

**Biomolecular Transport
Across and Along Membranes
studied by
Molecular Dynamics Simulations**

Dissertation
zur Erlangung des Grades
der Doktorin der Naturwissenschaften
der Naturwissenschaftlich-Technischen Fakultät II
– Physik und Mechatronik –
der Universität des Saarlandes

von

Weng In Siu

Saarbrücken

2010

Tag des Kolloquiums: 23.08.2010

Dekan: Univ.-Prof. Dr. rer. nat. Christoph Becher

Mitglieder des
Prüfungsausschusses:

Univ.-Prof. Dr. rer. nat. Manfred Lücke (Vorsitzender)
Univ.-Prof. Dr. rer. nat. Rainer Böckmann (1. Gutachter)
Univ.-Prof. Dr. rer. nat. Karin Jacobs (2. Gutachter)
Dr. rer. nat. Stephan Gier (Akademischer Mitarbeiter)

Hiermit versichere ich an Eides statt, dass ich die vorliegende Arbeit selbstständig und ohne Benutzung anderer als der angegebenen Hilfsmittel angefertigt habe. Die aus anderen Quellen oder indirekt übernommenen Daten und Konzepte sind unter Angabe der Quelle gekennzeichnet. Die Arbeit wurde bisher weder im In- noch im Ausland in gleicher oder ähnlicher Form in einem Verfahren zur Erlangung eines akademischen Grades vorgelegt.

Saarbrücken, Januar 2010

Abstract

Biomolecular transport processes allow the exchange of ions and other molecules across the membranes of organelles and cells. Here, we studied selected membrane-bound transport processes by means of molecular dynamics simulations, with a special focus on the interaction of membrane proteins with their environment.

As a model system, the cation-selective gramicidin channel in both the channel and non-channel conformation embedded in a phospholipid bilayer was chosen. Upon application of external electric fields a stabilizing effect of gramicidin on the membrane could be shown. Due to favorable interactions between lipids and cations at the channel entrance a significantly decreased free energy barrier for potassium ion permeation through the non-channel conformation was found, a result which underlines the importance of environmental effects for the function of membrane proteins. In order to improve the combined treatment of proteins and lipids in simulations, a new lipid force field based on the generalized AMBER force field was developed, yielding a marked improvement on the structural properties of DOPC membranes as compared to existing force fields.

Proton transport in bulk water and close to membranes was addressed by the semi-empirical Q-HOP method. In excellent agreement with experiments we found a linear dependency of proton diffusion on temperature and observed single events with large lateral diffusion distances close to membranes.

Zusammenfassung

Biomolekulare Transportprozesse erlauben den Austausch von Ionen und anderen Molekülen über die Membranen von Zellen und Organellen hinweg. In dieser Arbeit haben wir unter Verwendung der Methode der Moleküldynamiksimulation ausgewählte membrangebundene Transportprozesse untersucht.

Als Modellsystem wurde der in eine Phospholipiddoppelschicht eingebaute kationenselektive Gramacidinkanal sowohl in der Kanal- als auch in der Nichtkanalkonformation ausgewählt. In externen elektrischen Feldern konnte ein stabilisierender Einfluß des Gramacidins auf die Membran gezeigt werden. Attraktive Wechselwirkungen zwischen Lipiden und Kationen am Kanaleingang führten zu einer signifikant reduzierten Freie Energiebarriere für den Transport von Kaliumionen durch die Nichtkanal-Konformation. Dies unterstreicht die Bedeutung von Umgebungseffekten für die Funktion von Membranproteinen. Um eine konsistente Behandlung von Proteinen und Lipiden in Simulationen zu ermöglichen, wurde ein auf dem generalisierten AMBER Kraftfeld basierendes Lipidkraftfeld entwickelt, das die strukturellen Eigenschaften von DOPC Membranen merklich verbesserte.

Schließlich wurden der Transport von Protonen in Wasser sowie nahe einer Membran mittels der semi-empirischen Q-HOP Methode untersucht. Die gefundene lineare Abhängigkeit der Protodiffusion von der Temperatur sowie einzelne Ereignisse einer langreichweitigen Diffusion nahe der Membranoberfläche stehen in exzellenter Übereinstimmung zu Experimenten.

Acknowledgements

This is one of the most exciting pages for me in this thesis. The only page which stirs up all the memories for the past six years of my life in this little German town Saarbrücken, and in this wonderful little university, Saarland University. I am deeply thankful to my family, my friends, and my teachers who gave me countless support throughout my study and my PhD work.

First of all, this thesis would not have been possible without my supervisor, Rainer Böckmann, or "my Liebe boss" as we always called him. He led me into the exciting world of science, and carefully guided me to become a researcher. I appreciated his knowledgeability, his seriousness, his patience, and his devotion to support my work in his group, and especially his constant effort in critically correcting my writings.

I have to thank my colleagues, in particular Alexander Benedix, Beate Griepenau, Daniele Narzi, Simon Leis, and Caroline Becker for great discussions in scientific matters (even some silly questions on physics and chemistry), for having experience together with me to all the conferences, for contributing to the daily relaxing coffee breaks, and for helping me to deal with complicated living issues in Germany. Thanks again to Caroline for her important comments in the final writing stage of my thesis.

Collaboration in research is an excellent experience. I am gratified to have the chance to work with Robert Vácha and Pavel Jungwirth in the lipid force field project, with Gerrit Groenhof, Bert de Groot, Mareike Moritz, Wei Gu, and Volkhard Helms in the Q-HOP project, with Christian Weidemüller and Karin Hauser in the on-going ion channel project. I enjoyed the numerous discussions with Siti Azma Yusof in her Hepatitis C project, and with Ling Wang in her Barnase-Barstar project.

Computer is the main resource for my work. I am indebted to Volkhard Helms and Helmut Grubmüller for their generosity in sharing of their clusters for my research works. Special thanks go to the Graduate school of Physics in Saarland University and the Deutsche Forschungsgemeinschaft for funding my PhD study.

My joyful life in Saarbrücken would have been incomplete without the companion of all these friends: Sky Shi, Georgiana Ifrim, Deepak Ajwani, Yajing Zhang, Mars Wang, Tracy Chen, Hong Li, Hongbo Zhu and his family, Wei Gu, Ling Wang, Yvonne Low,

X

Zizhou Zheng, and Zhichao Chen.

Last, but not the least, thanks to my mom and dad who always trust me in all the decisions that I had to make. Your care and love are always in my heart - "I love you". Thanks to Antony Si Tou who ran hand-in-hand with me through all the ups and downs of my emotional landscape, and managed all the troubles that I created.

To God, thanks for being with me.

Contents

List of figures	iv
List of tables	vii
1 Introduction	1
1.1 Lipids and membranes	2
1.2 Membrane proteins	4
1.3 Experimental studies of membrane systems	7
1.4 Computational studies of membrane systems	8
1.5 Organization of the thesis	12
2 Methodology	15
2.1 Molecular dynamics simulation	15
2.2 Free energy calculations	20
2.2.1 Free energy perturbation and thermodynamic integration	21
2.2.2 Potential of mean force	22
2.3 A semi-empirical proton transport method (Q-HOP MD)	24
2.3.1 Potential of the proton transfer process	25
2.3.2 The Q-HOP model	25

3	Electric Field Effects on Membranes: Gramicidin A as a Test Ground	31
	Summary	31
3.1	Introduction	32
3.2	Materials and methods	34
3.3	Results and discussion	38
	3.3.1 Electric field effects on the membrane	38
	3.3.2 Gramicidin A in an external electric field	42
3.4	Summary and conclusions	51
	Acknowledgements	53
4	Low Free Energy Barrier for Ion Permeation Through Double-Helical Grami- cidin	55
	Summary	56
4.1	Introduction	56
4.2	Methods	58
	4.2.1 System setup	58
	4.2.2 Potential of mean force calculations	59
4.3	Results	61
	4.3.1 Potential of mean force	61
	4.3.2 Pore radius of gramicidin	65
	4.3.3 Energy decomposition	66
	4.3.4 PMF with the modified potassium-carbonyl oxygen parameters . .	68
4.4	Discussion and summary	70
	Acknowledgements	73
5	Biomolecular Simulations of Membranes: Physical Properties from Different Force Fields	75
	Summary	75

<i>CONTENTS</i>	iii
5.1 Introduction	76
5.2 Methods	78
5.2.1 Initial structures	78
5.2.2 Force fields parameters	79
5.2.3 Simulation conditions	82
5.2.4 Analysis	82
5.3 Results	85
5.3.1 Area per lipid	85
5.3.2 Lipid headgroup orientation	86
5.3.3 Lipid order parameter	87
5.3.4 Density profile and membrane thickness	89
5.3.5 Lipid and water diffusion	92
5.3.6 Electrostatic potential and dipole moment	94
5.4 Discussion	98
5.5 Conclusion	100
Acknowledgements	101
6 Simulating Proton Transfer Using the Semi-Empirical Q-HOP Method	103
Summary	104
6.1 Introduction	104
6.2 Methods	106
6.3 Proton diffusion in bulk water	110
6.3.1 Diffusion	110
6.3.2 Regimes of the proton transfer reaction	111
6.3.3 Structure of the hydronium solvation shell	114
6.4 Proton diffusion at the membrane-water interface	116
6.4.1 Proton mobility	118

6.4.2 Proton solvation in the membrane	123
6.5 Conclusion and future work	126
Acknowledgements	128
7 Summary & Conclusions	129
Bibliography	134
List of publications	147

List of Figures

1.1	Structure of a glycerophospholipid	3
1.2	The different structural phases of amphiphilic lipids	3
2.1	The thermodynamic cycle for calculating the free energy of molecular solvation.	22
2.2	The general one-dimensional double-well potential of the proton transfer process	26
2.3	The three regimes in the Q-HOP model	28
3.1	The gramicidin-membrane simulation system for electric field study	35
3.2	Hydrocarbon-chain order parameters of DMPC molecules around gramicidin A	40
3.3	Pore formation times observed in MD simulations	42
3.4	Root mean square deviation of the gramicidin A in response to applied external electric fields	43
3.5	Root mean square fluctuations of the gramicidin A in response to applied external electric fields	44
3.6	The changes in the monomer dipole moment over the simulations	46
3.7	Average dipole moment of all water molecules with and without electric fields	47

3.8	Dipole moment of water molecules confined inside the gramicidin channel	48
3.9	Schematic drawing of the protein and water file dipole moments for the two different gramicidin conformations	49
3.10	Snapshots of potassium cation passage through the gramicidin channels .	51
4.1	The two major conformations of gramicidin	57
4.2	Time evolution of the asymmetric and symmetric PMF profiles	62
4.3	Comparison of the PMF profiles for K^+ permeation through the gramicidin in HD and DH conformation	63
4.4	Radius of the gramicidin channels along the helical axis	66
4.5	Interaction energies of ion with different components of the environment	67
4.6	Cumulative radial distribution functions of the DMPC choline and phosphate group to the potassium ion	68
4.7	Snapshots of simulations with a potassium ion restrained to the channel entrances	69
4.8	Comparing the PMF profiles obtained with calibrated K^+ -O LJ interactions	70
5.1	Area per lipid for the five investigated DOPC systems	85
5.2	Deuterium order parameters of DOPC using GAFF, CHARMM and Berger force fields	88
5.3	The electron density profiles of the DOPC systems	90
5.4	Comparison of the electron density profiles at the membrane-water interface	91
5.5	DOPC lipid diffusion coefficients calculated for different time lengths of the simulations	93
5.6	The lateral diffusion coefficients of water molecules at the membrane-water interface	95
5.7	Total electrostatic potential and contributions of DOPC systems	96
5.8	Average water dipole moment along the membrane normal of the DOPC systems	97
6.1	Diffusion coefficients of hydronium as a function of the Q-HOP waiting time	108

6.2	Chemical structure of the GMO molecule	108
6.3	Diffusion coefficients of the hydronium ion as a function of the temperature and of the applied hydronium charge set	111
6.4	Number of proton hopping events and the proton mean residence time in waterbox simulations	112
6.5	Regimes of all hopping events from a Q-HOP simulation at 300 K	113
6.6	Distribution for E_{12} and R_{DA} from proton hopping reactions	114
6.7	The radial distribution function of water oxygen and of water hydrogen around the hydronium oxygen	115
6.8	Distribution of the hydrogen bond types of hydronium and water molecules in the 0/1/2-solvation shell centered around the hydronium	116
6.9	The average densities of different groups in Q-HOP GMO system	117
6.10	The slab lateral diffusion coefficients of the hydronium ion in the GMO simulations	119
6.11	Travelling behaviour of the hydronium ion in GMO simulations	120
6.12	Snapshots of the 1.9-nm hydronium diffusion along the membrane surface	121
6.13	The distributions of the lateral distance of the hydronium round-trip travels in the membrane	122
6.14	Comparison of the mean residence times of the excess proton with a water molecule or between a pair of water molecules.	123
6.15	The distribution of the lateral distance travelled by the hydronium in the GMO system and in the pure water box	124
6.16	The radial distribution function of the GMO oxygens around the hydronium oxygen.	125
6.17	The autocorrelation function of hydrogen bonds between the hydronium ion and the lipid polar headgroups	126

List of Tables

3.1	Area per lipid in simulations of a pure DMPC bilayer and of the gramicidin/DMPC system at different external electric field strengths.	39
3.2	Membrane thickness in different lateral separations from the gramicidin .	41
3.3	The average dipole moment of the gramicidin monomers and the total protein dipole moment	45
3.4	Diffusion coefficient of water molecules confined to the gramicidin channel and spontaneous water passage events	50
4.1	Comparison of our PMF results to former MD studies	63
5.1	The atom-types, the partial charges, and the schematic drawing of the DOPC lipid	81
5.2	Overview of the DOPC simulation systems using different lipid force fields	83
5.3	Membrane structural parameters in DOPC systems	86
5.4	Distribution of lipid headgroup orientations and the lipid dipole moments in DOPC systems	87
5.5	The lateral diffusion coefficient for water molecules and for DOPC molecules.	94
6.1	Partial atomic charges of the hydronium ion.	107
6.2	The GAFF atom types and the partial atomic charges for the GMO molecule.	109

6.3	The distribution of proton transfer reactions taken place in the three defined regimes	113
6.4	Area per lipid of GMO bilayers with different ionic concentrations	117
6.5	The diffusion coefficient of the hydronium ion in GMO systems and in the water box systems.	118

Chapter 1

Introduction

The importance of membranes for the viability of biological cells has become increasingly apparent. As the boundary of the cell (as well as of the organelles) and the platform for hosting about one-third of all the protein machineries, membranes are found not only to act as a passive barrier but also to actively participate in most of the interactions between the cell and its environment, and between different compartments within the cell [1]. Specifically, the plasma membrane was found to be the key component in sensory and signaling pathways [2, 3]. In addition, membranes are involved in all sorts of molecular transport in the cell [4].

Computational studies of biological processes have received increasing attention due to their interpretative power and the ability to create different levels of model abstractions. In particular, the method of Molecular Dynamics (MD) simulation allows an atomistic description of the system evolving in time through the laws of classical mechanics. Therefore, MD simulations are the method of choice for studies of time-dependent biological processes, such as molecular transport and pathways [5–7], ligand binding [8–11], protein folding [12–15], or of the conformational dynamics [16–18] of proteins.

With the improvement of force fields for the modeling of lipid membranes during the past decade [19–21], the study of biological processes occurring in or close to membranes via MD simulations became feasible. Investigated processes included ion permeation through membrane channels [22–25] and their gating mechanisms [26–29], partitioning of small molecules into membranes [30, 31], formation of lipid domains [32, 33],

electroporation [34–36], protein insertion and folding [37, 38], etc.

In this thesis, the roles and impacts of lipid membranes and ion channels in molecular transport are studied by means of Molecular Dynamics simulations. Overviews of the biological basis of both proteins and membranes are presented in the following sections. In addition, current experimental techniques and computational methods to study membrane systems are described.

1.1 Lipids and membranes

The primary role of biological cell membranes is the formation of a semi-permeable barrier to separate the cytosolic content from the environment. The major constituents of membranes are amphiphatic molecules, so-called *lipids*. The number of lipid species differing in headgroup and acyl chain composition is huge (in the order of 10^3 in the eukaryotic cell [39, 40]). Membranes in different parts of the cell and in different organisms are found to contain distinct mixtures of lipids [41, 42]. The composition is adjusted depending on the developmental stages of the cell and additionally affected by various environmental factors such as temperature and pH. The most important class of membrane lipids are the phosphate-containing *glycerolipids*. As shown in Fig. 1.1, they are composed of fatty acids esterified at position 1 and 2 of the glycerol backbone (so-called diacylphosphoglycerides), and the phosphate at position 3. The name of the lipid is derived from the moiety attached to the phosphate group, the length of the fatty acid chains and the number of unsaturated segments along the chains.

The amphipathic nature of lipids – the hydrophilic headgroup at one side and the hydrophobic carbon tails at the other – is the main factor driving their self-association into membranes. Although lipids occur in different shapes (inverted conic, cylindrical, or conic shapes) and pack into different structural phases (micelle, bilayer, and hexagonal phases, respectively, see also Fig. 1.2) when dissolved in aqueous systems, they stabilize into the bilayer structure in the living cell at physiological condition. The hydrophilic headgroups form an ionic interface which interacts with the environmental aqueous solvents. Thereby, the hydrophobic tails are completely shielded from the solvent in the bilayer core.

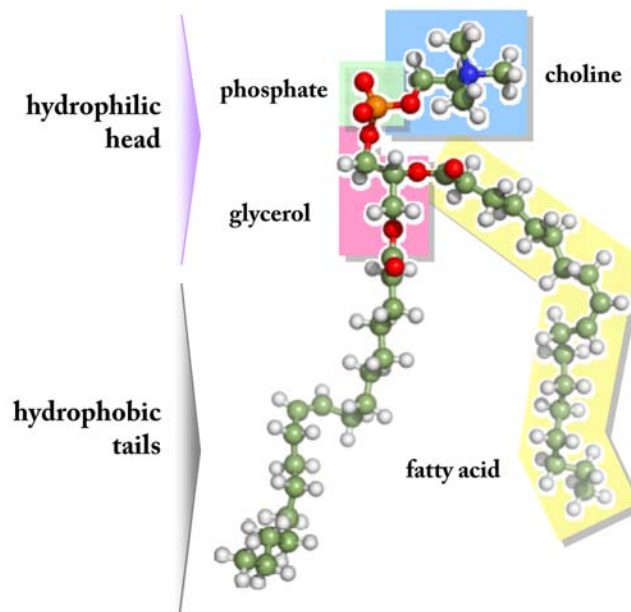


Figure 1.1: Structure of a glycerophospholipid. A phosphate-based glycerolipid is made up of the glycerol backbone, two fatty acid chains and a phosphate group attached with a headgroup moiety, such as choline (here), ethanolamine, serine, etc.

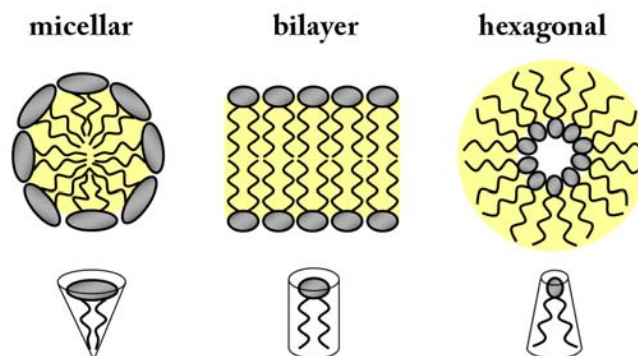


Figure 1.2: The different structural phases of amphiphilic lipids in 2D schematic representation (from left to right): inverted cone shaped lipids favor a micelle structure, cylindrical lipids favor a bilayer, and cone shaped lipids preferentially adopt the hexagonal (H_{II}) phase. The hydrophobic regions are colored in yellow.

Lipid bilayers exist in different phases [43]. At low temperatures, lipids are highly ordered and the hydrocarbon chains are arranged into all-trans conformation with a preferred tilting angle with respect to the bilayer normal, the bilayer is in the so-called

gel phase (L_β). Upon heating, the bilayer undergoes an endothermic phase transition. The lipids exhibit an enhanced disorder in the tails, and the bilayer adopts the liquid-crystalline state (L_α). The topology of the lipid matrix in this state is not static but rather dynamic. Lipids show considerable motions such as gauche-trans isomerization, rotation, translation, and even interchange between the lipid leaflets (*flip-flop*). The temperature at which this transition occurs (*transition temperature*) depends on the nature of the acyl chains, the headgroups and the environmental conditions (such as pressure, pH, ion concentration, etc.) [44–50].

The increasing interest in biological membranes in recent years has deepened our understanding of the biological functions of membranes. In the conventional fluid mosaic model proposed by Singer and Nicholson [51], the bilayer was considered simply as a rather homogeneous-passive-unperturbed environment embedding freely-diffusing proteins at low concentration. However, it could be shown that not only the cell interior but also biological membranes are crowded (protein/lipid ratio is in the range of 0.25 to 5 [52]), and vary in composition and thickness to great extent [53]. Lipid mixtures enriched with cholesterols and sphingolipids can undergo phase separations forming microdomains called *rafts*, which is probably of importance for compartmentalizing the membrane and fencing related proteins in order to achieve signaling cascades [54] and trafficking [55]. In conclusion, membranes can no longer be looked at as passive barriers only. There is increasing evidence that they also actively regulate various biological processes eventually accomplished by membrane proteins.

1.2 Membrane proteins

In general, there are two classes of membrane proteins: *integral* membrane proteins are permanently embedded into the membrane, and *peripheral* membrane proteins are only temporarily attached to the bilayer, or to other integral membrane proteins. Integral membrane proteins span through the whole hydrophobic core of the bilayer (also termed *transmembrane proteins*) and usually consist of three parts: the intracellular domain, the transmembrane region and the extracellular domain. The membrane spanning region frequently adopts an α -helical structure (or β -barrel) in order to maximize the hydrogen bonding of the peptide bonds, thereby shielding polar groups from the hydrophobic environment. The polypeptide chains can pass the bilayer several times, adjusting as a bundle of helices which together may form a functional unit directly coupled to solu-

ble domains. For example, the cytosolic headpiece of the sarcoplasmic reticulum Ca^{2+} -ATPase binds and unbinds the Adenosine-5'-triphosphate (ATP) to induce translocation of calcium ions through the pore [56]. The famous signaling protein family, the G-protein-coupled receptors (GPCRs), couple the binding of signaling molecules (*ligands*) from the cell exterior to the activation of specific G proteins on the cytoplasmic side initiating a signal transduction cascade [57].

As the *gates* of the cell, membrane proteins are involved in a wide variety of biological processes including molecular transport, signal transduction, respiration, enzymatic activity, cell-cell recognition, and others. Structure determination of membrane proteins is an extremely challenging task. The first three-dimensional structure of a membrane protein, *bacteriorhodopsin*, was determined in 1975 [58]; not until 10 years later, the high-resolution structure of the *Rhodospseudomonas viridis* photosynthetic reaction centre was solved using X-ray crystallography [59]. To present, there are about 220 unique membrane protein structures determined [60] (as of Jan 2010) as compared to 15,600 soluble proteins [61]. Considering that about 30% of the genome codes for membrane proteins [62], the knowledge about membrane proteins is still very limited.

Among membrane proteins, the pore-forming ion channels are of particular interest. They regulate the electrolytic composition across the cell by selectively controlling the transport of different physiological species across the hydrophobic barrier. The central pore of channels frequently feature a hydrophilic interior surface, which facilitates the diffusion of polar or charged species by lowering the permeation barrier. The pores may appear in structurally different *open* and *close* conformations enabling gating regulated by external factors: E.g. the binding of a ligand in the toxin-binding site of Nicotinic acetylcholine receptors induces opening of the cation-selective pore [63]; in the action potential, depolarization of the membrane activates the voltage-dependent K^+ channels whereas repolarization deactivates the channels [64]; mechanical stresses applied to a membrane open the nonselective pore of mechanosensitive ion channels to allow an increase in compensatory solute flux [65]. The structural complexity of ion channels is diverse. It can be as simple as one helical pore like the model peptide Gramicidin [66], or as complicated as the family of large voltage-gated channels, which are multidomain complexes with pores surrounded by bundles of helices [67]. Also, it is not uncommon that one channel allows simultaneous transport and countertransport of different molecular species in one reaction cycle. For example, the Ca^{2+} -ATPase transports two calcium

ions and countertransports 2–3 protons [56]; the sodium-potassium pump moves three Na^+ ions out of the cell and takes two K^+ ions in exchange [68].

Around membrane proteins, distinct annular shells of lipids with restricted mobility are formed [69]. When the hydrophobic thickness of these lipids is different from the thickness of the protein's nonpolar surface, either protein or membrane or both of them are distorted. This so-called *hydrophobic mismatch* may be minimized by lipid stretching, tilting of the membrane protein, or compression of the membrane. For a membrane protein with a rigid interface, often little or no effect is observed on the structure of the membrane protein. Instead, the surrounding lipids deform to match the protein. Oriented circular dichroism spectra (OCD) and X-ray diffraction patterns showed that the shorter DLPC and the longer DMPC approached to a common thickness with embedded β -helical Gramicidin in the membrane [70] but not with the α -helical transmembrane peptide WALP which is less structurally rigid [71]. The outer membrane protein OmpA can fold to the same stable β -barrel structure regardless of the thickness of the bilayer [72]. The strength of lipid binding to the β -barrel trimer OmpF showed a lipid chain length dependency, which suggests that thinning and thickening of lipids occur around the protein structure [73]. In contrast, for less tightly anchored or less rigid proteins, the free energy cost to tilt or even to deform (parts) of the protein may be comparable or smaller than required for local compression or stretching of the membrane. For example, the helical bundle K^+ channel from *Streptomyces lividans* *KcsA* [74] and the mechanosensitive channel *MscL* [75] tilt in accordance with the change in the lipid chain lengths; and for Ca^{2+} -ATPase the enzymatic activity is affected when incorporated in lipid bilayers with too short ($< 14\text{C}$) or too long ($> 20\text{C}$) carbon chains [62]. Aromatic residues of the protein near the ends of transmembrane helices may play a role in adjusting the effective hydrophobic length of the protein by rotating relative to the protein tilting [76].

In addition, specific interactions between proteins and lipids, depending on the type of the lipid headgroup, are frequently reported (See [42, 77] for reviews, and [78–81] for recent studies). Lipids carrying a net charge are usually able to bind at defined grooves on the protein surface or at the interface of oligomers, and thus can have a marked influence on the structure and function of a membrane protein. E.g., the negatively charged cardiolipin lipid (CL) that binds at the interface of the two monomers of the Cytochrome *c* Oxidase was found to be crucial for the electron transport activity of the protein [42, 82]. A recent study has also shown that deformed membranes due

to hydrophobic matching or bilayer bending possibly induce coupled conformational changes of neighboring membrane proteins by attractive or repulsive interactions over distances [83].

1.3 Experimental studies of membrane systems

In order to understand the physicochemical and biological properties of membranes at the cellular level while avoiding the complexity of the biological membrane *in vivo*, different model bilayer systems have been devised for biophysical investigations. The conventional model is the *black lipid membrane* (BLM) [84, 85]. It consists of a phospholipid bilayer formed across a 1 mm hole placed between two chambers of organic solution. Pore-forming proteins such as ion channels can then be inserted into the bilayer and the channel activity observed by measuring the current through the hole. The setup of a BLM is simple but the bilayer has only a short lifetime (a few hours). A more robust model are *solid supported lipid bilayers* (SLB) [86], in which a stable bilayer is formed on top of a substrate surface with a thin intermediate hydration layer. The main advantage of SLB is that surface analytical techniques such as atomic force microscopy (AFM) can be used directly to probe e.g. protein-membrane interactions on the membrane surface [86].

Another popular membrane model are *liposomes*, i.e. lipid bilayers forming spherical vesicles. In general, these are formed by dispensing dried lipids into aqueous solution by different mechanistic ways [87]. Hydrophobic interactions of the lipid acyl chains force the formation of a closed vesicle. Liposomes can take the form of a single layer (unilamellar) or of a stack of concentric bilayers (multilamellar) [88]. Their sizes vary from tens of nanometers to some hundred micrometers. The application of liposomes is diverse [89]. As the lipids and reconstituted molecules in the liposomes can diffuse freely, their usage is advantageous for the study of dynamic properties such as domain formation, fluctuations, permeability, fission, and fusion.

The most important methods to determine the structure of membranes are *X-ray* and *neutron diffraction* [88]. In X-ray diffraction experiments, beams of X-rays are directed at oriented multilamellar stacks of membranes containing thousands of lipid bilayers [90]. X-rays scattered by the electrons produce a diffraction pattern characterized by 5–10 sharp Bragg reflections [88]. The intensity data is analyzed to yield the one-dimensional electron density profile along the bilayer normal. Structural parameters

such as volume and bilayer thickness, etc. can be deduced [91]. Whereas quantities such as the area per lipid or the volume of the component groups cannot be deduced directly from the density profile, they may be inferred from the changes in the electron density between measurements of the fluid phase and the gel phase bilayer with the same head-group [91, 92]. By combining data obtained independently from X-ray and selectively deuterated neutron diffraction experiments, it is possible to derive the positional distribution of each individual molecular segment in the bilayer [93].

Apart from the membrane structure, knowledge about the membrane dynamics is crucial to elucidate on the function of membranes. Characteristics like the lipid order (or the orientation) [94] and the motional behavior of lipids can be studied using spectroscopic techniques such as nuclear magnetic resonance (NMR), infrared and Raman spectroscopy, or electron paramagnetic resonance (EPR) on selective isotopic labels. Different types of lipid motion have distinct correlation times [95]. For example, gauche-trans isomerization in the acyl chain occurs on the picosecond time scale (order of 10^{-10} s), lipid rotation and lateral diffusion on the nanosecond time scale ($\approx 10^{-8}$ to 10^{-7} s), collective motions like undulations on the microsecond time scale ($\approx 10^{-6}$ to 1 s), and translayer movement or flip-flops on the millisecond to second time scale ($\approx 10^{-3}$ to 10^4 s). Depending on the operational time scale of each experimental technique, experimental results are thus either obtained as weighted average over all conformers within the measured time (motions with shorter correlation time) or as superposition of signals from different states (motions with longer correlation time) [95].

1.4 Computational studies of membrane systems

Biological membranes are extremely complex systems (Section 1.1 and 1.2). Membranes occur in different states, their temperature- and composition-dependent properties, and the inserted or adsorbed proteins impose difficulties in experimental studies. Often, only macroscopic characteristics can be determined from experiment, while the microscopic details are difficult or impossible to assess with current methods.

Theoretical and computational studies allow the fragmentation of the relatively complex system into different levels of abstraction, from which the physical concepts can be studied in detail. The tools employed in computational studies of biological systems include *ab initio* simulations [96], classical molecular dynamics (MD) simulations [97] at

different coarsening levels [98], Monte Carlo (MC) [99], Brownian dynamics (BD) simulations [100], and continuum studies [101]. Each of these methods has strengths and weaknesses depending on the degree of approximation.

Among these methods, MD simulations are particularly interesting because they allow to study the system at the atomic level on time scales of up to a few microseconds [102, 103]. In MD, snapshots of the system as a function of time (called *trajectory*) are generated by numerical integration of the Newton's equations of motion. The quality of the results depend crucially on the parameterization of the underlying force field. The parameterization is performed by fitting parameters in the defined functional forms to experimental and theoretical results, the latter are e.g. obtained from *ab initio* calculations on small molecules. Most importantly, the parameterization determined in this way is assumed to be transferable between different problems. Often, simulations are used to provide a molecular interpretation of experimental observables. As an example, Feller could link atomic motions of phospholipids in a MD simulation to rates of magnetization transfer within a bilayer, thereby providing an atomic-level description of complex NOESY cross-relaxation rates observed in NMR experiments [104]. A different study by Böckmann *et al.* succeeded to relate macroscopic rates for the formation of electropores in lipid vesicles to pore formation kinetics in MD simulations of comparatively small lipid bilayers. Thereby, a four-state pore formation model giving hints to the nature of the pore intermediates could be suggested [105].

In addition to studies on the structure and dynamics of phospholipid bilayers, MD simulations are increasingly used to shed light on the intricate interactions between membrane proteins and membranes. Successfully investigated systems include membrane channels and transporters [106, 107], G-protein coupled receptors [108–110], ATP synthases [111, 112], and membrane surface-bound proteins [113, 114], etc. Recent studies have also examined the solvation and partitioning behavior of amino acids into lipid bilayers [115, 116]. This helps to predict the stability of proteins in membranes and to understand the relation of important residues to the function of proteins. For example, the low transfer free energy of aromatic tryptophan to the bilayer-water interface explains its functional role in positioning membrane proteins in the bilayer [117–119]. Likewise, the high cost of burying an arginine into the bilayer core [116] justifies the enhanced water penetration around the voltage-sensor (VS) domain containing four arginines [120], where the motion of the VS domain is believed to be coupled to the gating of the chan-

nel [121].

For the initial setup of a membrane-protein system for simulation, the protein has to be inserted and oriented e.g. within a pre-equilibrated lipid bilayer. Apart from the simulation conditions such as the temperature, the pressure, or external fields, it is essential to have a consistent force field at hand describing both lipid and protein atoms. Major biomolecular force fields include AMBER [122], CHARMM [123], GROMOS [124] and OPLS-AA [125]. Each of them has developed consistently for protein simulations, and evolved its unique parameterization strategy over years. For example, in AMBER atomic charge fitting using quantum calculations was performed on molecular fragments in vacuum whereas solute-water dimers were used in CHARMM [122]. Unlike AMBER and CHARMM, charges were fitted for functional groups in the OPLS force field such that they are transferable between molecules [126]. In GROMOS, values from fitting to quantum calculations serve only as an initial guess for atomic charges, they are subsequently calibrated together with other nonbonded parameters to reproduce experimental data such as the heat of vaporization and densities. While in AMBER the torsional parameters were only fit to quantum mechanical conformational energies of target molecules, parameters in CHARMM are refined further to attain agreement between protein backbone angles of simulations and experiments [122].

Within the last years, the above biomolecular force fields have been extensively optimized especially for treating protein molecules, and the results are generally good. However, the progress in the development of lipid force fields is much slower, which is due to the long simulation times required to test the parameter sets, and partly due to insufficient or inaccurate available experimental data (e.g. lack of structural information; controversial dipole potential of membranes [20]) to guide the development and verification of the results. Nevertheless, there are two lipid force fields commonly in use – the CHARMM [127] lipid force field as part of the CHARMM distribution, and the AMBER/OPLS based so-called Berger [128] lipid force field. For the simulation of mixed protein-lipid system, CHARMM offers a consistent framework; however, the CHARMM force field shows deficiencies for phospholipid systems. In contrast, the Berger force field was optimized to reproduce experimental observables of phospholipids but does not offer a consistent link to a protein force field [129]. With the recently published general AMBER force field (GAFF) [130], new lipid force fields can now be developed [131, 132] and used consistently with the AMBER force field for proteins and nucleic acids.

In spite of the vast advances in computer power, the length scale and time scale of simulations are still limited. Typical membrane systems consisting of about 10^4 to 10^6 atoms may be simulated for 100 ns to a few microseconds in atomic detail. These size and time limitations confine the types of biological processes that can be studied by conventional MD. Therefore, non-equilibrium simulation techniques such as umbrella sampling [133] and steered molecular dynamics [134] are frequently employed as a remedy to the time scale problem. E.g. in order to study the free energy barrier for ion transport through an ion channel, it would suffice to compute the free energy profile $G(Z)$ from the projected ion density $\rho(Z)$ along the channel axis Z according to $G = -k_B T \ln \rho(Z)$. Since spontaneous passage of ions is too slow, an additional *umbrella* potential may be added to ions placed along the channel axis. Deconvolution of the biased potential then yields the true free energy profile. For large system sizes, coarse-grained approaches [98, 135–137] with significantly reduced number of degrees of freedom – e.g. by replacing groups of atoms by effective, coarse atoms [138] selectively reduce uninteresting degrees of freedom may be preferable.

Future challenges for membrane simulations point into two directions: Starting from simple homogeneous phospholipid bilayers the field develops towards systems with a more physiological composition of both lipid mixtures and of organic compounds in order to study the functionality of membrane proteins or even close-to-physiological biological membranes. The interactions between these heterogeneous molecules are crucial for their structure and function. There is a compelling demand for further optimization of force fields for improved lipid models and molecular interactions. Additionally, polarization effects are probably of importance for the hydrophilic-hydrophobic interface [139]. Polarizable models became mature during the past few years and will be computationally feasible also for membrane systems in the near future. On the other hand, coarse-grained models will be continuously in demand to uncover the time scales and length scales inaccessible by atomistic models. Major efforts will be devoted to the development of scale-crossing models between atomistic and coarse-grained descriptions, allowing to combine micro- or even millisecond dynamics of large systems with the nanosecond dynamics of lipids or proteins, and even to the quantum dynamics of e.g. proton transfer process.

1.5 Organization of the thesis

In this thesis, the roles of membranes and channel proteins in the transport of molecular species along and across the membranes were studied. The work of this thesis can be divided into three parts: applications, force field development, and method development. For the former, we studied selected transport mechanisms of both membranes and of a membrane-embedded ion channel. The biotechnologically relevant electric-field induced pore formation – enhancing the transport through membranes – was compared for pure phospholipid bilayers and protein-containing bilayers mimicking more biological membranes. Cation-selective transport through membranes was studied for the ion channel Gramicidin. In order to enhance the description of the protein-lipid interaction, new lipid force field parameters were devised in the second part. Finally, a semi-empirical methodology to simulate proton transfer reactions was reimplemented and tested on the bulk water and membrane systems within classical MD simulation algorithms. The mentioned topics will be addressed in the following chapters:

Chapter 2 This chapter gives a brief account of the methodologies used in this work, including MD simulation, free energy calculation, and the semi-empirical proton hopping algorithm implemented within a conventional MD algorithm.

Chapter 3 Many known biological transport mechanisms in the cell are strongly coupled to changes in the membrane potential. Electric fields, either created by ionic gradients across the membrane or applied externally, may induce local perturbations of membranes and result in the formation of electropores. Through these pores, molecules such as ions, proteins, and DNA, etc. can be exchanged between the cell or organelle interior and exterior. Electric fields were also observed to have direct influence on the function of channel proteins by changing the channel conformations, and thus can promote or impede the transport of molecules through the pores. Here we report the effect of the change in membrane potentials on a membrane-protein system by applying different strengths of external electric fields. The influence of the embedded channel Gramicidin on the membrane properties is examined with a focus on the membrane stability with respect to external electric fields. Additionally, the properties of water permeation and ion diffusion through the pores were investigated.

Chapter 4 This chapter extends the study of the Gramicidin channel to the calculation of the free energy profile of potassium permeation. As ion passage is a rare event on the time scale of computer simulations, a biasing sampling method was employed in MD to obtain reliable energy profiles. In this work, the ion transport through the two main conformations of Gramicidin was analyzed and compared. A significantly decreased free energy barrier for potassium permeation was found for the so-called “non-channel” conformation of gramicidin. Importantly, our study revealed the importance of lipids in promoting or supporting the protein functionality as a channel.

Chapter 5 The focus of both experimental and theoretical studies on biological membranes increasingly turned during the last year towards an understanding of the protein-lipid interaction. As lipid membranes forms the environment for membrane proteins regulating the transport of drugs into or out of cells and organelles, computational models that accurately describe the properties of lipids and in particular the interactions of lipids with proteins and drugs are required. Here, we report the development of a new lipid force field based on the general AMBER force field, which can consistently be used for the combined simulation of phospholipids with proteins, DNA, or drugs. Comparison to existing lipid force fields indicate remarkable improvements in reproducing the structure and dynamics of phospholipid bilayers.

Chapter 6 Proton transport is one of the most abundant reactions in the biological cell. However, purely classical MD simulations cannot be used to study the proton transport as it involves the frequent breakage and reformation of molecular bonds, i.e. the quantum nature of the proton is crucial e.g. for its diffusion. The method of choice to study proton transfer and transport pathways on long time scales is the semi-empirical Q-HOP method [140]. In this chapter, submicrosecond simulation studies of proton transfer in bulk water and in a membrane-water system are reported. A particular focus is on the examination of the Q-HOP method by comparing the simulation results to known experimental values. The proton diffusion behavior on the membrane surface and in different ionic concentrations were additionally analyzed. Our results show that membranes, although reducing the mobility of protons in their vicinity, can extend the lateral diffusion distance of protons as compared to that in bulk water.

Chapter 7 summarizes the different research studies of this thesis and provides a brief discussion of this and related computational studies in membranes and membrane

proteins. Future methodological development for the study of biological transport processes will be addressed.

Methodology

2.1 Molecular dynamics simulation

Molecular Dynamics (MD) is a method that allows to simulate the time evolution of a system of atoms within the context of classical mechanics. In MD, the rapid motion of the electrons is averaged out assuming that they adjust instantaneously to the comparatively slow motion of the heavy nuclei (Born-Oppenheimer approximation). Thereby, the Schrödinger equation can be separated into a time-dependent equation for the nuclei and a time-independent Schrödinger equation for the electron degrees of freedom. The Hamiltonian of the time-dependent Schrödinger equation can be written solely as a function of the positions of the nuclei. In a second approximation, the Schrödinger equation for the nuclei is replaced by the Newton's equation of motion. The electronic potential is exchanged by an empirically derived force field (see below). In the equations of motion, the total force F_i acting on a particle i is given as the negative derivative of the potential energy of the system:

$$\mathbf{F}_i = m_i \mathbf{a}_i = m_i \frac{d^2 \mathbf{r}_i}{dt^2} = -\nabla_{\mathbf{r}_i} V(\mathbf{r}_1, \dots, \mathbf{r}_N). \quad (2.1)$$

Given an initial state, the equations of motion are solved numerically to generate a trajectory describing the time-evolution of the system. At any instant in time, the total

energy of a system is the sum of the kinetic and the potential energy:

$$E = \sum_{i=1}^{3N} \frac{1}{2} m_i v_i^2 + V(\mathbf{r}_1, \dots, \mathbf{r}_N), \quad (2.2)$$

where the potential energy $V(\mathbf{r}_1, \dots, \mathbf{r}_N)$ is a function of the particle coordinates \mathbf{r}_i using an empirical *force field*, namely a set of simple functions describing the bonded interactions (bond length b , angles θ , and torsions ϕ) and the non-bonded interactions (electrostatics and van der Waals interactions) between atoms:

$$\begin{aligned} V(\mathbf{r}_1, \dots, \mathbf{r}_N) = & \sum_{\text{bonds}} k_b (b - b_0)^2 + \sum_{\text{angles}} k_\theta (\theta - \theta_0)^2 + \sum_{\text{torsions}} k_\phi [1 + \cos(n\phi + \delta)] \\ & + \sum_{\text{nonbonded-pairs}} \left(\frac{q_i q_j}{r_{ij}} + \frac{A_{ij}}{r_{ij}^{12}} - \frac{C_{ij}}{r_{ij}^6} \right). \end{aligned} \quad (2.3)$$

The bonded energy terms penalize deviations from the respective equilibrium or reference values for the bond length (b_0), the angle between three bonded atoms (θ_0), and the equilibrium states of torsions around a bond (n, δ). For non-bonded interactions, the potentials are a function of the distance r_{ij} between pairs of particles (i, j). The electrostatic interactions are described by Coulomb's law. Particles in a molecule usually do not carry full electron charge, instead the charge distributions are represented by partial atomic charges q_i centered at the nuclei. The short-ranged repulsive (Pauli repulsion) and the dispersion forces, i.e. the van der Waals interactions, are commonly described by a Lennard-Jones potential. The repulsive part prevents particles from overlapping; while the attractive part, quickly decaying for long distances, models the cohesive property of dipole-dipole interactions.

A good integrator for the numerical integration of the equations of motion (Eq. 2.1) should conserve energy and momentum of the system and be time-reversible. A popular algorithm fulfilling these characteristics is the *Verlet* scheme [141], which is based on the finite difference method to approximate solutions to the differential equations employing a Taylor expansion. The time is discretized into intervals of small time steps Δt (1–5 femtoseconds). New atomic positions are propagated from positions \mathbf{r}_i and forces \mathbf{F}_i from the current and the previous time steps:

$$\mathbf{r}_i(t + \Delta t) = 2\mathbf{r}_i(t) - \mathbf{r}_i(t - \Delta t) + \frac{\mathbf{F}_i(t)}{m} \Delta t^2. \quad (2.4)$$

In the original Verlet algorithm, the velocity \mathbf{v}_i of atom i is not coupled to the calculation of the position, instead it is derived until the position in the next step is obtained:

$$\mathbf{v}_i(t) = \frac{\mathbf{r}_i(t + \Delta t) - \mathbf{r}_i(t - \Delta t)}{2\Delta t}. \quad (2.5)$$

A variant of the Verlet algorithm which improves on this problem is the *leap-frog* algorithm. It evaluates the atomic positions at the whole time step based on the velocity calculated at intermediate time steps:

$$\mathbf{r}_i(t + \Delta t) = \mathbf{r}_i(t) + \mathbf{v}_i(t + \frac{\Delta t}{2})\Delta t, \quad (2.6)$$

$$\mathbf{v}_i(t + \frac{\Delta t}{2}) = \mathbf{v}_i(t - \frac{\Delta t}{2}) + \frac{\mathbf{F}_i(t)}{m}\Delta t. \quad (2.7)$$

In this case, positions and velocities are coupled but are out of phase by a half time step. Another popular variant of the Verlet algorithm is the *velocity Verlet* algorithm, which yields the position, velocity and acceleration within the same time step:

$$\mathbf{r}_i(t + \Delta t) = \mathbf{r}_i(t) + \mathbf{v}_i(t)\Delta t + \frac{\mathbf{F}_i(t)}{2m}\Delta t^2, \quad (2.8)$$

$$\mathbf{v}_i(t + \Delta t) = \mathbf{v}_i(t) + \frac{\mathbf{F}_i(t) + \mathbf{F}_i(t + \Delta t)}{2m}\Delta t. \quad (2.9)$$

Note that two force evaluations are required in the procedure which makes velocity Verlet more expensive. In the Verlet scheme, the error in the position calculation is of the order $O(\Delta t^4)$, while the error in the calculation of the velocity is only of the order $O(\Delta t^2)$. Both the leap-frog and the velocity Verlet algorithms improve the velocity estimation and thus provide a better stability for the integration of the equations of motion.

According to the equipartition theorem, each degree of freedom contributes on average $k_B T/2$ to the energy in thermal equilibrium at temperature T , where k_B is the Boltzmann constant. Thus the system temperature T can be estimated according to

$$\sum_{i=1}^{3N} \frac{1}{2} m_i v_i^2 = \frac{3}{2} N k_B T. \quad (2.10)$$

The pressure P is calculated according to the virial equation as the sum of the product of positions and the forces F acting on this position due to all other particles in the

system:

$$PV = Nk_B T + \frac{1}{3} \sum_{i=1}^N r_i F_i, \quad (2.11)$$

where V is the volume of the system. A standard MD simulation generates an NVE ensemble (constant number of particles, volume and energy). It is also possible to generate other ensembles such as the NPT (constant number of particles, pressure and temperature) by adjusting the velocities or the sizes of the box through coupling to an external heat bath and/or pressure bath. A widely used method is the Berendsen coupling algorithm [142]. In Berendsen temperature coupling, the change in temperature is proportional to the difference between the heat bath and the system temperature with the strength of the coupling controlled by the coupling parameter τ . The coupling is achieved by scaling of the velocities with the scaling factor λ :

$$\lambda = \sqrt{1 + \frac{\Delta t}{\tau} \left(\frac{T_{ref}}{T(t)} - 1 \right)}. \quad (2.12)$$

Constant pressure can be achieved analogously by scaling of the atomic coordinates to obtain the desired pressure within the box.

Simulations of the bulk phase of molecules are hampered by the size limits of simulation systems and the (artificial) effects of system boundaries. One remedy to this problem is to use the *periodic boundary conditions* (PBC), in which particles in the central box are replicated in all directions to infinity. Particles moving across the box boundary re-enter the system from the opposite side. Different shapes of periodic boxes can be used. Their choice depends on the type of the system simulated, the structure of the molecule, and the total amount of solvent molecules required to fill the box.

Under PBC, the number of pairwise interactions is enormously increased because interactions not only between the “real” particles, but also between the real and the image particles have to be considered. For short-range interactions (such as the quickly decreasing Lennard-Jones potential, $\frac{1}{r^6}$), a cutoff distance r_c is employed. The cutoff distance has to satisfy the *minimum image convention* such that r_c is no more than half of the shortest box length. In this way, interactions between atoms and their images are prevented. For the long-range electrostatics interactions ($\frac{1}{r}$), the use of a cutoff leads to significant artefacts [143–145]. Instead, lattice summation methods such as the Ewald summation method are able to consider full electrostatics in an efficient manner.

In the Ewald method [146], the sum over all pairwise interactions is converted

into two rapidly converging series, namely the direct (real-space) sum and the reciprocal (Fourier) sum. A neutralizing charge density having exactly the same total but opposite charge centered at each point charge is introduced. Thereby, the electrostatic interactions between point charges are screened, and the long-range interactions can be safely neglected.

The total Coulomb potential then consists of three contributions:

$$V_{coul} = V_{direct} + V_{recip} + V_{self}. \quad (2.13)$$

The short-range Coulomb interactions of the screened charges (the *direct sum*) can easily be calculated using a cutoff in real space:

$$V_{direct} = \sum_{i \neq j}^N \frac{q_i q_j \operatorname{erfc}(\sqrt{\alpha} r_{ij})}{r_{ij}}, \quad (2.14)$$

where $r_{ij} = |\mathbf{r}_i - \mathbf{r}_j|$, α the cutoff range, and $\operatorname{erfc}(x)$ the complementary error function. Note that the screening function is a Gaussian.

To correct for the added charge density, a compensating charge density has to be included. Its contribution to the electrostatic potential is evaluated by solving the Poisson equation in reciprocal space using the Fourier transformed charge density [141].

$$\begin{aligned} V_{recip} &= \frac{1}{2V} \sum_i q_i \phi^c(r_i) \\ &= \frac{1}{2V} \sum_{k \neq 0} \sum_{i,j=1}^N \frac{4\pi q_i q_j}{k^2} \exp(i\mathbf{k}(\mathbf{r}_i - \mathbf{r}_j)) \exp(-k^2/4\alpha), \end{aligned} \quad (2.15)$$

where \mathbf{k} is the reciprocal lattice vector, $\phi^c(r_i)$ the electrostatic potential at a point r_i due to compensating charges. and V the volume of the unit cell.

Finally, the self-interaction introduced in V_{recip} has to be cancelled:

$$V_{self} = -\frac{\alpha}{\pi} \sum_{i=1}^N q_i^2. \quad (2.16)$$

By varying the shape of the Gaussian function, the rate of convergence of the two sums can be controlled. The optimal Ewald method was found to scale as $O(N^{3/2})$ [141].

An improvement to further speed up the algorithm to $O(N\log N)$ is to use the fast Fourier transform (FFT) in the reciprocal sum computation. For that purpose, the charges are mapped on a grid by interpolation, the so-called particle-mesh techniques [147].

A frequent purpose of simulations is to study phenomena in comparison between experiments and simulations. Observables from MD simulations are obtained by statistical mechanics: Each configuration sampled in trajectories can be seen as a microstate of the system (consists of the positions of particles and their momenta). The probability of a state follows the Boltzmann distribution, i.e. it is proportional to $\exp(-\frac{E}{k_B T})$ with the energy E of the state. Under the *ergodic hypothesis*, the expectation value of an observable averaged over an ensemble of configurations (ensemble average) is equivalent to the time average of the observable obtained from an experiment or a MD simulation. While in Monte Carlo (MC) simulations observables are computed on ensembles of structures lacking time information, MD simulations allow to study properties as a function of time. Essential for both MC and MD is the approximate sampling of the complete accessible phase space.

In MD simulations, configurations are generated as a function of time, the sampling on very long time scales follows according to the ergodic hypothesis the Boltzmann distribution. The thermodynamic average of an observable A is then obtained by simple averaging over the configurations or microstates of the system:

$$\langle A \rangle = \frac{1}{M} \sum_{i=1}^M A(t_i), \quad (2.17)$$

where M is the total number of sampled configurations. The statistical uncertainty of this average value is inversely proportional to the square root of the number of sampled points (if independent). If the system was simulated for a sufficient time and reached equilibrium, the calculated value can directly be compared to experiment.

2.2 Free energy calculations

In statistical mechanics, the free energy A is defined in terms of the canonical partition function Z ,

$$A = -k_B T \ln Z = -k_B T \ln \left\langle \exp \left(-\frac{E}{k_B T} \right) \right\rangle, \quad (2.18)$$

where Z is the sum of the Boltzmann weights of all possible microstates of the system. This sum is equivalent to the ensemble average of $\exp(-E/k_B T)$. While the Boltzmann factor is dominated by low energy states, an MD simulation preferentially samples high-energy regions in phase space. Thus, a direct calculation of the absolute free energy from simulations is rarely possible.

The problem can be largely simplified if one focuses on the free energy difference between two well-defined states (0 and 1) of the system instead of the absolute free energy of a particular state. In this case, one aims to solve $\Delta A = A_1 - A_0$, where A_0 is the initial state and A_1 is the final state,

$$\Delta A = -k_B T \ln \frac{Z_1}{Z_0}. \quad (2.19)$$

To allow a smooth (and in most cases unphysical) transition from A_0 to A_1 , usually a coupling parameter λ that varies from 0 to 1 is employed in the definition of the Hamiltonian of the system,

$$H(\lambda) = \lambda H_1 + (1 - \lambda) H_0. \quad (2.20)$$

Three methods are commonly used to solve ΔA using the method of MD simulations, namely the Free Energy Perturbation (FEP), the Thermodynamic Integration (TI), and the potential of mean force (PMF).

2.2.1 Free energy perturbation and thermodynamic integration

In FEP [148], the free energy difference is derived as the ensemble average of the Hamiltonian difference:

$$\Delta F = \sum_{\lambda=0}^{\lambda=1} -k_B T \ln \left\langle \exp \left(\frac{-(H(\lambda + \Delta\lambda) - H(\lambda))}{k_B T} \right) \right\rangle_{\lambda}. \quad (2.21)$$

In each step, separated by $\Delta\lambda$, only one λ -ensemble is used to obtain the free energy difference, so the two neighboring states λ and $\lambda + \Delta\lambda$ should be sufficiently close. It is recommended that the free energy changes for each step should not exceed $2 k_B T$ [149]. Both forward and backward calculations can be performed to measure the statistical uncertainty in the calculation.

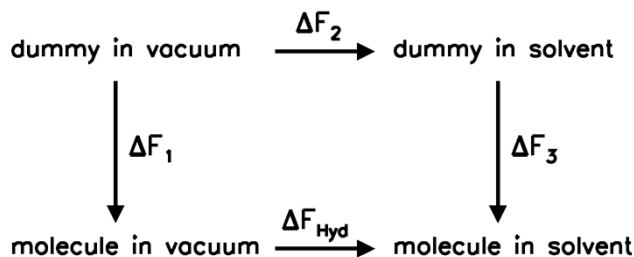


Figure 2.1: The thermodynamic cycle for calculating the free energy of molecular solvation.

Alternatively, the relative free energy can be obtained from an integral sum of free energy changes along the transition path defined by the coupling parameter λ . The derivative of the free energy can be rewritten as the ensemble average of the derivative of the Hamiltonian [149]. This method is called Thermodynamic Integration (TI) and reads as

$$\Delta F = \int_0^1 \frac{\partial F(\lambda)}{\partial \lambda} d\lambda = \int_0^1 \left\langle \frac{\partial H(\lambda)}{\partial \lambda} \right\rangle_{\lambda} d\lambda. \quad (2.22)$$

Like in FEP, the right hand side integral can be approximated by using successive discrete λ values with small intervals.

As a state function, the value of ΔF is independent of the path between the two states. One can make use of thermodynamic cycles and integrate along paths computationally more convenient. Such paths can be real physical/chemical processes or non-physical ones. An example of the thermodynamic cycle commonly used to calculate the hydration free energy of a molecule is shown in Fig. 2.1. “Dummy” is the molecule which has only intramolecular interactions for cavity creation but does not interact with its environment. From the cycle, we obtain $\Delta F_{Hyd} = \Delta F_3 - \Delta F_1 + \Delta F_2$. The free energies of the alchemical pathways ΔF_1 and ΔF_3 can easily be computed by letting the molecule disappear (switching off the nonbonded interactions of the molecule with the environment in the Hamiltonian), and ΔF_2 is zero.

2.2.2 Potential of mean force

For many problems not only the free energy difference between two states is required, but also the change in free energy as a function of a reaction coordinate, the so-called *potential*

of mean force (PMF). Firstly introduced by Kirkwood [150], the PMF is the average force of all microstates of the rest of a system on a selected, fixed set of atoms. It is defined from the average density of states $\langle \rho(\xi) \rangle$ along the chosen reaction coordinate ξ in reference to some arbitrary constants $W(\xi^*)$ and $\langle \rho(\xi^*) \rangle$ (e.g. the density of an ion along a path through an ion channel) [133].

$$W(\xi) = W(\xi^*) - kT \ln \left[\frac{\langle \rho(\xi) \rangle}{\langle \rho(\xi^*) \rangle} \right] \quad (2.23)$$

The ensemble-averaged density is obtained from the weighted Boltzmann average

$$\langle \rho(\xi) \rangle = \frac{\int d\mathbf{r} \delta(\xi'(\mathbf{r}) - \xi) \exp\left(-\frac{V(\mathbf{r})}{k_B T}\right)}{\int d\mathbf{r} \exp\left(-\frac{V(\mathbf{r})}{k_B T}\right)}. \quad (2.24)$$

The function $\xi'(\mathbf{r})$ converts the atomic coordinates \mathbf{r} into the reaction coordinate ξ which typically consists of only a few degrees of freedom. For reactions involving a high activation barrier ($> 1.5 k_B T$ [151]), the distribution function $\rho(\xi)$ does not converge in standard MD simulations due to insufficient sampling of the low energy region. Non-Boltzmann sampling techniques such as umbrella sampling [152] are required to solve this problem. In this method, a biasing potential (e.g. a harmonic function) confining the sampling region to the coordinate ξ_i is added to the original potential function,

$$V'(r) = V(r) + w_i(\xi) = V(r) + \frac{1}{2} K (\xi - \xi_i)^2 \quad (2.25)$$

A series of (window) simulations is performed using the modified potential along the reaction coordinate yielding a set of biased ensembles. To obtain the final underlying PMF, the results have to be unbiased and recombined by solving the free energy constant introduced to each window simulation. An efficient way to generate the unbiased PMF is the weighted histogram analysis method (WHAM) [153]. It constructs an optimal estimate of the unbiased distribution function as a weighted sum of all unbiased window distributions:

$$\langle \rho(\xi) \rangle = \sum_{i=1}^{N_w} n_i \langle \rho(\xi) \rangle_{(i)} \times \left[\sum_{j=1}^{N_w} n_j \exp\left(-\frac{w_j(\xi) - F_j}{k_B T}\right) \right], \quad (2.26)$$

where N_w is the number of biased window simulations, n_i is the number of independent data points in constructing the biased distribution function $\langle \rho(\xi) \rangle_{(i)}$ in window i .

F_j , which is the free energy constant associated with the introduced biasing potential w_i , is computed as:

$$\exp\left(-\frac{F_i}{k_B T}\right) = \int d\xi \exp\left(-\frac{w_i(\xi)}{k_B T}\right) \langle \rho(\xi) \rangle. \quad (2.27)$$

The two equations (2.26) and (2.27) have to be self-consistent. To do this, an initial guess of the free energy constants will be generated, and then the equations are solved iteratively until convergence is reached.

2.3 A semi-empirical proton transport method (Q-HOP MD)

Due to the abundant transfer of protons between different chemical moieties and the small mass of a proton particle, an accurate description of the motion of proton can only be achieved by quantum chemical techniques. However, as the computational cost of *ab initio* methods is huge, the size and the time scale of the system studied will be extremely limited. A semi-empirical method providing an efficient way to model the proton transfer (PT) process was proposed by Lill and Helms in a series of publications [140, 154, 155]. The PT reaction is modeled as an instantaneous process of migrating the proton from the donor molecule to the acceptor molecule. The transition probability for the proton hopping was fitted by an analytical expression to probabilities derived from the solution of the time-dependent Schrödinger equation for simplified systems. The latter include the donor-acceptor distance and the change in interaction energy of the donor-acceptor pair to the environment as variables.

This method was successfully applied to study PT in various biological systems, such as a hydronium ion in aqueous solution [140], the proton shuttle in green fluorescent protein [156], the proton exclusion mechanism in the Aquaporin-1 channel [157], and the protonation equilibrium of solvated acetic acid [158]. Recently, the parameterization was extended to PT between all titratable amino acids and thus the method allows also the study of proton hopping among protein residues.

Q-HOP was firstly implemented in the ARGOS simulation package [159], later in NWChem [160], and recently by us in GROMACS [161]. In the following sections, we present the methodology of the Q-HOP method, whereas details of the implementation

evaluations will be given in Chapter 6.

2.3.1 Potential of the proton transfer process

In general, the PT reaction may be described by the double-well shaped energy potential as a function of the proton transfer distance as shown in Fig. 2.2. The probability of a successful proton transfer event is coupled to the rate of barrier crossing in the energy potential surface from one minimum (the donor-bound state) to the next minimum (the acceptor-bound state).

The shape of the potential surface is largely influenced by two important factors: the distance between the donor and the acceptor, and the arrangement of other molecules in the system environment. As pointed out by Huggins [162] using a simple Morse function for Coulombic interaction and later by Lu et al. [163] and Lill et al. [164] using *ab initio* calculations, the height of central barrier of the double-well energy surface of a PT system in vacuum varied at different donor-acceptor distances. At a sufficiently small distance, the barrier even vanished. This corresponds to the case where a proton is symmetrically shared between the donor and the acceptor molecule. The PT barrier can be lowered further to that in vacuum, when ligand molecules such as water are involved, depending on their distances from the reaction site. Therefore, to provide a good approximation of the proton transfer, both the donor-acceptor distance as well as the momentary configuration of the system have to be considered.

2.3.2 The Q-HOP model

In the Q-HOP method, the PT reaction is modeled as an instantaneous process of migrating the proton from the donor molecule (D) to the acceptor molecule (A). The proton hopping probability is then estimated from the donor-acceptor distance (R_{DA}), the nature of the donor/acceptor molecules, and the energy difference between the two energy minima E_{12} (see Fig. 2.2). The latter can be approximated by adding the electrostatic influence (the instantaneous Coulombic interactions) of the environment to the energy difference between the two reaction states in vacuum E_{12}^0 [154]:

$$E_{12} = E_{12}^0 + (E_2^{env} - E_1^{env}) \quad (2.28)$$

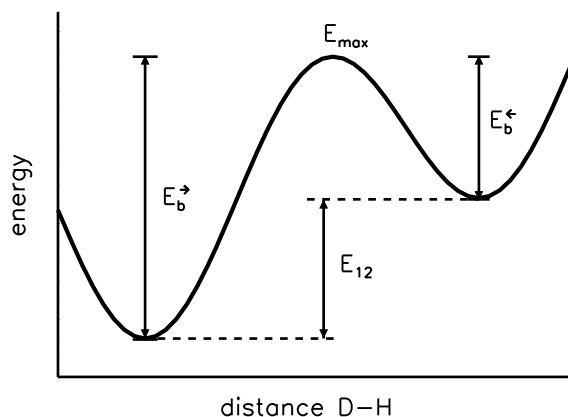


Figure 2.2: The general one-dimensional double-well potential of the proton transfer process as a function of the distance between the donor atom and the proton. The first minimum corresponds to the state with the proton bound to the donor, the second minimum to the state with the proton bound to the acceptor.

where E_{12}^0 is obtained from an empirical fit to the calculated energy barrier which depends only on distance R_{DA} . E^{env} is the Coulombic interaction between the reaction center and the rest of the system in the donor-bound state (state 1) and the acceptor-bound state (state 2).

$$E_{12}^0 = \alpha + \beta R_{DA} + \gamma R_{DA}^2 \quad (2.29)$$

$$E_1^{env} = \sum_{i \in \{D-H, A\}} \sum_{j \in \{env\}} \frac{q_i q_j}{4\pi\epsilon_0 |r_i - r_j|} \quad (2.30)$$

$$E_2^{env} = \sum_{i \in \{D, H-A\}} \sum_{j \in \{env\}} \frac{q_i q_j}{4\pi\epsilon_0 |r_i - r_j|} \quad (2.31)$$

Note that the coefficients in blue (α , β , γ) are tabulated parameters of the pairs of donor-acceptor chemical groups [140, 154, 155, 165]).

Depending on the distance R_{DA} and the interaction energy E_{12} of a PT reaction, three different cases have to be distinguished to calculate the proton transfer probability (see Fig. 2.3):

1. **TST regime:** For large distances R_{DA} and large energy differences E_{12} , the transition state theory (TST) [166] is used to estimate the free energy barrier for PT and

the transition probability [154]. The probability is calculated based on the modified rate equation taking into account the zero-point energy correction $\hbar\omega/2$ and the tunneling effect $\kappa(T)$:

$$p_{TST} = \kappa(T) \frac{k_B T}{2\pi\hbar} \exp\left(-\frac{E_b^\rightarrow - \hbar\omega/2}{k_B T}\right) \Delta t \quad (2.32)$$

E_b^\rightarrow is the forwarding barrier in the energy surface, which shows a quadratic dependence on E_{12} , whereas the coefficients S , T , and V are simple functions of R_{DA} :

$$E_b^\rightarrow = S(R_{DA}) + T(R_{DA})E_{12} + V(R_{DA})E_{12}^2 \quad (2.33)$$

$$S(R_{DA}) = s_A(R_{DA} - t_A)^2 + v_A \quad (2.34)$$

$$T(R_{DA}) = s_B \quad (2.35)$$

$$V(R_{DA}) = s_C \exp(-t_c(R_{DA} - 2\text{\AA})) + v_C \quad (2.36)$$

For the zero point energy, the motion of the proton is approximated using a quantum harmonic oscillator at the educt well. The values of $\hbar\omega/2$ show an exponential dependence on E_b^\rightarrow :

$$\hbar\omega/2 = f \exp(-gE_b^\rightarrow) + h \quad (2.37)$$

The tunneling effect is accounted for in the transmission coefficient κ as a ratio of the quantum transfer rate and the classical transfer rate, $\kappa = k_{QM}/k_{classical}$. It is estimated from E_M and the temperature T :

$$\kappa(T) = \exp(P(T) + Q(T)E_M + R(T)E_M^2) \quad (2.38)$$

$$P(T) = p_1 \quad (2.39)$$

$$Q(T) = q_1 + q_2 T + q_3 T^2 \quad (2.40)$$

$$R(T) = r_1 + r_2 T + r_3 T^2 \quad (2.41)$$

where $E_M = \min(E_b^\rightarrow, E_b^\leftarrow)$ is the minimum of the forward and the backward transfer barrier.

2. **Schrödinger regime:** When the PT barrier is insignificant due to small R_{DA} and E_{12} , transition state theory is no longer valid. By following the time evolution of the probability density of a proton by solving the time-dependent Schrödinger equa-

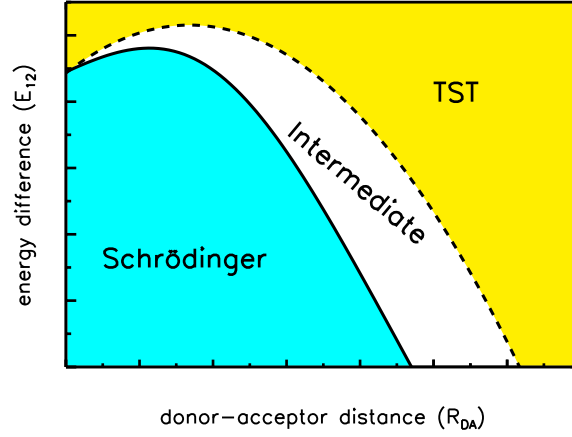


Figure 2.3: The three regimes in the Q-HOP model. Depending on which regime is valid, the proton transfer probability in Q-HOP is calculated either in the Schrödinger regime, in the TST regime, or by interpolation between the two.

tion, the probability of a proton crossing a barrier within a period of time can be obtained. This probability varies depending on R_{DA} and E_{12} . By fitting of the probabilities for different R_{DA} and E_{12} combinations, one obtains an empirical function to estimate the proton transfer probability in the Schrödinger regime [155]:

$$p_{SE} = (0.5 \tanh(-K(R_{DA})E_{12} + M(R_{DA})) + 0.5) \frac{\Delta t}{10 \text{ fs}} \quad (2.42)$$

$$K(R_{DA}) = k_1 \exp(-k_2(R_{DA} - 2.3 \text{ \AA})) + k_3 \quad (2.43)$$

$$M(R_{DA}) = m_1 \exp(-m_2(R_{DA} - 2.3 \text{ \AA})) + m_3 \quad (2.44)$$

Note that a characteristic time of 10 fs is introduced here, which is the observed time scale for the proton transfer process in a strongly hydrogen bonded system [155].

3. **Intermediate regime:** The validity limit for the TST regime, E_{12}^R , is defined as $\exp(\frac{E_b^{\rightarrow}}{k_B T}) \geq 100$, where the forward energy barrier E_b^{\rightarrow} is much larger than thermal fluctuations ($k_B T$). For the Schrödinger regime, E_{12}^L , the calculated probability is considered valid for $p_{SE} > 0.1$.

In the intermediate regime – i.e. between the TST regime and the regime where the transfer probability is best described by the Schrödinger approximation – the

transfer probability is linearly interpolated on a logarithmic scale:

$$\log_{10}p_{GAP} = \log_{10}p_{SE}(E_{12}^L) + \frac{\log_{10}p_{TST}(E_{12}^R) - \log_{10}p_{SE}(E_{12}^L)}{E_{12}^R - E_{12}^L}(E_{12} - E_{12}^L) \quad (2.45)$$

In a typical Q-HOP MD simulation, at each Q-HOP step (every 10 fs) the proton donors and the potential acceptors are identified. The proton transfer probability for each donor-acceptor pair is calculated. It is then compared to a random number to decide whether hopping occurs or not. If hopping is allowed, the system topology is updated by attaching the proton to the acceptor molecule and removing it from the donor molecule before the next MD step.

It should be pointed out that as each PT process performs an immediate change in the system configuration, a (short) period of inequilibrium is introduced. In addition, the energetic difference between the donor-bound state and the acceptor-bond state results in a non-conserved change in system energy upon PT.

Chapter 3

Electric Field Effects on Membranes: Gramicidin A as a Test Ground

Shirley W.I. Siu and Rainer A. Böckmann. *J. Struc. Biol.* 157 (2007), 545-556. ¹

Summary

Electric fields due to transmembrane potential differences or ionic gradients across the membrane are presumably crucial for many reactions across membranes or close to membranes like signal transduction, control of ion channels or the generation of neural impulses. Molecular dynamics simulations have been used to study the influence of external electric fields on a mixed gramicidin/phospholipid bilayer system. At high field strengths, formation of membrane electropores occurred both close and distal to the gramicidin. Gramicidin was found to stabilize the membrane adjacent to the protein but also at larger distances of up to 2–3 nm. As a result, membrane pore formation was found to be significantly suppressed for the mixed gramicidin/DMPC system. Moderate field strengths only weakly affected the structure and dynamics of the gramicidin. Spontaneous potassium passage events in external electric fields were observed for both the head-to-head helical conformation as well as for the double helical conformation of gramicidin A. The double-helical conformation was found to facilitate ion passage compared to the head-to-head helical dimer.

¹Reprinted from Journal of Structural Biology, Copyright (2006), with permission from Elsevier.

3.1 Introduction

Membranes play an important role in biology. Their permeability for water, ions and larger molecules as well as their influence on the structure and function of integral and peripheral membrane proteins are of crucial importance for almost all aspects of cell life. Electric field effects both on artificial lipid bilayer membranes as well as on cell membranes attract increasing interest. External electric fields induce local perturbations of vesicle or cell membranes, largely dependent on the field strength, and the pulse form and length. These perturbations are often followed by the formation of reversible hydrophobic or hydrophilic pores. The reversible electroporation of membranes is used to transfer drugs and gene DNA [167] into cells, for electrochemotherapy [168, 169], in electrogenetherapy [170], in vaccination [171, 172], and in RNA transfection [173, 174]. But also under physiological conditions, potential differences across membranes in the order of 200 mV corresponding to electric fields of 0.4 MV/cm are present. Membrane potentials play a crucial role e.g. for voltage-gated ion channels, or in mitochondrial protein import [175, 176], and drive central processes like the ATP synthesis (see e.g. [177, 178]). In protein import, membrane potentials are thought to drive the insertion of charged presequences and the opening and closing of the protein conducting pores [176]. In ATP synthesis, transmembrane potential differences of 150 mV or larger are necessary to drive the F_1F_0 -ATP synthase molecular motor [179]. It has further been speculated that local destabilization of cell membranes by electric fields followed by electropermeabilisation is the relevant mechanism in exocytosis [180] and may also play a role in apoptosis [181].

Studies of the effect of electric fields on cells, membranes, or lipid bilayers range back by almost 50 years: The observation of an *electrical breakdown* of membranes [182], the killing of bacteria by high electric fields [183], and the finding of short-lived permeability changes induced by electrical fields [184] were followed by numerous theoretical and experimental studies elucidating, e.g the influence of electric field strength and pulse forms and of the membrane composition on the mechanism of pore formation [185–187]. Recently, simulation studies on pure lipid bilayers revealed the molecular mechanism of electropore formation at the atomic level [34–36, 188–190].

Molecular dynamics (MD) simulations gave an unprecedented view of the first steps of electropore formation in lipid bilayers, starting with a both structurally and dynamically asymmetric tilting of the dipolar phospholipid headgroups, which depends

on the orientation of the bilayer inside the external electric field. This tilting is followed by the formation of a closed water file across the membrane often associated by lipid headgroup protrusions into the membrane. Finally a small (≈ 1 nm) hydrophilic pore is formed by intertwined lipid headgroups inside the hydrophobic core of the membrane [34–36, 190]. It was experimentally shown that addition of gramicidin to lipid bilayers significantly increases the voltage threshold to electroporation and the membrane area expansivity modulus [191]. However, the molecular interactions of membrane spanning proteins with the lipids causing membrane stabilization with respect to electric fields are largely unknown. Also the influence of membrane potentials on the structure and dynamics of membrane proteins remains elusive.

Here, we study the influence of moderate to large external electric fields on gramicidin A embedded in a dimyristoylphosphatidylcholine (DMPC) bilayer as a model system using the method of MD simulation. Gramicidin is a polypeptide antibiotic forming a channel selective for the transport of monovalent cations across membranes. Several crystal and NMR structures of gramicidin A are known to date (see [192] for a review), and its function as a cation channel has been studied in great detail both experimentally and by MD simulations (see e.g. [193–198]). The energetics of cation permeation can be obtained from MD simulations by computing the potential of mean force (PMF) along the channel axis (or the free energy profile) by umbrella sampling generating distributions of ion positions along the channel at fixed positions [199, 200]. Several other properties of this miniprotein have been studied as well, e.g. the lipid-protein interaction [201], the water permeability [196], or the importance of protein elasticity on water motion [194] and on ion permeation [202]. Gramicidin has also been used as a model system in studies of the effect of anesthetics on membrane channels [203] or as a test ground for molecular dynamics force fields [199].

In this study, we investigate the dynamics of this channel protein in different conformations subject to external electric fields and discuss the influence of this membrane protein on the adjacent and on the distal membrane structure. We demonstrate that the electropore formation in membranes is drastically influenced by the presence of gramicidin. Already for the dilute gramicidin/DMPC concentration investigated (1:63) the pore formation time is considerably increased with respect to a pure DMPC bilayer. Additionally, the transport properties of the gramicidin channel both for water molecules and for potassium ions in an external electric field are analyzed. Differences in the pro-

tein and water dipole moments between the head-to-head helical conformation and the double helical conformation of the gramicidin will be discussed.

3.2 Materials and methods

Gramicidin A (gA) mainly adopts two conformations which have been resolved by both X-ray crystallography and by NMR spectroscopy: a double-helical structure (DH) called the pore form and a head-to-head helical dimer conformation (HD) referred to as the channel form [192]. These two conformations are favored depending on the specific conditions [192], e.g. on the bilayer thickness [204], on the temperature, or the ion type [205]. The biologically active form is still a matter of debate [206–208]. In this study, both conformations were used to study the influence of external electric fields.

The initial conformations of the gA were taken from the PDB database: PDB entry 1AV2 for the double-helical structure [209] and 1MAG for the helical dimer [210]. A pre-equilibrated DMPC bilayer (kindly provided by Peter Tieleman) was used as a starting structure and equilibrated for another 4 ns, applying a different force field (see below). The model system (Fig. 3.1 A) consisted of a gramicidin embedded in this DMPC bilayer of 125 lipids solvated with 6,140 water molecules.

We followed the procedure of [211] to insert the gA into the bilayer: Firstly, the protein was transferred to the center of the bilayer with the channel axis parallel to the normal of the bilayer. Lipids completely overlapping with the protein were removed and the volume of the protein defined by its molecular surface was generated. Then, a simulation was performed to expel atoms from inside the protein volume by applying forces normal to the protein surface. Five water molecules were placed inside the gramicidin channel. This procedure was performed both for the DH and the HD structures separately to obtain the initial systems.

The initial configurations were energy-minimized using the steepest descent algorithm (3000 steps), followed by a MD run with harmonic position restraints (force constant $1000 \text{ kJ mol}^{-1} \text{ nm}^{-2}$) applied to all heavy atoms of the protein for 200 ps. This procedure allowed the lipids and the water molecules to relax around the protein after its

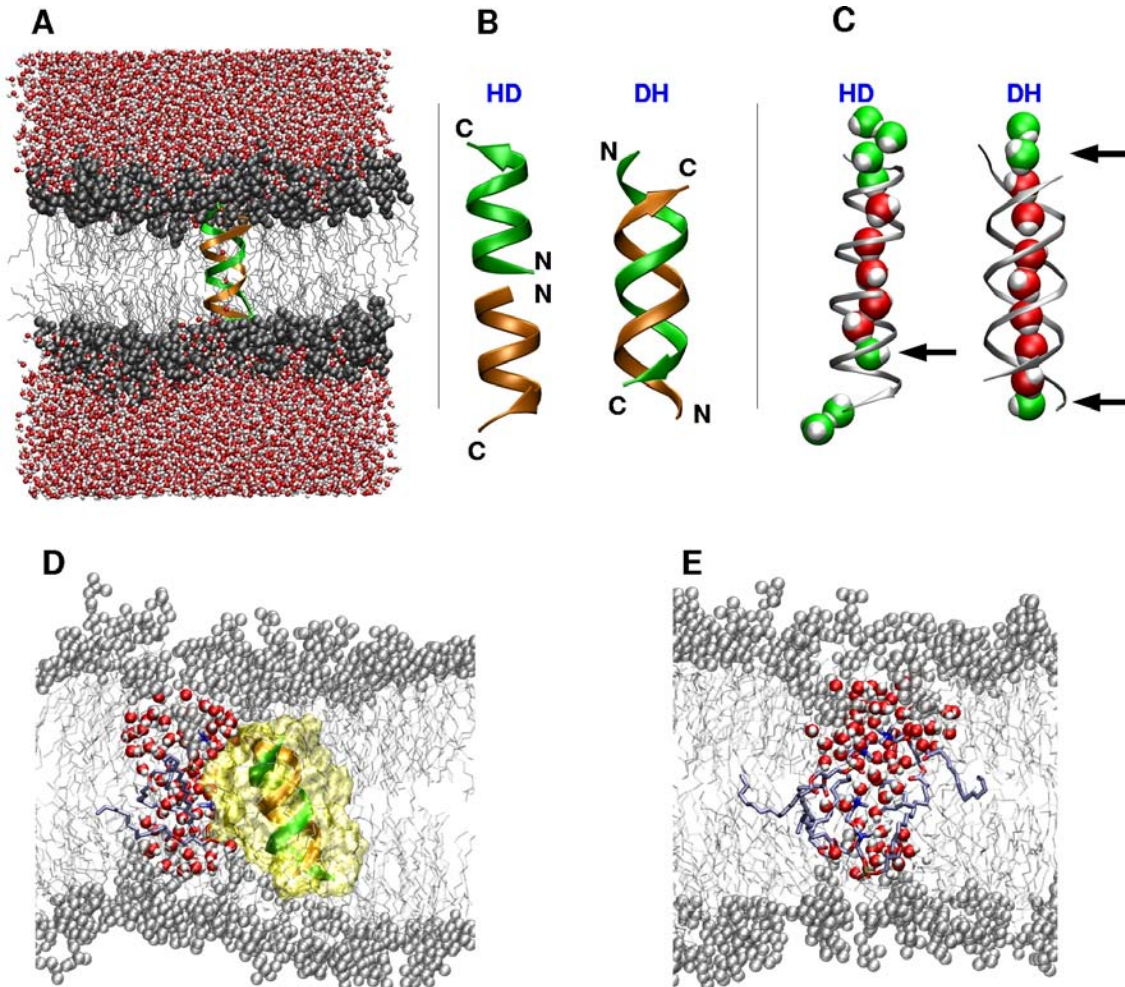


Figure 3.1: Simulation system (A). All simulations have been started from a gramicidin A in HD or DH conformation (B) embedded in a fully hydrated DMPC lipid bilayer. The simulation systems consist of more than 30,000 atoms. To simulate cation passage the green colored water molecules (C) have been replaced by a potassium cation in separate simulations. For cations positioned in the upper entrance an external electric field pointing downwards has been applied and vice versa for cations placed at the lower channel entrance. Those positions marked by an arrow led to complete cation passage. Figs. (D) and (E) show pore formation events close to the gramicidin (DH, in surface representation) and in a pure phospholipid bilayer. Lipids with headgroups protruded into the hydrophobic core of the bilayer are highlighted in blue, pore water molecules in red.

insertion. The systems were pre-equilibrated for 10 ns with constraints on bonds to H-atoms only.

To examine the effects of external electric fields on the gA and its surroundings, further simulations were performed based on the equilibrated systems. Electric fields of strength -0.20 V/nm, 0 V/nm, and 0.20 V/nm were applied normal to the membrane plane. Each simulation (for DH and HD) was run for 20 ns. Results were compared to the equilibration without external electric field and to a 16 ns simulation of a pure DMPC bilayer (128 lipid molecules). In a second setup we added K^+Cl^- at a concentration of 460 mM (in the solvent) at random positions to the solvent phase of the simulation system and analyzed the ion distribution at a field strength of $E = 0.2$ V/nm (40 ns trajectory). In order to accelerate the passage of potassium ions through the gramicidin channel ten simulations were started with one cation placed at different positions close to or inside the channel entrance (at 460 mM K^+Cl^- concentration). The respective starting positions for the cations are shown in Fig. 3.1 C.

Membrane electroporation was studied from 18 simulations at field strengths 0.3 and 0.35 V/nm for a pure DMPC bilayer (128 DMPC molecules, approximately the same dimensions of the periodic box as for the mixed system) and for the gA/DMPC system (gA in DH conformation). The pore formation time was defined as the time at which a closed water file was formed across the membrane.

The total simulation time adds up to ≈ 300 ns.

All simulations were performed using the GROMACS package [161, 212], applying the OPLS/AA force field [125] for the protein and the TIP4P water model [213]. For the DMPC molecules, we used the Berger force field [128], applying however the OPLS combination rules for the mixed Lennard-Jones parameters instead of the GROMOS combination rules (see also [214]). Since the formyl and the ethanolamide groups of gramicidin A were not predefined in the force field, they were created by assigning the force field parameters of the most similar groups in other amino acids.

Periodic boundary conditions were used in all directions. The system was coupled to a temperature bath at 310 K separately for the protein, the lipids, and the water

molecules with a coupling constant of 0.1 ps^{-1} [142]. As for the pressure, semi-isotropic coupling was adopted (pressure coupling separately for the lateral and for the normal direction) with a coupling time $\tau_p = 1 \text{ ps}$. The isothermal compressibility was set to $4.5 \times 10^{-5} \text{ bar}^{-1}$. Bonds to H-atoms were constrained using the LINCS [215] or the SETTLE algorithm [216], allowing for an integration step size of 2 fs. The non-bonded pair list was generated every 10 steps with a cutoff at 1.0 nm. For the short range vdW interactions, a cutoff distance of 1.0 nm was used. In treating the long-range electrostatics, the Particle-Mesh Ewald (PME) method with a grid spacing of 0.12 nm and cubic interpolation was adopted. Atom positions were written every 1 ps.

In the MD simulations, an electric field was applied along the membrane normal z , i.e., perpendicular to the DMPC bilayer surface. The field \mathbf{E} is defined as the gradient of the potential Φ ,

$$E_z = -\frac{\partial}{\partial z}\Phi. \quad (3.1)$$

Tin-foil boundary conditions were applied [217]. The simulation conditions ensure a potential difference of $\Delta\Phi = \mathbf{E} \cdot \mathbf{d}$ across the simulation box with box vector $\mathbf{d} = (d_x, d_y, d_z)$. The potential drop $\Delta\Phi_m$ across the membrane is given as

$$\Delta\Phi_m = \left(1 + \frac{d_w \epsilon_m}{d_m \epsilon_w}\right)^{-1} \Delta\Phi. \quad (3.2)$$

Inserting a dielectric constant for water of $\epsilon_w = 78$ and of $\epsilon_m \approx 3$ for the membrane [36], about 93% of the total potential difference $\Delta\Phi$ drops across the membrane (water slab thickness $d_w \approx 4.5 \text{ nm}$, thickness of the hydrophobic core of the membrane $d_m \approx 2.2 \text{ nm}$).

The cross-sectional area of the gramicidin channel along the membrane normal (binning size 0.15 nm) has been determined by applying two-dimensional Voronoi tessellation analysis [218] for all protein and lipid atoms. The average gramicidin area was computed to 232 \AA^2 for the HD conformation and 244 \AA^2 for the DH conformation (after averaging along the membrane normal and over 20 snapshots of the respective equilibration simulations).

A measure of the ordering of the lipid acyl chains is given by the order parameter

S_{ii} , defined by [94]

$$S_{ii} = \frac{1}{2} \langle 3 \cos^2 \theta_i - 1 \rangle \quad (i = x, y, z), \quad (3.3)$$

where $\langle \cos^2 \theta_i \rangle$ is the time average of the angular fluctuations of the i th molecular axis and the bilayer normal. In the simulations, a united-atom model for the acyl chain carbons lacking explicit hydrogen atom positions has been used. Therefore, the molecular axis is defined as the vector connecting the two acyl chain carbons C_{n-1} and C_{n+1} . In this way, no order parameters were obtained for the outermost carbon atoms C_1 and C_{14} (see also [219]). Experimentally, the deuterium order parameter S_{CD} is measured. It is connected to the above order parameter by the following relation:

$$S_{CD} = \frac{2}{3} S_{xx} + \frac{1}{3} S_{yy}. \quad (3.4)$$

3.3 Results and discussion

3.3.1 Electric field effects on the membrane

Electric fields of different strengths (0.2–0.35 V/nm) were applied on the mixed gramicidin/DMPC system and on a pure DMPC bilayer to examine their respective influence on the structure and function of the gramicidin, on the lipid environment, and to elucidate the influence of the membrane channel on the stability of the membrane.

Area per lipid

The pure DMPC bilayer adopts an area per lipid of $61.6 \pm 0.7 \text{ \AA}^2$ (see Table 3.1), in good agreement with experimental values for the area per lipid of pure DMPC bilayers at 310 K which range from 60 \AA^2 to 66 \AA^2 [220–222]. For the gramicidin A (DH conformation) embedded in the DMPC bilayer, the size of the simulation box was $6.22(\pm 0.06) \text{ nm} \times 6.22(\pm 0.06) \text{ nm} \times 8.38(\pm 0.15) \text{ nm}$, resulting in $57.9(\pm 1.1) \text{ \AA}^2$ for the area per lipid (59.3 \AA^2 for the HD conformation, subtracting the area of gA in the xy plane, see Methods), i.e., the average area per lipid for DMPC is decreased by $\approx 5\%$ after insertion of gramicidin. External electric fields show no significant influence on the area per lipid. Previous studies applying different lipid force fields showed a too large area per lipid (67 \AA^2 in [199], $\approx 70 \text{ \AA}^2$ in [223]) or fixed the area per lipid [224] at a predefined value.

Table 3.1: Area per lipid in simulations of a pure DMPC bilayer (DMPC) and of the gramicidin/DMPC system (DH, HD) at different external electric field strengths.

System	EF (V/nm)	area per lipid (\AA^2)
DMPC	0.0	61.6 \pm 0.7
DH	0.0	57.9 \pm 1.1
	0.2	57.8 \pm 0.8
	-0.2	58.2 \pm 0.7
	0.0	59.3 \pm 0.8
HD	0.2	59.3 \pm 0.7
	-0.2	58.3 \pm 1.3

Lipid order parameters

As a measure of the lipid acyl chain ordering we determined the (deuterium) lipid order parameters $|S_{CD}|$ [94] at various distances of the gramicidin. Overall, for the pure DMPC lipid bilayer the values are slightly below those determined in NMR experiments (green symbols and green line in Fig. 3.2 [225, 226]).

The deuterium lipid order parameters of those lipids in close proximity to the gramicidin in HD conformation (gray lines in Fig. 3.2) show only small deviations from the order parameters derived for a pure DMPC bilayer (diamonds); an average order (sn-1 and sn-2, average taken over carbon atoms $C_2 - C_{13}$) of 0.18 (close to gA) vs. 0.182 (pure DMPC) is observed. An order decrease is seen for carbons close to the headgroup which is more pronounced for the sn-1 chain. For lipids adjacent to the gramicidin in DH conformation (not shown), this decrease is more pronounced, the average order of the sn-1 chain decreases from 0.19 for the pure DMPC bilayer to 0.17 for the DH/gA system.

Hydrocarbon chains from the second shell around the protein (dashed line) and the residual lipids show a significant increase of order especially for the tail carbons close to the bilayer center. This is in contrast to a previous study on the 1 ns timescale reporting *increased* lipid order parameters adjacent to the protein [227] and a negligible effect for more remote lipids.

The decreased lipid order parameters close to the gramicidin and the increased order parameters distal to the gramicidin are in accord with NMR data for the sn-2 chain of a mixed DMPC/gramicidin A system [225]: At 15 wt % gramicidin (red line, correspond-

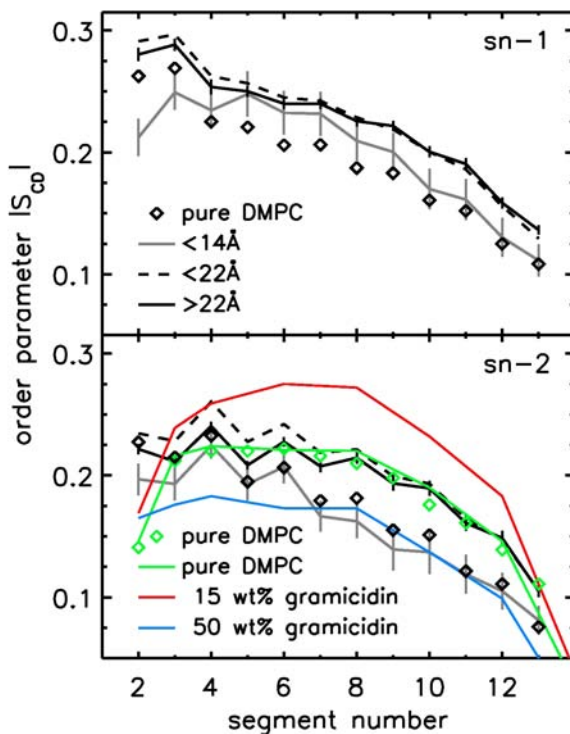


Figure 3.2: Hydrocarbon-chain order parameters of DMPC molecules around gramicidin A in HD conformation, separately for the sn-1 and the sn-2 chain of lipids close to the protein (gray line, lipid headgroups within approx. 14 Å distance of gramicidin channel), of the lipids in a second shell around the protein (dashed line), and of the residual lipids with a distance larger than 22 Å from the channel (solid black line). Errors are shown only for order parameters of close and distal lipids for clarity. Additionally shown are NMR data for the sn-2 chain of a pure DMPC system (green symbols [226] and green line [225]) as well as of mixed DMPC/gA systems ([225], red and blue lines). Distances are measured between the carbon atom at position 2 of the respective phospholipid glycerol group and the channel entrances. The latter are defined by the centers of mass of the backbone oxygens of residues A8, A10, A12 and B8, B10, B12 for the HD conformation.

ing to a lipid:gA ratio of 15:1) the overall order of the lipid acyl chains was increased while it was decreased for 50 wt % gramicidin (blue line, lipid:gA ratio of 3:1). The decrease in order for adjacent lipids was interpreted [225] by a disordering effect due to the filling of spaces between amino acid side-chains by the boundary lipid acyl chains. The neighbored lipids then form a smooth surface for the more distal lipids.

The change in the lipid order parameter is accompanied by a change in the thickness of the lipid bilayer (measured as the average distance between the phosphates of both monolayers): the membrane adjacent to the gramicidin has a thickness of $3.26 \pm$

Table 3.2: Membrane thickness in different lateral separations from the gramicidin (region 1: <1.4 nm; region 2: <2.2 nm; region 3: >2.2 nm).

	DH (nm)	HD (nm)	pure DMPC (nm)
region 1	3.26 ± 0.14	3.26 ± 0.10	3.50 ± 0.02
region 2	3.67 ± 0.07	3.58 ± 0.08	3.50 ± 0.02
region 3	3.73 ± 0.09	3.65 ± 0.05	3.50 ± 0.02

Distances are measured between the carbon atom at position 2 of the respective phospholipid glycerol group and the channel entrances. The latter are defined by the centers of mass of the backbone oxygens of residues A8, A10, A12 and B8, B10, B12 for the HD conformation, and of residues A3, A5, B14 and B3, B5, A14 for the DH conformation.

0.10 nm (similar for both gA conformations, see Table 3.2), about 0.25 nm less than a pure DMPC bilayer. The membrane thickness increases, however, to about 3.7 nm at larger distances from the membrane channel. Thus the hydrophobic thickness of DMPC (≈ 2.2 nm) does not fit to that of the gramicidin dimer, different from what has been expected from structural comparison [228]. By thinning, the DMPC bilayer adjusts to the protein hydrophobic region.

Pore formation in pure DMPC vs. gramicidin/DMPC membrane

We investigated the time until a first electropore is formed, i.e. the pore formation time, for pure DMPC lipid bilayers and for the system containing gramicidin in conformation DH. Experimentally, it is known that gramicidin at peptide/lipid ratios of 1:500 (for the sample) or larger significantly increases the electroporation voltage threshold [191] (by 16% at a concentration of 1:500 applying rectangular voltage pulses of defined length on giant unilamellar vesicles). At this concentration (and assuming that the concentration of the sample is retained in the mixed bilayer), the gramicidin itself only occupies $\approx 0.5\%$ of the total area. Including adjacent lipids the fraction of area modified by the gramicidin increases to roughly 2.5%, still small compared to its influence on the electroporation. Thus a stabilizing effect of this channel protein also on more distal parts of the membrane appears probable.

In total, 18 simulations were carried out each for up to 17.5 ns at two different field strengths (0.3 and 0.35 V/nm), 8 for the pure DMPC bilayer system (see Methods section) and 10 for the mixed DMPC/gramicidin A system (DH conformation). Pores could

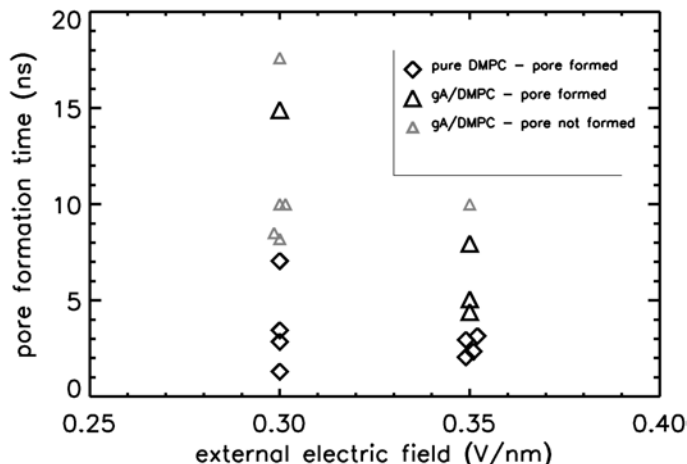


Figure 3.3: Pore formation times observed in MD simulations for a pure DMPC lipid bilayer (black diamonds) and for a mixed gramicidin/DMPC system (black triangles, gramicidin in DH conformation) at two different field strengths (0.3 and 0.35 V/nm). Small gray symbols denote the simulation lengths of further simulations in which pore formation could not be observed. The total simulation time exceeds 120 ns.

be observed in all simulations of the pure DMPC bilayer and in four simulations of the mixed system. Two out of four pores for the mixed gA/DMPC system formed close to the gramicidin. Typical snapshots of the initial phase of membrane pore formation are shown in Fig. 3.1 for a pore formed along the gramicidin surface (D) and for a pore in a pure DMPC bilayer.

The pore formation times (black symbols) as well as the simulation lengths for those simulations without pore formation (gray symbols) at the accessible simulation times are summarized in Fig. 3.3. At both investigated field strengths, the pore formation for the gA/DMPC system (average pore formation time $\bar{\tau}_{0.30} \geq 11.5$ ns at 0.3 V/nm, $\bar{\tau}_{0.35} \geq 6.9$ ns at 0.35 V/nm) is significantly suppressed with respect to the pure DMPC bilayer ($\bar{\tau}_{0.30} = 3.7$ ns, $\bar{\tau}_{0.35} \geq 2.6$ ns), the pore formation times are at least a factor of two larger. Thus gramicidin stabilizes the membrane with respect to enhanced membrane potential differences.

3.3.2 Gramicidin A in an external electric field

The influence of an external electric field on gramicidin A was analyzed only for moderate field strengths ($E = \pm 0.2$ V/nm) for which no electroporation was observed within

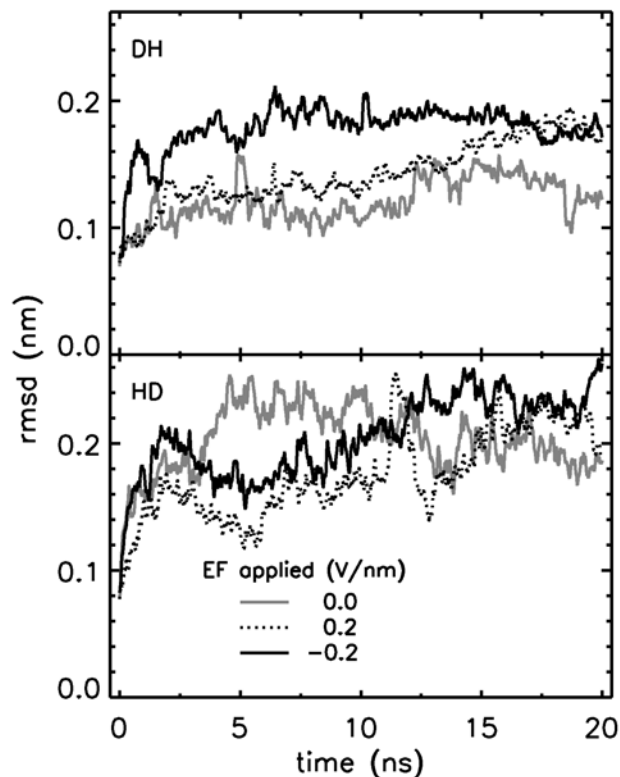


Figure 3.4: Root mean square deviation (rmsd) of the gramicidin A in DH and HD conformation from the respective equilibrated structure in response to applied external electric fields of given strength. The rmsd was calculated for the complete peptide after fit to the backbone.

the simulation time of 20 ns. Fig. 3.4 shows the root mean square deviations (rmsd) of gramicidin A in the two conformations from their (equilibrated) starting structures as a function of simulation time separately for the simulations at different field strengths (gray: $E = 0 \text{ V/nm}$, dotted: $E = 0.2 \text{ V/nm}$, black line: $E = -0.2 \text{ V/nm}$). For all investigated field strengths and conformations, the structure of gramicidin A is retained. Deviations in the rmsd curves reflect side-chain conformational changes mainly of Trp.

The dynamics of the peptide was accessed by calculating the root mean square fluctuations (rmsf) for all amino acids (see Fig. 3.5). As expected, the largest rmsf values are observed at the capping regions close to the hydrophilic headgroup region of the lipid bilayer, i.e. residues For1, Val2, Gly3, Ala4, Trp16, Eta17 for DH gA, and residues Trp13, Trp16, Eta17 for HD gA (formyl and ethanolamide groups abbreviated as For and Eta, respectively). These are the residues guarding the entrance and exit of the ion-conducting channel. Motion of the Eta, together with the neighboring residues, in closing and opening the gA channel was frequently observed. The fluctuations do not vary significantly

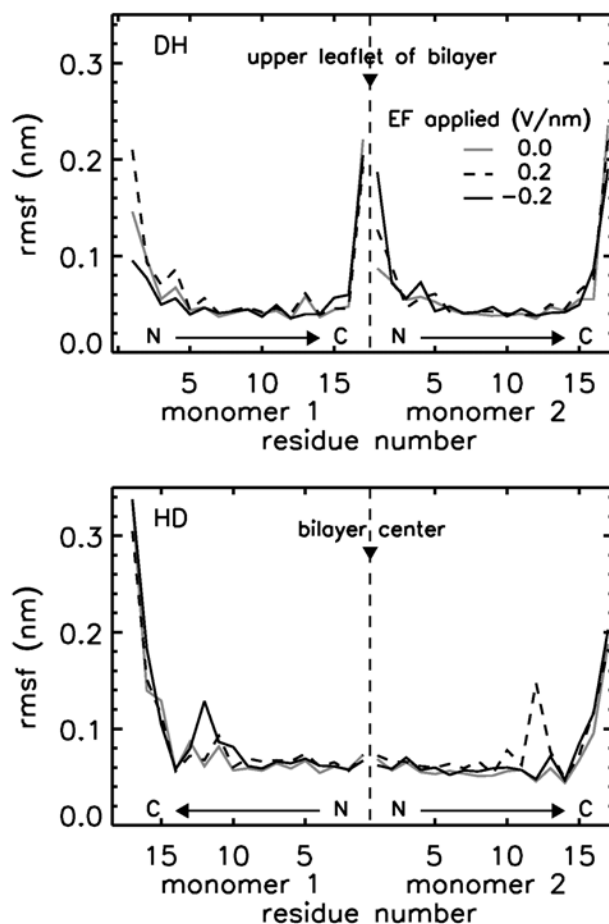


Figure 3.5: Root mean square fluctuations (rmsf) of the gramicidin A in DH and HD conformation from the respective equilibrated structure in response to applied external electric fields of given strength. The rmsf has been calculated over the full simulation period of 20 ns.

upon application of external electric fields.

Dipole moments

The dipole moments of the two gA conformations differ significantly (see Table 3.3 and Fig. 3.6). For the intertwined helical structure (DH), the two monomers possess dipole moments of similar magnitude (taken normal to the membrane, 10–12 D) but of opposite direction resulting in a total protein dipole moment of ≈ 0 D. With external electric field switched on, the dipole moments of both monomers are increased by 0–3 D in the

Table 3.3: The average dipole moment of the gramicidin monomers and the total protein dipole moment (given in Debye, averaged over 20 ns).

	EF (V/nm)	monomer 1 (D)	monomer 2 (D)	total (D)
DH	0.0	-11.44 ± 1.64	10.52 ± 1.40	-0.91 ± 2.09
	0.2	-11.44 ± 1.55	12.57 ± 1.88	1.14 ± 2.53
	-0.2	-12.49 ± 1.60	7.81 ± 2.01	-4.68 ± 2.07
HD	0.0	2.93 ± 2.58	1.08 ± 2.02	4.01 ± 3.70
	0.2	4.41 ± 2.55	5.22 ± 3.02	9.64 ± 3.00
	-0.2	-4.44 ± 2.70	-1.33 ± 2.63	-5.76 ± 3.52

respective direction of the applied field.

For the head-to-head helical dimer (HD), both monomers possess a slightly positive dipole moment (total dipole moment of 4 D). External electric fields normal to the membrane induce a larger change of the dipole moment of the monomer close to the respective anodic leaflet of the membrane.

Also the DMPC lipids re-orient in the applied external fields: the absolute value of the average dipole moment of DMPC phospholipids normal to the membrane of 7.5 ± 0.2 D is increased by ≈ 0.8 D or decreased by 1.3 D for fields directed parallel or anti-parallel to the lipid dipoles, respectively. The dipole moment of the lipids in each monolayer is counter-balanced by orientation of water dipoles in the lipid headgroup region (see Fig. 3.7), resulting in a positive membrane potential (not shown, see also [229]).

As can be seen in Fig. 3.7, the water file inside the gramicidin channel in HD conformation is highly oriented even without external electric field, similar as found in previous studies [200, 230]. The water file adopts an orientation directly opposed the weak protein dipole moment. Water molecules close to both channel entrances have a vanishing dipole moment normal to the membrane (see Figs. 3.7 and 3.8). In contrast – in the DH channel – two opposite orientations of the water chains exist simultaneously, occupying half of the channel each.

Frequent cooperative flipping of the channel water molecules by 180° is observed for the DH conformation, resulting in large fluctuations of the total dipole moment of the water file (for $E = 0.0$ V/nm, see Fig 3.8). On the contrary, the water file in the HD

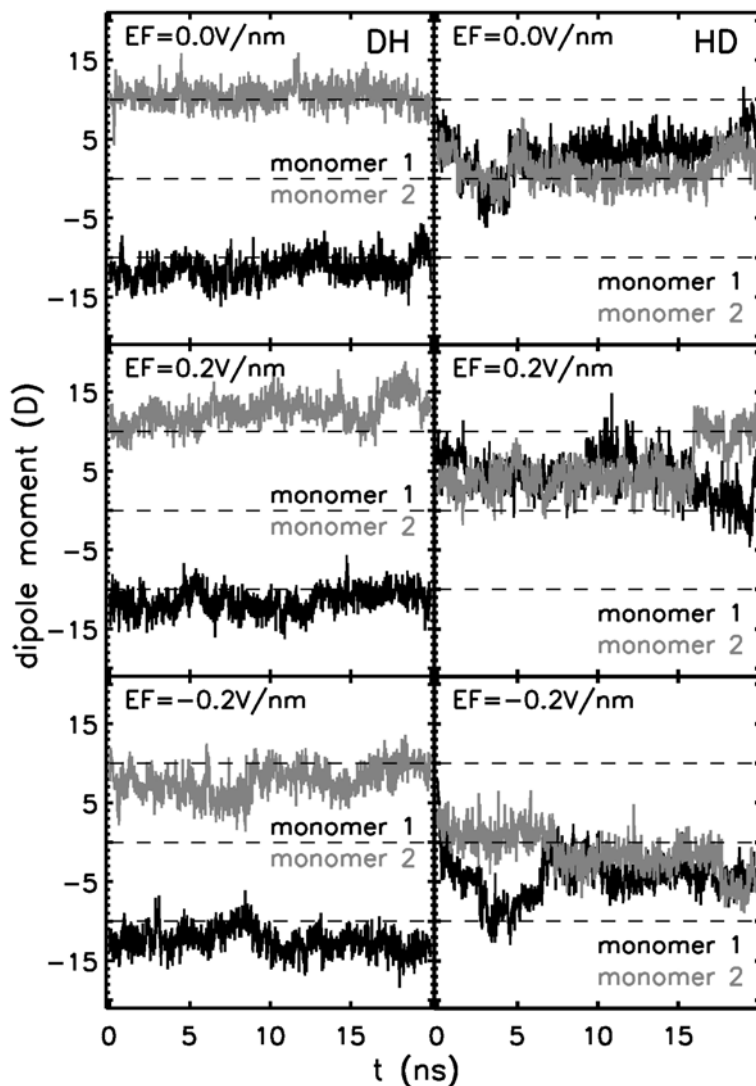


Figure 3.6: The changes in the monomer dipole moment normal to the membrane over the simulations. Shown are the dipole moments of the two monomers separately for the two gramicidin A conformations. The dashed black lines are to guide the eyes.

channel exhibits a strong negative dipole moment. Two almost complete albeit very short transitions of the channel water dipole moment are observed on the simulation timescale of 20 ns (see Fig. 3.8). A transition may be hindered by the opposed dipole moment of the gramicidin.

With external electric field ($E = 0.2 \text{ V/nm}$), the dipole moment of the water file for

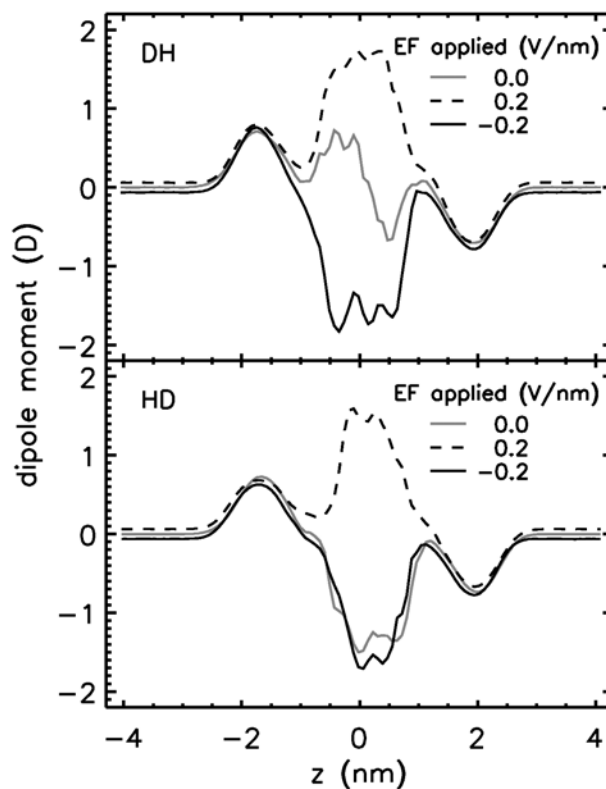


Figure 3.7: Average dipole moment of all water molecules along the z -axis (normal to the membrane) with and without external electric fields.

both the DH gA and the HD gA orient completely in field direction on the timescale of 0.1 ns.

A summary of the protein and water file dipole moments for the two different gA conformations (no external electric field) is shown in Fig. 3.9: In HD, the two monomers on top of each other favor a similar dipole orientation (black arrows). Accordingly, the water file dipole (gray arrow) in gA HD adopts the reverse orientation. In contrast, the intertwined monomers in the DH conformation energetically favour opposite large dipoles. These monomer dipoles cancel each other, that allows the confined water molecules to adopt the respective preferred orientations of the water molecules close to the channel entrances. The orientation of these water molecules is determined by the phospholipid headgroups.

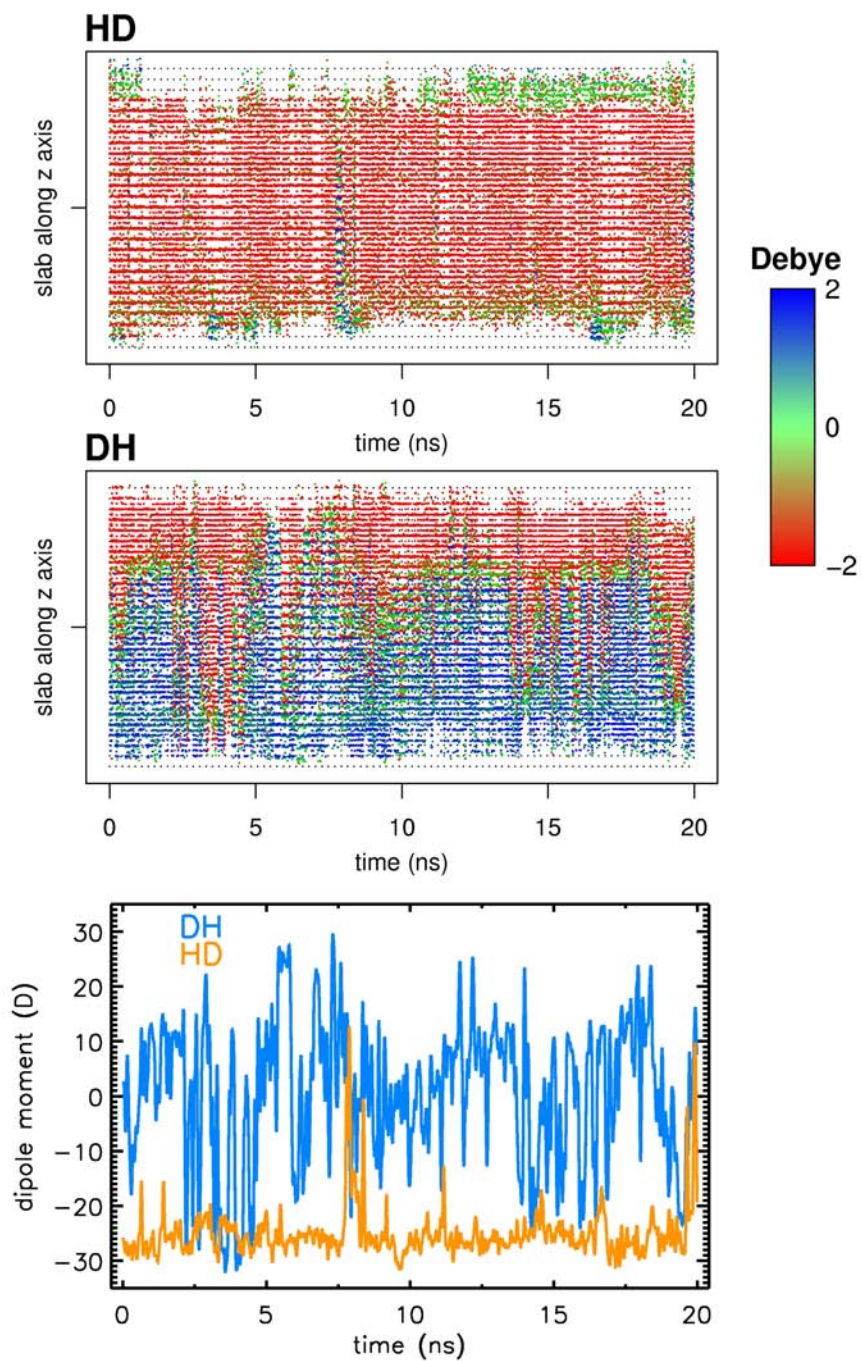


Figure 3.8: Color-coded dipole moment (in Debye) of water molecules confined inside the gramicidin channel without external electric field. The dipole moment has been calculated for slabs of 1 Å thickness perpendicular to the membrane normal. The lower panel shows the sum of the dipole moments of these water molecules separately for both gramicidin conformations.

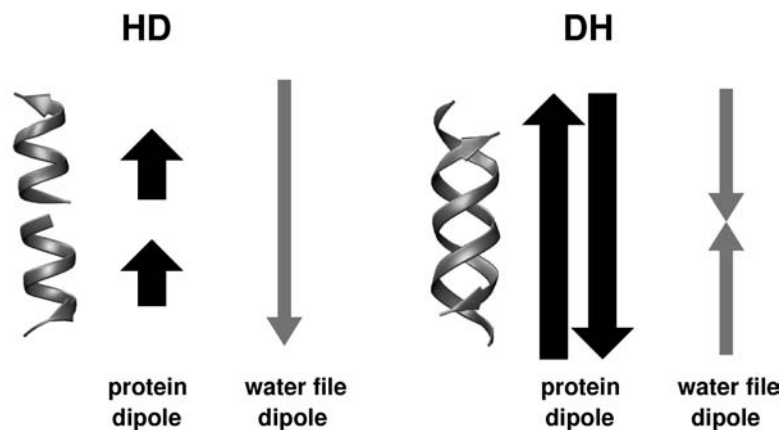


Figure 3.9: Schematic drawing of the protein and water file dipole moments for the two different gramicidin conformations (no external electric field). The gramicidin monomer dipole moments are shown as black arrows, those of the water molecules inside the channel as gray arrows.

Water permeation

Due to the highly collective motion of water molecules inside the channel [196] the water diffusion coefficient depends strongly on the status of the channel entrances, i.e. whether they are open or blocked by e.g. phospholipid headgroups or by the ethanolamide groups. The latter were found to block one or both entrances of the DH gA for 14% of the simulation time ($E = 0 \text{ V/nm}$) and of the HD gA even for 97% (see Table 3.4). For DH, the blockage times are increased in the presence of external electric fields. The channel water diffusion coefficients show only weak dependence on the conformation of the gramicidin or on external electric fields. The diffusion coefficient is larger by $\approx 50\%$ inside the DH channel compared to the HD channel (Table 3.4).

Spontaneous water passages were observed in all simulations, i.e. channel water eventually exited from either side of the channel, but only one full permeation event (in DH gA with $E = 0.2 \text{ V/nm}$) was found. Twice as many water passages were found for the DH (6) conformation as compared to HD gA (3). For the DH gA, the spontaneous water passages amount to only about 35% of what has been reported earlier [196]. In contrast, for the HD conformation, no water molecules left the channel in the former study [196]. Reasons for this discrepancy may be due to the different force fields (GROMOS vs. OPLS/AA) or due to insufficient sampling of the channel opening or closing.

Table 3.4: Diffusion coefficient of water molecules confined to the gramicidin channel and spontaneous water passage events.

	EF (V/nm)	diffusion coef. ($10^{-6}\text{cm}^2\text{s}^{-1}$)	water passages	% opened
DH	0.0	1.58 ± 0.15	6	86
	0.2	1.52 ± 0.18	8	54
	-0.2	0.80 ± 0.07	2	14
HD	0.0	1.05 ± 0.08	3	3
	0.2	1.24 ± 0.06	4	7
	-0.2	0.95 ± 0.08	1	3

The diffusion coefficients have been computed from the slope of the mean square displacement of the water molecules as a function of time (between 10 ps and 100 ps). Additionally, the percentage of simulation time with both channel entrances opened is given in the last column. A channel entrance was defined as closed if the distance between the center of mass of the ethanolamide group and the channel entrance was less than 3 Å.

Ion permeation in external electric fields

During a 40 ns simulation with applied external electric field ($E = 0.2\text{V/nm}$) and a K^+Cl^- concentration of 460 mM no ion passage through the gramicidin A channel (DH conformation) could be observed. Passage of potassium ions on the accessible timescale was made feasible only after pre-insertion of one cation at defined positions at the channel entrance (see Fig. 3.1 C). Without external electric fields all pre-inserted cations left the channel entrances on timescales of a few hundred picoseconds. With external field ($E = 0.2\text{V/nm}$) only in three out of ten simulations (three DH gA and seven HD gA starting conformations) with different starting conditions the cation passed the channel. Two passages through the DH gramicidin and one through the HD gramicidin are shown in Fig. 3.10: In the case of the cation placed at the lower entrance of DH, we observed a slow, step-wise passage of the cation through the channel on a timescale of 10 ns (Fig. 3.10 A). For the cation placed at the upper entrance with reversed field, the cation passage is considerably faster ($\approx 1.3\text{ns}$, not shown). For both permeation events through DH gA, two water molecules are dragged by the cation with an orientation reverse to the applied electric field.

Only in one out of seven simulations with the cation pre-inserted deeply into the channel (marked by an arrow in Fig. 3.1 B), spontaneous passage through the HD gA was observed. Due to closure of the lower entrance of the HD channel (Fig. 3.10 B) by the ethanolamide group no water molecules could be dragged by the cation during its passage. Thus, after passage, the channel is empty.

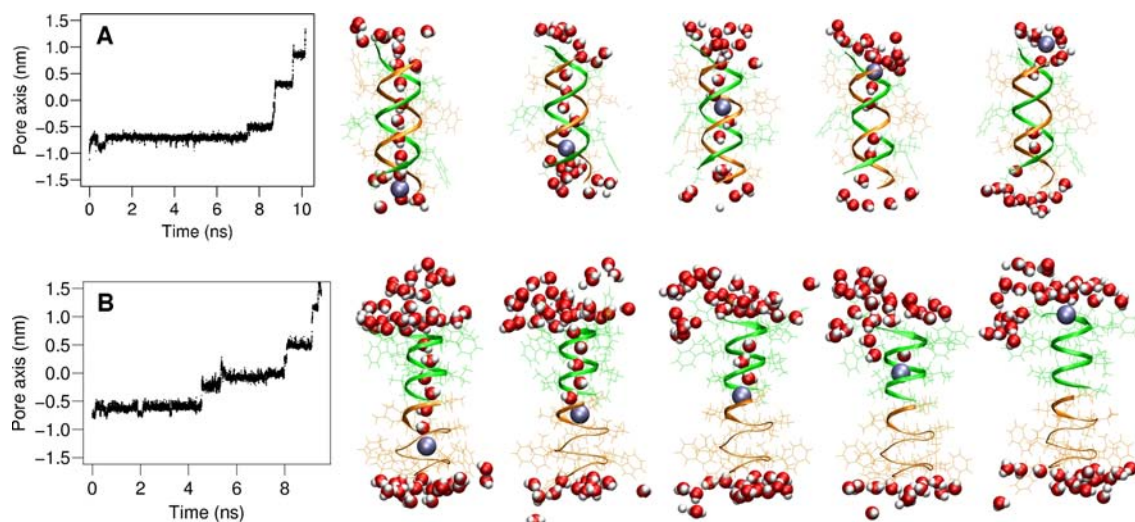


Figure 3.10: Snapshots of potassium cation passage through the DH gramicidin (A) and through the HD gramicidin (B). The projection of the cation position as a function of time on the gramicidin channel axis as well as representative snapshots during the passage are shown (potassium ion in blue, water molecules in red).

Flipping of the water file dipole moment from -15 D to $+15$ D during cation passage through HD gA has been reported applying umbrella sampling calculations [200]. The found dipole reversal during passage would hamper the entrance of a second ion [200]. This complication for multiple ion permeation is absent for the DH conformation of gA: the water file dipole orientation close to the channel entrances is enforced to point towards the membrane center (see Fig. 3.8). Small transmembrane potentials (unlike those applied in this study) will presumably not change this orientation. Thus an approaching cation will *always* find a correctly directed water file when approaching gramicidin in DH conformation.

3.4 Summary and conclusions

We studied the properties of a gramicidin/DMPC membrane subject to external electric fields of various strengths in comparison to the field-free case. The main results are: First, gramicidin A considerably suppresses membrane electropore formation. Close to gramicidin, the phospholipid bilayer is thinned due to a hydrophobic mismatch between the protein and the hydrophobic core of the bilayer. Distal to gramicidin (2–3 nm), the

bilayer thickness is increased, thereby decreasing the probability for closed water files across the membrane. The latter is the time-limiting step for electropore formation. The applied membrane potentials for electropore formation of approximately $\Delta\Phi_m = 2.5\text{--}3.0\text{ V}$ appear quite high. However, please note that the same membrane potential would be achieved by a charge difference on both sides of the membrane of four elementary charges, or only two calcium ions. A small charge imbalance across a lipid bilayer has recently been shown to be sufficient for electropore formation in a simulation study [190].

Second, our results demonstrate the structural stability of both gramicidin A conformations for large transmembrane potential differences. The spontaneous water passage through the channel is only weakly affected by external electric fields. Both gA conformations differ significantly in the dipole orientation and dynamics of the single-file water molecules: Complete flipping of the confined water molecules dipole moment was not observed on the 20 ns timescale for the HD conformation. In contrast, the dipole moment of the channel water molecules in the DH conformation fluctuates on the subnanosecond timescale with frequent dipole reversals in the central region, strongly influenced by the preferred bulk water dipole moment in the phospholipid headgroup region.

Third, spontaneous cation passage of pre-inserted cations was found for both conformations, albeit at a higher rate for the DH conformation. The frequent closure of one or both channel entrances by the ethanolamide groups at the C-termini likely hampers both water and thereby cation passage mainly through HD gA.

The currently favored biologically active conformation of the gA channel is the head-to-head helical dimer (see e.g. [197]). However, the conformational preference of gramicidin A is strongly dependent on the specific environmental conditions like the fatty acid chain length and even on the bilayer preparation (see [192] for a review). Thus no universal answer to the question of the biologically active conformation can be given to date. Despite enormous efforts, free energy calculations on ion permeation through gA in the HD conformation still yield a potassium conductance which is 4–5 orders of magnitude too small as compared to experiment (see [198] and references therein). Our results contain hints to a decreased free energy barrier for ion passage in DH compared to HD: the increased water permeation rate in DH as it was also found earlier [196], the frequent reversals of the water file dipole moment in DH, and the large open rate of the channel entrances in DH. Free energy calculations by e.g. applying the umbrella sampling tech-

nique could provide more insight into the properties of the double-helical conformation as an ion channel.

Acknowledgements

We thank Alexander Benedix for help with preparation of the simulation system, Beate Griepernau, Bert de Groot, Helmut Grubmüller, and Volker Knecht for valuable discussions, and BG for critical reading of the manuscript. Shirley W. I. Siu is supported by the Deutsche Forschungsgemeinschaft (Graduate School *Structure Formation and Transport in Complex Systems*, No. 1276/1). As a member of the Center for Bioinformatics, Rainer A. Böckmann is supported by the Deutsche Forschungsgemeinschaft Grant BIZ 4/1.

Low Free Energy Barrier for Ion Permeation Through Double-Helical Gramicidin

Shirley W. I. Siu and Rainer A. Böckmann. *J. Phys. Chem. B* 113 (2009), 3195-3202. ¹

Summary

The pentadecapeptide gramicidin forms a cation-specific ion channel in membrane environment. The two main conformations are the head-to-head helical dimer (HD) known as the channel conformation and the intertwined double helical form (DH) often referred to as nonchannel conformation. In this comparative study, the energetics of single potassium ion permeation by means of the potential of mean force (PMF) for both gramicidin conformations embedded in a DMPC bilayer has been addressed by molecular dynamics simulations. A significantly decreased free energy barrier by ≈ 25 kJ/mol for potassium ion passage through DH as compared to HD is reported. Favorable electrostatic side chain-cation interactions in HD are overcompensated by phospholipid-cation interactions in DH. The latter are coupled to an increased accessibility of the channel entrance in DH due to distributed tryptophans along the channel axis. This result underscores the importance of the lipid environment of this channel not only for the equilibrium between

¹Reproduced with permission. Copyright 2009 American Chemical Society.

the different conformations but also for their function as cation channels.

4.1 Introduction

Gramicidin A (gA) is the major component of the antibiotic gramicidin from the soil bacteria *Bacillus brevis*. Each monomer is made up of 15 alternating L- and D-amino acids capped at the two ends by a formyl group and an ethanolamine group. When dimerized, gA functions as a cation-selective transmembrane channel. In contrast to most structurally resolved ion channels, the unique sequence of the gA peptide is able to adopt a wide range of conformations based on various environmental factors, such as solvent history (incorporating solvents used to cosolubilize gramicidin and phospholipids), peptide concentration, types of lipids, temperature, and binding of cations [231–236]. Mainly, two folding motifs of gramicidin were reported in experimental structural studies, namely the single-stranded head-to-head helical dimer (HD) [237, 238] and the double-stranded helical dimer (DH) (Fig. 4.1) [209, 236], which can be further categorized according to their handedness. In the past three decades, extensive experimental measurements were performed to discriminate the biological active conformation in the membrane from the non-active one, and the head-to-head dimer has been considered as the consensus model (for reviews see [66, 192, 239]).

An important argument for the existence of head-to-head dimerization in membranes was given by Urry *et al.* [241] who showed that the dimers with covalently linked N-termini displayed conductivity. Bamberg *et al.* and Apell *et al.* [242, 243] showed that modification at the N-terminus of the peptide but not at the C-terminus affected the single channel conductivity. Shift reagent NMR experiments indicated that both N-termini of the dimer were buried deeply within the bilayer while the C-termini were located near the surface of the membrane [244]. Furthermore, the circular dichroism spectrum (CD) of the channel embedded in a bilayer [245] was found to be qualitatively different from the spectrum obtained from channels in various organic solvents, in which the double helical dimer conformation is predominant. Thereafter, CD spectra were conventionally used in laboratories to validate the peptide conformation in the samples.

While the head-to-head dimer was believed to be the thermodynamically more stable form in membrane environment, some experiments demonstrated that the pep-

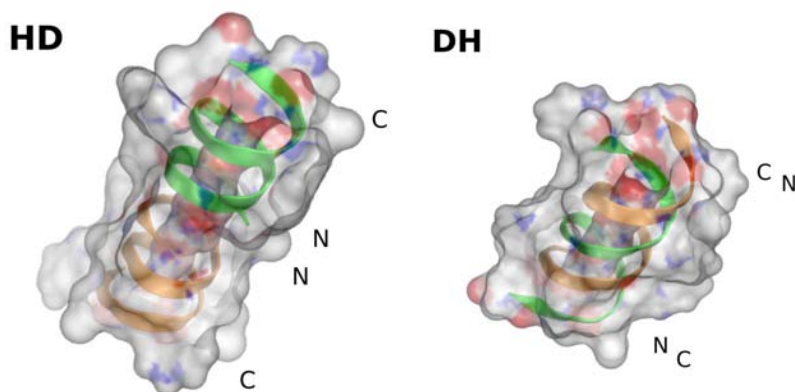


Figure 4.1: The two major conformations of gramicidin drawn in its solvent accessible surface (water radius 1.4 Å: the head-to-head (HD) and double-helical dimer (DH). The figure was prepared using Pymol [240].

tide might as well adopt a conformation different from the HD structure by virtue of a different incorporation protocol. Using CD, Killian [231] observed that gramicidin prepared in ethanol preserved the antiparallel double-helical dimer conformation in the membrane. At room temperature, conversion to the HD form was very slow and thus the membrane was regarded as an environment of minimal conversion. Applying the High-Performance Liquid Chromatography, Bano [233] demonstrated that the double-stranded dimer coexists with the single-stranded form in the membrane in certain ratio. The finding of a right-handed double-stranded helical dimer conformation that showed agreement with the measured ^{15}N -NMR pattern [209] again arose disputes [206–208] on the biologically active conformation of gramicidin in a lipid environment.

Despite the ongoing controversies, due to its small size and the well-defined channel pore gramicidin has been a popular model system for studying the properties of an ion channel and the mechanism of ion conduction. Previous computational studies focused on the energetics of ion and proton permeation through the HD dimer. They cover continuum electrostatics calculations (see for example [151, 246–248]), semi-microscopic models [249–251], as well as microscopic models [224, 252–259]. The latter are particularly interesting for the level of detail which can be obtained. Potentials of mean force (PMF) for ion permeation through the HD channel derived from classical atomic-detail molecular dynamics showed an unexpectedly high central energy barrier and relatively weak binding sites at the channel entrances. Improved PMF profiles in reasonable agree-

ment to observables could be obtained by correcting for system boundary and polarization effects [249, 254]. Nevertheless, resulting barrier for potassium ion through HD is still in the range of 25 kJ/mol [254], at least a factor of two too large compared to the experimentally derived barrier [151].

On the other hand, the DH conformation hardly studied in simulations has been shown to translocate a water column at an increased rate as compared to HD [196, 260]. The double-stranded conformation allows for an orientation of channel water dipoles favorable to a cation entry on both sides. Spontaneous water dipole restoration observed after ion passage suggested a facilitation of multiple ion passages in the DH as compared to HD [260].

Here, in a comparative study we focus on the ion conduction properties of both DH and HD conformations using a non-polarizable force field. The potential of mean force for one-ion permeation through the channel is computed. Our results reveal a decreased free energy barrier and an increased structural flexibility for DH as compared to HD. While the PMF profiles might be sensitive to the force field parameters, tests using a modified ion-protein interaction retained a decreased PMF barrier for the DH channel.

4.2 Methods

4.2.1 System setup

The gramicidin embedded membrane system was prepared by the same procedure as described in our previous work [260]. It consists of a gramicidin, 124 dimyristoylphosphatidylcholine (DMPC) lipids and 6,142 water molecules. The initial structures of gramicidin were taken from the PDB database: 1MAG [210] for the head-to-head helical dimer (HD) and 1AV2 [209] for the intertwined double helix (DH). The system was equilibrated for 40 ns. The average area per lipid was approximately 60 \AA^2 , which is in agreement with experiment [261]. Bulk water molecules were replaced by K^+ and Cl^- ions to achieve an ionic concentration of 200 mM. The system was further equilibrated to prepare for the free energy simulations.

4.2.2 Potential of mean force calculations

The potential of mean force (PMF) [150] of ion permeation is the Helmholtz free energy W defined from the average distribution function of the sampled ion along the chosen permeation path ξ , in reference to the bulk value [133]:

$$W(\xi) = W(\xi_0) - k_B T \ln \left[\frac{\langle \rho(\xi) \rangle}{\langle \rho(\xi_0) \rangle} \right] \quad (4.1)$$

For the PMF of ion permeation, the ion's positions along the gramicidin channel have to be sampled. Since ion permeation is a process with an activation barrier well above $1.5 k_B T$ [151], classical MD simulations would yield an insufficient sampling. One way to circumvent this is to employ the umbrella sampling technique; by introducing a biased potential, the ion movement is restrained to positions along the reaction pathway. The PMF is then calculated by unbiasing and combining the ion density distributions of the window simulations using the weighted histogram analysis method (WHAM) (see [153] and [133] for a review). The coordinate parallel to the bilayer normal was chosen as the reaction coordinate, and the protein's center of mass as the origin. The entire pathway covering the range of $[-30, 30]$ Å was divided into 0.5 Å intervals summing up to a total of 121 windows.

To ensure similar starting conditions for the window simulations, we selected a trajectory from the classical simulations such that both the channel tilting angle and the channel length were equilibrated. For HD, convergence was reached in 20 ns (protein mean rms 0.15 nm, tilt angle $15.8 \pm 2.5^\circ$, channel length 2.0 ± 0.02 nm) and for DH in 24 ns (protein mean rms 0.19 nm, tilt angle $5.0 \pm 2.2^\circ$, channel length 1.6 ± 0.02 nm). The increased tilting of HD as compared to DH can be attributed to its increased channel length. The tilt enables polar interactions of the channel terminal tryptophans with the lipid hydrophilic headgroup region.

Starting structures for the window sampling were selected from the last 5 ns of the equilibration based on the following criteria: (a) the channel must be filled with water molecules and (b) a water molecule is found close to the center of the window (typically within 0.1 Å distance). The water molecule closest to the center of the respective window was exchanged with a potassium ion in the bulk. Throughout the unbiased simulations, both the HD and DH channel were partially closed by a nearby lipid. Similar headgroup

protrusions were reported previously in other MD studies of the HD conformation of gramicidin using different types of lipids [230, 258]. In order to obtain starting structures for windows in the channel entrance region, we performed additional classical simulations exchanging the water molecule in the single-file close to the blocked entrance with a potassium ion. The inserted ion escaped from the channel within about 2 ns simulation time for the HD and 7 ns for the DH. Window selection for the channel entrance regions was based on these simulations applying the same selection criteria as above.

Molecular dynamics simulations were performed using the GROMACS package [161, 212] applying a combination of the GROMOS96 53a6 force field for gramicidin [124] and the Berger [128] lipid force field. The vdW parameters for K^+ and Cl^- ions were taken from Straatsma [262], while parameters for the D-amino acids were obtained by reflecting the backbone dihedral angle of the respective L-amino acid, and charges for the formyl and ethanolamide groups were assigned according to the parameters from the peptide backbone and the serine residue of the GROMOS 53a6 force field.

In the window simulations, a harmonic potential with a force constant of $4,000 \text{ kJ mol}^{-1} \text{ nm}^{-2}$ was employed to restrain the sampled ion around the center of the window. Systems were simulated applying periodic boundary conditions with the temperature coupled to 310 K and pressure coupled semi-isotropically to 1 bar. All H-bonds were constrained using LINCS [215] or SETTLE algorithm [216], allowing for an integration step size of 2 fs. Pairlists were generated every 10 integration steps. The cutoff for LJ interactions and for short-range electrostatics was set to 1.0 nm, while the long range electrostatics was treated with the particle-mesh Ewald method (PME) [147]. Trajectories were written every picosecond and umbrella sampling data (ion position with respect to the window center) were collected at every integration step. All window simulations were equilibrated for 500 ps; 2.5 ns simulations were followed for data production. In the WHAM, a sampling bin size of 0.05 \AA and tolerance of 0.001 kT were used to check the convergence. Free energies at a distance of 30 \AA from the channel center were chosen as the bulk reference. The effect of channel tilting on the free energy profile was estimated by additional window simulations removing the rotational motion of the protein around its center of mass at every integration step. Symmetrized PMF profiles were obtained by averaging the density of states between both sides of the profile.

Note that free energy calculations based on MD simulations are subject to arti-

facts from the use of PME, periodic boundary conditions, and finite system sizes [254, 263]. The error introduced by Ewald summation is inversely proportional to the system size [264]. Concerning lateral periodicity of the membrane-gramicidin system, Allen *et al.* [254] derived an error of ≈ 0.1 kJ/mol for the system size used here.

4.3 Results

4.3.1 Potential of mean force

The PMF for potassium permeation is obtained by averaging over the sampled conformational states for every ion position along the membrane normal. PMF calculations using the umbrella sampling technique require a set of window simulations covering the entire reaction pathway. Depending on the equilibration time of the investigated system and the level of convergence required, each window simulation may take from a few hundred picoseconds [256] to some nanoseconds [254] in order to obtain sufficient statistics.

In this study, each window simulation was run for 3 ns (in total 363 ns of simulation time for each dimer conformation). To test for convergence, the PMF profiles were calculated for different time window length. As shown in Fig. 4.2 (left panel), the root-mean-square deviation (rmsd) between the profiles obtained for the first 500 ps and for the time window between 0.5 and 1.0 ns were 15 (HD) and 17 (DH) kJ/mol. This indicates a rather quick relaxation from the starting configuration in both cases. The first 500 ps of the trajectories were discarded for the PMF calculations to avoid artefacts from equilibration. Despite the structural symmetry of gramicidin, PMF profiles are typically asymmetric due to slow fluctuations not sufficiently sampled in nanosecond simulation, that is, membrane undulations, fluctuations in the lipid packing, or channel tilting. Errors from insufficient sampling are accumulated and may even not be eliminated by extensively long simulation time (see [252]).

The rmsd between the left and the right side of the potential around the protein center (at $z = 0$) after different simulation time lengths (500 ps, 1 ns, 1.5 ns and so on) were 26, 23, 18, 14, 14 and 15 kJ/mol for HD, and 26, 13, 8, 9, 9 and 8 kJ/mol for DH. This trend of decreasing rmsds implies that the asymmetry is improved at drastically increased simulation times. Typically, the obtained profiles are symmetrized (Fig. 4.2, right panel).

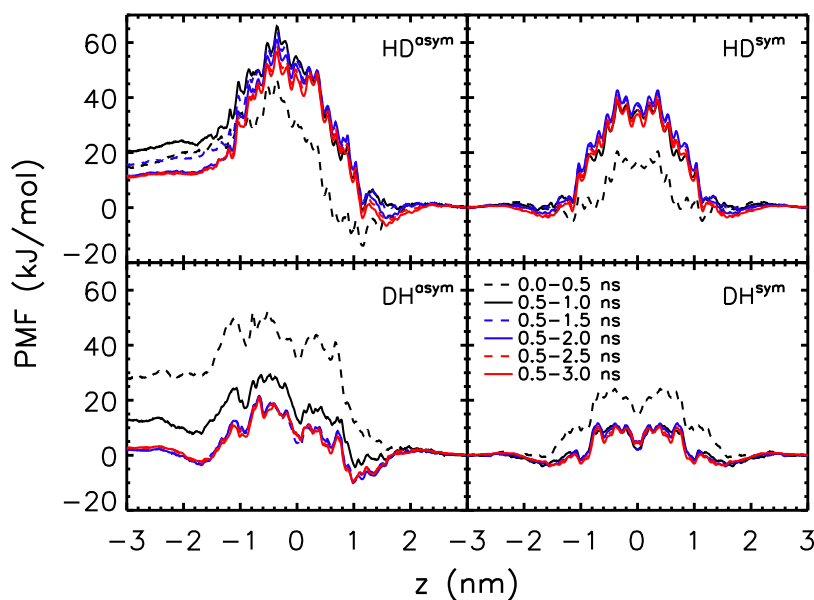


Figure 4.2: Time evolution of the asymmetric and symmetric HD (upper panel) and DH (lower panel) PMF profiles. The first 500 ps of the simulations were discarded for subsequent analyses. The 1D-PMF curves are only well defined within the channel constriction zone (approximately $|z| \leq 1.6$ nm).

The symmetrized PMF profiles of the two gramicidin conformations show a remarkable difference in stabilizing a K^+ ion along the gramicidin channel. As shown in Fig. 4.3 (solid lines), the HD profile displays a large central barrier of about ≈ 40 kJ/mol. A wide shallow well is observed at the interface of the channel and the lipid headgroup region. The ion entering the channel experiences a stepwise increase in free energy. Results obtained in this study for the HD conformation are in good agreement with previous free energy calculations for the barrier height. An internal binding site was reported applying the CHARMM and AMBER force fields [254, 256, 265] (see Table 4.1); however, for both GROMOS87 [254] and for the more recent GROMOS96 (this study), this internal binding site cannot be identified.

In contrast to HD, the DH profile has a much less rugged energy profile with a decreased central barrier of only 14 kJ/mol, at least a factor of three lower than for HD. Binding sites both at the channel entrances as well as in the lipid interfacial region are clearly seen. Experimentally, it was observed that gramicidin contains two symmetrically

Table 4.1: Comparison of our PMF results to former MD studies (energy values are given in kJ mol⁻¹).

	forcefield	barrier	well depth	total barrier height
this study (HD)	GROMOS96	39.1	–	39.1
this study (DH)	GROMOS96	10.7	–3.6 at 1.6 nm	13.7
			–3.0 at 1.0 nm	
Allen (HD) [§]	CHARMM27	40	–6 at 1.13 nm	46
Bastug (HD) [†]	CHARMM27	38	–12 at 1.10 nm	50
Bastug (HD) [‡]	CHARMM27	33	–17 at 0.97 nm	50
Allen (HD) [§]	GROMOS87	63	–	63

The barrier is measured at the point of largest energy in the channel, typically around the central region, the total barrier height is measured with respect to the internal well depth. Values[§] were taken from the uncorrected PMF in *Figures 4 and 14* of ref [254]. Values[†] were taken from ref [265] and [‡] from ref [256].

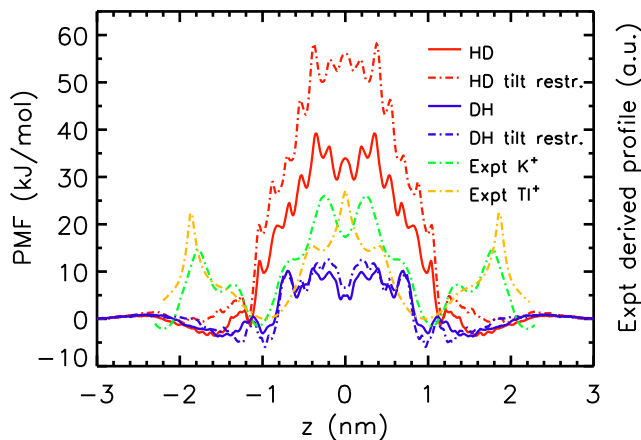


Figure 4.3: Comparison of the PMF profiles for K⁺ permeation through the gramicidin channel in HD and DH conformation (symmetrized). The 1D-PMF curves are only well defined within the channel constriction zone (approximately $|z| \leq 1.6$ nm). The potassium (K⁺) and thallium (Tl⁺) profiles of Olah *et al.* [266] were estimated from the experimental electron density data by $dG = -RT \ln(\frac{\rho_{diff}^{max}}{\rho_{diff}})$, where ρ_{diff} is $\rho(\text{ion sample}) - \rho(\text{salt-free sample})$. Hence, the profiles are plotted in arbitrary units. Additional peaks outside of the channel ($|z| = 2$ nm) are probably due to small lamellar spacings used in the experiments.

related binding sites at both ends of the channel [266–268]. However, the exact location and width of the binding sites are slightly different for different cations (e.g. for K⁺ and Tl⁺, see Fig. 4.3). In our study, the position of the binding site at the channel entrances observed for DH in the simulations are in very good agreement with the binding sites

derived from difference electron density profiles between gramicidin in a KCL solution and a salt-free solution [266] (binding sites 10.1 Å from the channel center). Also the central dip in the experimental profile compares favorably with the profile for the DH conformation.

Because the sampled ion is unbound outside the channel, the PMF in the channel entrance region may be dependent on the extent of sampling [254]. For the HD conformation, Bastug *et al.* [269] showed that the PMF with a restrained potassium differs by ≈ 1 kT from the unrestrained one. Similarly, for the case of DH, we tested the effect of a flat-bottom lateral restraint (confining the ion radial displacement to within ≈ 0.8 nm to the center of the channel axis) in the channel entrance region on the PMF profile (data not shown). The resulting PMF profile was similar to the unrestrained profile, the measured total barrier height was increased by less than 1 kJ/mol.

In both equilibration and window simulations, the gramicidin channels are tilted at varying degrees with respect to the membrane normal. HD showed a large average tilt angle of 15° while DH is fairly perpendicular to the membrane plane with a tilt angle of $\approx 5^\circ$. The HD has a channel length of 2.0 nm (measured as the distance between centers of mass of the backbone C α -atoms forming the last helical turn at the channel ends) as compared to only 1.6 nm for DH. Evidences of transmembrane helix tilting were reported in numerous NMR and Infrared spectroscopic studies using gramicidin [270–273] and WALP peptides [274, 275] (Leu-Ala core of α -helix flanked by pairs of Trp residues at N- and C- terminals). However, the cause of helix tilting has so far not been fully understood. It was observed as a consequence of membrane hydrophobic mismatch (e.g., membrane thickness, see ref [276] for a review) or the preferential disposition of aromatic residues such as tryptophans in the membrane interface [274]. The magnitude of tilting was found to be affected by the type of lipid headgroup [273], length of the bilayer hydrophobic core [275], ordering of the lipid tails [270, 273], peptide length [277], and packing of aromatic residues [278]. Channel tilting of gramicidin was also reported in previous computational studies [254, 258], but the effect of this tilting on the free energy profiles of ion permeation was not quantified. To answer this question, we performed window simulations with additional restraints on the protein rotational motion, such that the protein helical axis is oriented parallel to the membrane normal.

As to be expected, the PMF profiles obtained from the restrained simulations are

more symmetric as compared to the nonrestrained ones. After 3 ns, the rmsd between the left and the right side of the profile decreased to 4 kJ/mol for HD and 3 kJ/mol for DH. As shown in Fig. 4.3 (red and blue dashed-dotted lines), the free energy barrier of the restrained HD is increased by 18 kJ/mol as compared to the flexible HD, while the external binding site is even more shallow. There is no significant change in the ion permeation barrier for the restrained DH, but both internal and external binding sites are slightly shifted inward (to the protein) with a small increase in well depth by 3 and 1 kJ/mol, respectively.

4.3.2 Pore radius of gramicidin

Ion translocation through the narrow gramicidin channel occurs in a single-file mode. To some extent, the initial increase of the PMF is due to partial dehydration of the potassium ion upon channel entrance [197]. Inside the narrow channel, the cation is coordinated by two water molecules [193]. The loss of desolvation is partially compensated by attractive electrostatic interactions to the backbone carbonyls [193, 199, 267, 268] which are deflected toward the passing cation. Thus these carbonyls play an important role in coordination of the ion translocation process.

The structural change of the channel in response to the presence of a K^+ ion is reflected by changes in the pore radius. As shown in Fig. 4.4, the DH conformation has a pore with a uniform radius of $\approx 1.7 \text{ \AA}$ in the ion-free state. In contrast, the pore is more narrow for the HD at the channel entrances, increasing toward the channel center. In the window simulations, both DH and HD adapt to the bound ion by reorientation of the carbonyls towards the ion, thus resulting in smaller pore radii. Drastic changes close to the channel openings were observed in DH which amounts to a mean reduction of about 50% in the pore radius, reflecting the high flexibility of the double-helical conformation to the conducting ion. As expected from its more narrow pore in the ion-free simulation, the HD is contracted by less than 20% along the channel while maintaining its overall pore shape.

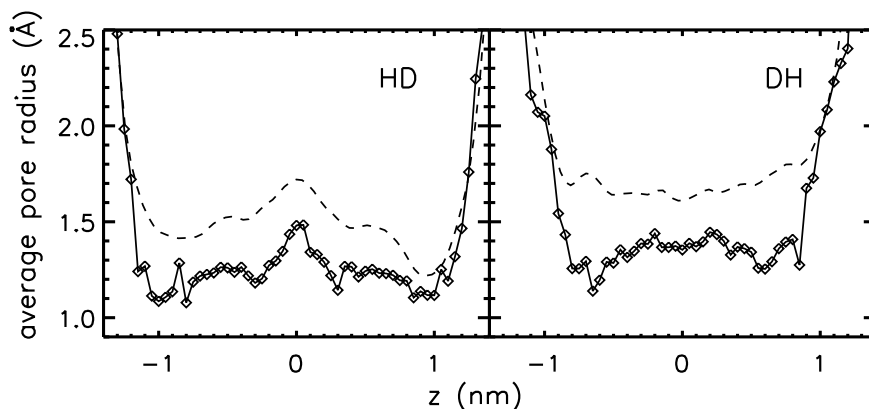


Figure 4.4: Radius of the channel along the helical axis at the restrained cation positions (*solid* line). The calculation was done by the HOLE program [279] using a sampling plane distance of 0.25 Å, and averaged over snapshots from every 10 ps. The channel radius for the ion-free state is shown as a *dashed* line.

4.3.3 Energy decomposition

The enthalpic contributions to the PMF can be estimated by analysis of the non-bonded interaction energies of the ion with the protein and the environment. For both HD and DH conformations, the largest contribution to the stabilization (see Fig. 4.5A) of the ion in the pore interior as well as in the binding sites is due to the protein backbone, in agreement with the finding that ion passage is coordinated by the backbone carbonyls. The enhanced backbone contribution for the DH in the channel core is due to the decreased channel length of DH (1.6 nm) as compared to HD (2.0 nm), i.e. the carbonyls have a larger density in the DH core. This attractive contribution is overcompensated by the large positive energies between the potassium ion and the membrane (including the electrolyte) resulting in an energetic barrier for ion permeation. A similar picture was previously reported by Allen et al. [200] for the HD by virtue of the mean force decomposition.

Comparison of the energies of the sampled ion in HD with those in DH (see Fig. 4.5B) reveals more favorable potassium interactions to the phospholipid and the bulk solution for the intertwined double-helical gramicidin. In total, the potassium ion is stabilized by ≈ 90 kJ/mol in DH as compared to HD.

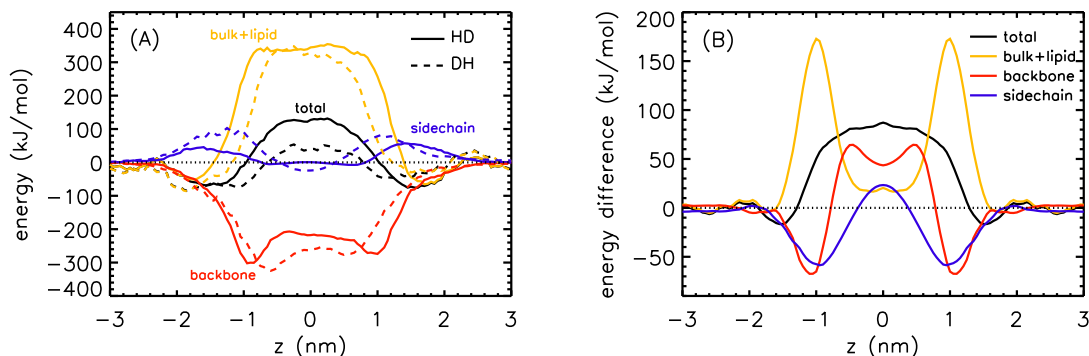


Figure 4.5: (A) Interaction energies E of the sampled ion with different components of the environment calculated for each umbrella window. E is calculated as the sum of Coulombic and Lennard-Jones interaction energies. The reference energy (leftmost bulk value) is set to zero. Note that the bulk component consists of both water molecules and ions. (B) The difference interaction energy $\Delta E = E_{HD} - E_{DH}$ (symmetrized). Positive values in the plot indicate favorable interactions in DH as compared to HD.

Interestingly, the protein-potassium interactions at the channel entrances are more favorable in HD as compared to DH (≈ 100 kJ/mol). However, this attractive contribution is outbalanced by a considerably more strong repulsive interaction of the cation to the lipids and the bulk solution in HD (≈ 180 kJ/mol). These results reveal the determining role of the protein-surrounding lipids (and their hydration shells) in stabilizing the cation at the pore entrance. To investigate this in more detail, we calculated the cumulative radial distribution functions (cdf) of the lipid choline and phosphate groups to the potassium ion when the cation is restrained at distances of ± 0.8 , ± 1.0 , and ± 1.2 nm to the protein center of mass (see Fig. 4.6). It is evident that the phosphate groups (net charge -1) of DH (dashed lines) can reach closer to the pore cation than those of HD. Obviously, the arrangement of the surrounding lipids to the gramicidin is affected by its conformation, as illustrated in Fig. 4.7. In the head-to-head dimer conformation (HD) all tryptophans are located at the channel entrances while they are distributed along the helical axis for the intertwined DH. As seen in the snapshot of HD, the tryptophan cluster at the channel entrances sterically hinders interaction of lipid headgroups with the ion at the channel entrance. In contrast, the DH conformation allows for tighter interaction of the bound ion to surrounding lipids.

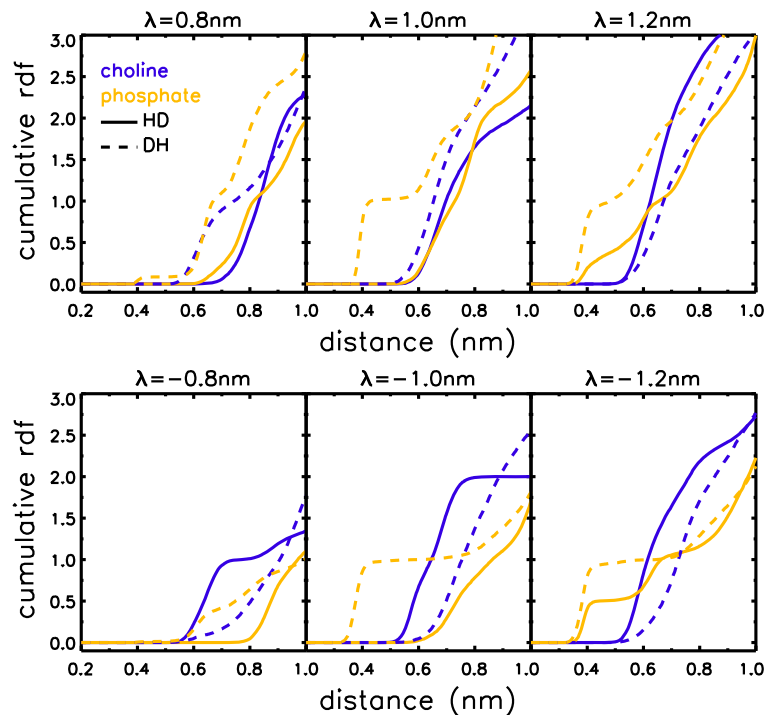


Figure 4.6: Cumulative radial distribution functions (cdf) of the DMPC choline (*blue*) and phosphate group (*orange*) to the sampled potassium ion in umbrella windows (λ indicates the center of the respective window in z dimension). Results for HD are shown as *solid* lines, those for DH as *dashed* lines.

4.3.4 PMF with the modified potassium-carbonyl oxygen parameters

The GROMOS biomolecular force field used here for the gramicidin was parametrized to reproduce the free enthalpies of solvation in polar and apolar solvents of representative compounds derived from amino acids [124]. In contrast, protein-ion interactions that were not included in the parametrization procedure are typically approximated by conventional combination rules. For these, the Lennard-Jones (LJ) parameters for ions derived in a separate study by Straatsma *et al.* [262] were chosen. These were fitted to reproduce the free energy of ionic hydration in simple point charge (SPC) water. Therefore, the actual interaction between the ion and the protein inferred in this way could possibly be under- or overestimated.

This deficiency of nonpolarizable biomolecular force fields was reported previously in computational studies using the popular CHARMM and AMBER forcefields, and also

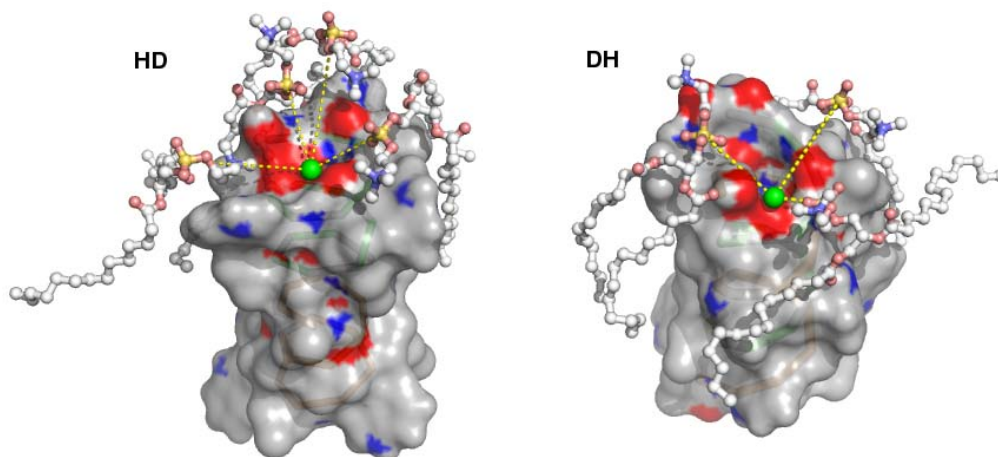


Figure 4.7: Snapshots of simulations with a potassium ion (colored green) restrained to the channel entrances. Spatially closed lipids are shown in ball-and-stick representation. Yellow dashed lines indicate the interactions between the ions and the lipid phosphorus atoms (colored orange).

for the earlier version of GROMOS87 [254, 280]. Indeed, the microscopic interaction energy between a potassium ion and the model protein NMA in these force fields is larger by 2 (CHARMM) to 37 kJ/mol (GROMOS87) [254] as compared to *ab initio* studies. For the GROMOS96 force field version 53a6 the deviation to *ab initio* data is decreased to 26 kJ/mol (data not shown) as a result of increased partial charges of the backbone atoms as compared to GROMOS87.

As demonstrated by Allen *et al.* and Roux *et al.* [254, 280] using the CHARMM force field, a more accurate representation of the protein-ion interactions based on the current potential functions could be obtained by reducing the potassium σ -value of the LJ potential in the interaction to carbonyl oxygens. Here, we tested the effect of similar reductions in the σ value in the GROMOS96 53a6 force field on the PMF. Two modified potentials were tested by performing window umbrella sampling simulations with $\sigma^{0.95}$ and $\sigma^{0.90}$ (multiplying σ by the indexed factor). As shown in Fig. 4.8, the free energy profiles are sensitive to the change in the potassium LJ parameters, but the influence in the profile was more drastic in HD as compared to DH: The overall profile was shifted downward and broad internal binding sites at the channel entrances emerged. Interestingly, while the total barrier height (the central barrier plus the well depth) for $\sigma^{0.95}$ was decreased (from 39.1 kJ/mol with the unmodified σ) to 35.5 kJ/mol, further reduction of

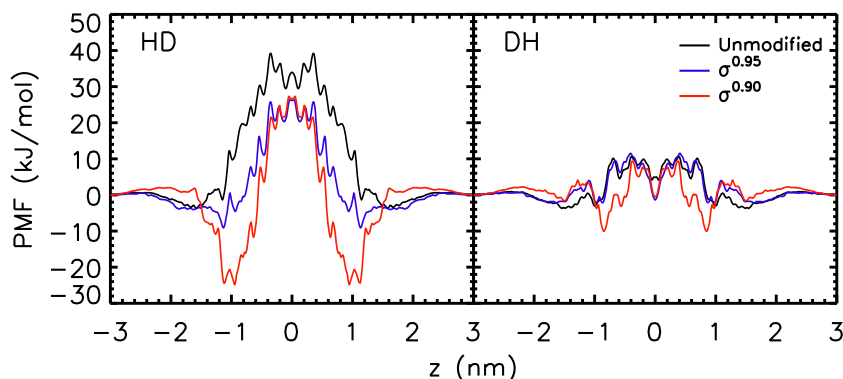


Figure 4.8: Comparing the PMF profiles obtained with calibrated K^+ -O LJ interactions by adjusting the atomic separation distance σ . The 1D-PMF curves are only well defined within the channel constriction zone (approximately $|z| \leq 1.6$ nm).

the σ -value resulted in an increase in the total barrier height (51.9 kJ/mol for $\sigma^{0.90}$) due to an overenhanced stabilization of the binding well. In DH, a scaling of σ by 0.95 had only minor influence on the free energy profile; for $\sigma^{0.90}$, the well depths became more pronounced, similar to the HD case. A conformation-dependent influence of the ion interaction parameter on the PMF profile was expected due to the different distributions of the backbone carbonyls in the channels. The larger effect of the shifted LJ interaction on the HD conformation as compared to DH may be explained by the smaller pore radius of HD and thereby increased sensitivity on the potassium-carbonyl oxygen interaction. For all investigated cases, the total barrier in the HD channel exceeded the DH barrier by 20–30 kJ/mol, underlining the increased stability of potassium in the DH channel as compared to HD.

4.4 Discussion and summary

In this study, we have analyzed the PMF for single potassium ion permeation both through the head-to-head helical dimer conformation and through the double-helical dimer conformation of gramicidin. The shape of the profile and the barrier height of 39.1 kJ/mol obtained for HD using the GROMOS96 53a6 force field is in agreement with earlier studies applying the GROMOS87 and the CHARMM force fields [254, 256, 265]. However, DH gramicidin embedded in a DMPC lipid bilayer displayed a significantly decreased free energy barrier for potassium ion permeation as compared to HD (13.7 kJ/mol).

Assuming that DH forms a stable channel our result seems to contradict experiments which suggested the HD conformation as the conducting conformation of gramicidin (*channel form*) while DH was termed the *nonchannel* conformation [241, 242, 244].

Conductance experiments by Bamberg *et al.* [242] and Apell *et al.* [243] adding bulky negatively charged pyromellityl groups to the N- or C-termini of the peptide observed channel activity only for gramicidin modified at the C-terminus. N-terminal-modified gramicidin, impeding the formation of HD dimers, was suggested to act as a detergent rather than an ion channel. The authors concluded that the gramicidin *channel* is formed by head-to-head association of the monomers rather than by the DH conformation. However, also the latter conformation was shown to have channel-like properties: For desformylated gramicidin probably predominantly existing in the double-stranded conformation [196, 281] a potassium conductivity of 7 pS was reported (KCL concentration 0.1 M) [281], the same order of magnitude as compared to HD with conductivities of 9–26 pS (KCL concentrations between 0.1 and 1 M [282–284]). It is important to note, however, that the desformylation introduces a positive charge at the N-terminus which might both decrease the potassium concentration at the channel entrances and modulate the interaction of the gramicidin to the lipid environment (see below). This is in line with a study on cation transport in mitochondria by gramicidin and by desformylated gramicidin: At high ion concentrations, desformylated gramicidin was reported to be nearly as effective as gramicidin in collapsing the mitochondrial membrane potential [285]. The ions were suggested to stabilize the channel structure. It should be noted, however, that the charges introduced by desformylation will be screened more effectively at large ion concentrations. Therefore, desformylated gramicidin is probably showing an increased functional similarity to gramicidin in DH conformation at large salt concentrations. The experimental results on desformylated gramicidin together with our finding of a decreased barrier for potassium permeation through DH gramicidin as compared to HD hint at a biological relevance of gA in DH conformation also.

The molecular basis for the decreased free energy barrier for ion permeation through the nonchannel conformation of gramicidin is obtained from a decomposition of the enthalpic contributions to potassium ion stabilization in the gramicidin channel. Neglect of the influence of the lipid and bulk water environment results in a stabilization of the potassium ion in the channel gramicidin (HD) as compared to the nonchannel gramicidin

(DH). Thus our results suggest that changes in the lipid environment (and the associated coupled hydration shells) not only change the equilibrium between different gramicidin conformations like those observed experimentally [204] but may have a profound influence on the conductance properties of the channel also without changing the specific channel conformation. Lipids with a modified lipid headgroup are likely to decrease the favorable lipid-ion interaction observed here for the DMPC – DH system. Thus whether the gramicidin in a specific conformation acts as a channel or not is expected to crucially depend on the chosen lipid environment. For that reason, we expect also modifications at the channel entrances to affect channel conductance, for example, by modulating the interaction to the environment. In addition, the channel conductance will also be affected by the tilting angle of the gramicidin which might, for example, probably be affected by the thickness of the hydrophobic core of the chosen membrane environment; for HD a significantly increased free energy barrier was observed for a straightened channel.

Indole-containing tryptophans along the gramicidin channel have a 2-fold effect on the permeation characteristics of the channel. First, by lipid headgroup interactions they are (co-) responsible for anchoring of the peptide in the membrane and thereby also determine the conformation-dependent arrangement of boundary lipids around the channel (microenvironment). Second, tryptophans assist ion permeation through the channel by favorable electrostatic interactions to the ion, strongly dependent on their localization along the peptide axis and their orientation. The latter was also expected from experiments revealing a reduced conductance of tryptophan-replaced HD channels [117, 118].

We note that the combination of the Berger force field for the phospholipids and the GROMOS96 force field for the protein may overestimate the protein-lipid interaction [129]. The here reported difference in the environment of the gramicidin channel entrances is, however, due to sterical reasons and should thus not severely be influenced by this shortcoming. Although the barrier height for HD applying the recently developed GROMOS96 53a6 force field is comparable to results reported for the CHARMM27 force field, the inner binding site for the HD conformation could not be reproduced. Probable reasons for this deficiency are the smaller carbonyl dipole strength used in GROMOS96 as compared to CHARMM27 and the nonideal potassium Lennard-Jones parameters. The strong dependency of the PMF (for HD) on the potassium ion-carbonyl oxygen interaction (see also Allen *et al.* [254], a 5% change in the force field parameter decreased the central barrier for HD by more than 10 kJ/mol) underlines the need for consistent force

fields in the study of membrane-embedded proteins (see also Siu *et al.* [132]). Current nonpolarizable force fields only implicitly take polarizability to a different degree into account, the optimal approach to simulate interfaces (protein, membrane, and bulk) in which induced dipole effect has been considered especially important is to use polarizable force fields [139]. Concerning gramicidin, inclusion of membrane polarizability has already been shown to improve the PMF profiles [200, 249, 254].

Acknowledgements

We thank Peter Pohl and Bert de Groot for stimulating discussions, and Peter Pohl for critical reading of the manuscript. The WHAM program was kindly provided by B. de Groot from MPI for Biophysical Chemistry in Göttingen. Financial support by the Deutsche Forschungsgemeinschaft (Graduate School *Structure Formation and Transport in Complex Systems* No. 1276/1) is acknowledged. As members of the Center for Bioinformatics, the authors are supported by the Deutsche Forschungsgemeinschaft BIZ 4/1.

Chapter 5

Biomolecular Simulations of Membranes: Physical Properties from Different Force Fields

Shirley W. I. Siu, Robert Vacha, Pavel Jungwirth, Rainer A. Böckmann.
J. Chem. Phys. 128 (2008), 125103. ¹

Summary

Phospholipid force fields are of ample importance for the simulation of artificial bilayers, membranes, and also for the simulation of integral membrane proteins. Here, we compare the two most applied atomic force fields for phospholipids, the all-atom CHARMM27 and the united-atom Berger force field, with a newly developed all-atom generalized AMBER force field (GAFF) for dioleoylphosphatidylcholine molecules. Only the latter displays the experimentally observed difference in the order of the C2 atom between the two acyl chains. The interfacial water dynamics is smoothly increased between the lipid carbonyl region and the bulk water phase for all force fields; however, the water order and with it the electrostatic potential across the bilayer showed distinct differences between the force fields. Both Berger and GAFF underestimate the lipid self-diffusion. GAFF offers a consistent force field for the atomic scale simulation of biomembranes.

¹Reprinted with permission. Copyright 2008, American Institute of Physics.

5.1 Introduction

Membranes are an indispensable constituent of biological cells. Apart from their apparent role in compartmentalization, they provide a unique hydrophilic and hydrophobic platform for the adsorption or anchoring of proteins to the interface, or for transmembrane proteins interacting mainly with the hydrophobic core. Lipid bilayers provide a highly modulative environment interacting, presumably affecting and possibly also keeping control of the function of, e.g., membrane ion channels and pores. The lipid-protein interaction is exerted both by hydrophobic interactions between the lipid acyl chains and the protein surface and by polar interactions at the lipid-water interface. Changes in the interaction profile may be attained by variations in the (local) membrane composition or that of the surrounding solvent or by changes in the temperature or pressure. Thereby, also the characteristic lateral pressure profile across the membrane is modified which may induce a shift of conformational equilibria between different states of membrane proteins, e.g., between the open and closed states of membrane channels [286, 287]. Molecules strongly interacting with membranes are, e.g., cholesterol [288, 289], anesthetics [290, 291], and monovalent [229, 292] and divalent cations [293, 294]. The latter bind tightly to the carbonyl oxygens of phospholipids and thereby increase the lipid packing density as well as modify the lipid headgroup orientation [229, 294]. Only recently, the importance of membrane thermodynamics for the understanding of propagating nerve pulses [295] or of the macroscopic effect of general anesthetic action [296] has been stressed.

Molecular dynamics (MD) simulation has been proven to be a powerful tool for the study of structural and dynamical properties of lipid membranes in atomic detail [19, 297, 298]. In recent years with the dramatic increase in computing power, membrane simulation has reached an unprecedented time scale, allowing the study of processes such as membrane assembly, fusion, domain formation, and protein/peptide/DNA interactions to be simulated while attaining statistical significance. In MD simulations, the intra- and intermolecular interactions of the lipids (also with the environment) are represented by specific potential functions (known as force fields). Parameters of the force fields are optimized empirically to reproduce both *ab initio* data and experimental observables. It was shown recently that – apart from appropriate simulation conditions – the quality of the force field is a crucial ingredient in obtaining reliable computational results in simulations of lipid bilayers [299].

There are two most commonly used lipid force fields nowadays. The all-atom model CHARMM27 [127], evolved from the old CHARMM22 [300], was optimized on the condensed phase properties of alkanes. Similarly, the united-atom model of Berger *et al.* [128, 301] (aliphatic hydrogen atoms implicitly treated), based on the united-atom version of Optimized Potential for Liquid Simulations (OPLS) [302], was parametrized against pentadecane. Both models have been applied extensively in a variety of membrane and membrane-protein studies and proved to show fairly agreeable results. Often, the Berger force field is preferred due to the greatly reduced computational cost with respect to all-atom lipid force fields [129]. Frequently, the united-atom force field for lipids is combined with the all-atom OPLS [125] force field for the simulation of protein-membrane systems instead of the more consistent CHARMM force field for both lipids and proteins. The combination of different force fields, however, is not straightforward and requires careful investigation [129].

The main focus in parametrizations and tests of the lipid force field is typically on the reproduction of experimentally accessible lipid bilayer properties such as the electron density profile, the area per lipid, the lipid order parameters, and the thickness of the membrane. These are generally well reproduced, with a few exceptions like the measured difference in the order parameters of the C2 atoms between the two acyl chains (typically similar in the force fields) or a too low lipid headgroup hydration at low water content [299]. Also protein-lipid interactions in combined Berger/GROMOS or Berger/OPLS lipid-protein simulations are possibly overestimated, resulting in drastic changes of lipid properties upon insertion of proteins [129, 260]. This is a consequence of the lack of experimental data on protein-lipid interactions to be used in parametrizations.

Deviations from experiment were also observed for the partitioning of anesthetics in lipid membranes: MD simulations of the spontaneous insertion of 1-alkanols of varying chain lengths into phosphatidylcholine bilayers applying the united-atom Berger force field for the lipids and the GROMOS force field for the 1-alkanols resulted in satisfying partition coefficients for the long-chain 1-alkanols [30]. However, for ethanol the partition coefficient was increased by a factor of 7–200 with respect to experiment, depending on the force field chosen for ethanol [30, 219]. Similar large ethanol partition coefficients were also obtained by consistently applying the CHARMM27 all-atom force field [303].

Recently, the general all-atom AMBER force field (GAFF) was developed [130]. In contrast to CHARMM and the previous version of AMBER, it is designed to be a general purpose force field, allowing extension to arbitrary organic molecules while keeping consistency with the parameters and forms of the existing force field. In principle, GAFF can also be used in membrane simulations, and in fact, Jójárt and Martinek [131] reported a tens of nanosecond test on GAFF in palmitoyoleoylphosphatidylcholine (POPC) lipid bilayer simulations in various ensembles, which showed its potency in good agreement with experimental values. Thus, GAFF is expected to open the lane toward a consistent all-atom force field for proteins, lipids, and other arbitrary organic molecules.

Here, we developed the all-atom GAFF for dioleoylphosphatidylcholine (DOPC) combined with restrained electrostatic potential (RESP) [304, 305] atomic partial charges. In a first step, structural and dynamical properties of a fully hydrated DOPC bilayer were compared to those obtained applying the united-atom force field of Berger *et al.* and with the all-atom CHARMM27 force field. Besides the structural and dynamical properties of the lipid bilayer, special emphasis was put on water properties close to the lipid-water interface and the resulting electrostatic potential across the phospholipid bilayer. Despite overall agreement in the reproduction of coarse properties of lipid bilayers, the force fields showed distinct differences in the phospholipid headgroup orientation, the water content of the interfacial region, the orientation of the carbonyl group, and the order of the two acyl chains. For the latter, only GAFF reflected the experimentally found order asymmetry at the beginning of the chains.

5.2 Methods

5.2.1 Initial structures

Two different systems of DOPC bilayers were set up for this study: A full-atomistic model (with 72 DOPC lipids) for use with the general AMBER (GAFF) [130] and the CHARMM force fields [127], and a united-atom model (128 DOPC lipids) for use with the Berger force field [128, 301].

A full-atomistic, pre-equilibrated DOPC bilayer [306] (1,500 ps snapshot, available from [307]) was taken as the starting structure. It consists of 72 lipids at low hydration with only five to six water molecules per lipid. To ensure full hydration, the simulation

box was enlarged, and additional water molecules were added to the water phase to attain a water to lipid ratio of 37.9 (above the suggested experimental value of 32.5 [308]). In total, the simulation system contained 2727 water molecules, forming a water slab of about 1.8 nm thickness. The simulation system consists of 18 117 atoms.

The united-atom model was created from a pre-equilibrated POPC membrane model of 128 lipids (100 ns) used in our previous study [229]. To convert to the DOPC model, two additional $-CH_2-$ groups were added to the palmitoyl chain of each POPC lipid in a *trans* configuration. Additionally, the single bond between carbon atoms 9 and 10 was changed to be double bonded. The number of water molecules was 4798 resulting in a water to lipid ratio of 37.4. The total system size was 21 279 atoms.

5.2.2 Force fields parameters

Three popular force fields were chosen in this study. The lipid parameters for the united-atom model of DOPC were based on Berger. Parameters for the unsaturated carbons, however, were taken from the GROMOS87 force field [309]. The CHARMM27 force field for DOPC was converted to GROMACS topology (conversion script kindly provided by Mark Abraham). Note that the conversion is not exact and dihedrals were fitted to Ryckaert–Bellemans dihedrals to reproduce the CHARMM27 [127] force field the best. For GAFF, the atomic charges for the lipids were evaluated using antechamber with the RESP potential fit method [304, 305] after an *ab initio* HF/6-31G* calculation using the Gaussian03 program package [310] and fitting the electrostatic potential at points selected according to the Merz–Singh–Kollman scheme. The RESP fitted charges from 72 lipid conformations taken from the Feller model were averaged and rounded to two decimal points. The rounding was done with preference to conserve the total charge on a chemical group.

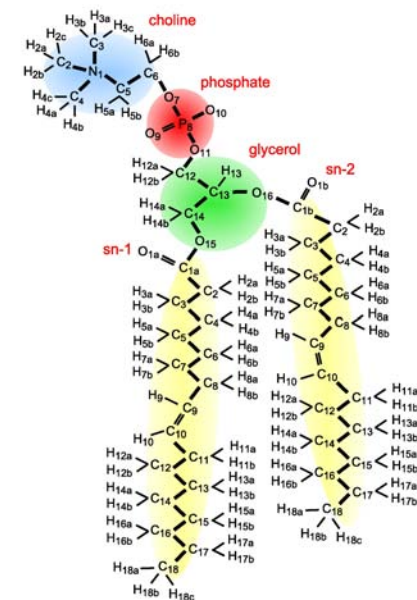
As shown in Table 5.1, the total charges on the choline and phosphate groups, on the glycerol backbone, on the carbonyl groups, and the acyl chains are similar for all investigated force fields. Differences are especially seen in the charge distribution of the choline group: the nitrogen atom is almost uncharged in GAFF but highly negatively charged in the CHARMM27 and in the Berger force field. The acyl chain atoms are neutral in the Berger force field; for GAFF only the beginning of the chain (C2 atom), the unsaturated carbons and the attached hydrogens, as well as the terminal methyl groups

carry charges significantly different from 0. In contrast, all atoms of the acyl chains have non-negligible charges in the CHARMM27 force field.

For the DOPC bilayer simulation applying the Berger force field the Simple Point Charge (SPC) water model [311] was chosen as this force field was developed with SPC water. For the same reason, the bilayer applying the CHARMM27 lipid force field was solvated with TIP3P water [312]. For the newly developed GAFF, both the Extended Simple Point Charge (SPC/E) [313] water model and the TIP3P water model (starting from a snapshot of the SPC/E system after 100 ns) were chosen for comparison.

Table 5.1: (Left) The atom-types and the partial charges of all atoms used in the respective force fields. (Right) Schematic drawing of the DOPC lipid and the naming convention used in this manuscript.

name	GAFF		CHARMM27		BERGER		name	GAFF		CHARMM27		BERGER	
	type	charge	type	charge	type	charge		type	charge	type	charge	type	charge
choline	Σ	1.1	Σ	1.1	Σ	1.4	acyl chain	Σ	0.0	Σ	0.1	Σ	0.0
N1	n4	0.02	NTL	-0.60	LNL	-0.50	C2	c3	-0.12	CTL2	-0.08	LP2	0.000
C2	c3	-0.12	CTL5	-0.35	LC3	0.40	H2a/b	hc	0.05	HAL2	0.09	LP2	0.000
H2a/b/c	hx	0.11	HL	0.25			C3	c3	-0.02	CTL2	-0.18	LP2	0.000
C3	c3	-0.12	CTL5	-0.35	LC3	0.40	H3a/b	hc	0.02	HAL2	0.09	LP2	0.000
H3a/b/c	hx	0.11	HL	0.25			C4	c3	-0.03	CTL2	-0.18	LP2	0.000
C4	c3	-0.12	CTL5	-0.35	LC3	0.40	H4a/b	hc	0.02	HAL2	0.09	LP2	0.000
H4a/b/c	hx	0.11	HL	0.25			C5	c3	-0.02	CTL2	-0.18	LP2	0.000
C5	c3	-0.01	CTL2	-0.10	LH2	0.30	H5a/b	hc	0.01	HAL2	0.09	LP2	0.000
H5a/b	hx	0.09	HL	0.25			C6	c3	-0.02	CTL2	-0.18	LP2	0.000
C6	c3	0.16	CTL2	-0.08	LC2	0.40	H6a/b	hc	0.01	HAL2	0.09	LP2	0.000
H6a/b	h1	0.06	HAL2	0.09			C7	c3	-0.02	CTL2	-0.18	LP2	0.000
phosphate	Σ	-1.28	Σ	-1.2	Σ	-1.4	H7a/b	hc	0.02	HAL2	0.09	LP2	0.000
O7	os	-0.42	OSL	-0.57	LOS	-0.80	C8	c3	0.04	CTL2	-0.18	LP2	0.000
P8	p5	1.12	PL	1.5	LP	1.70	H8a/b	hc	0.03	HAL2	0.09	LP2	0.000
O9	o	-0.78	O2L	-0.78	LOM	-0.80	C9	c2	-0.25	CEL1	-0.15	LH1	0.000
O10	o	-0.78	O2L	-0.78	LOM	-0.80	H9	ha	0.13	HEL1	0.15	LH1	0.000
O11	os	-0.42	OSL	-0.57	LOS	-0.70	C10	c2	-0.24	CEL1	-0.15	LH1	0.000
glycerol	Σ	-0.1	Σ	-0.32	Σ	-0.2	H10	ha	0.13	HEL1	0.15	LP2	0.000
C12	c3	0.06	CTL2	-0.08	LC2	0.40	C11	c3	0.02	CTL2	-0.18	LP2	0.000
H12a	h1	0.08	HAL2	0.09			H11a/b	hc	0.03	HAL2	0.09	LP2	0.000
H12b	h1	0.08	HAL2	0.09			C12	c3	-0.01	CTL2	-0.18	LP2	0.000
C13	c3	0.14	CTL1	0.04	LH1	0.30	H12a/b	hc	0.01	HAL2	0.09	LP2	0.000
H13	h1	0.13	HAL1	0.09			C13	c3	-0.00	CTL2	-0.18	LP2	0.000
C14	c3	0.01	CTL2	-0.05	LC2	0.50	H13a/b	hc	0.00	HAL2	0.09	LP2	0.000
H14a	h1	0.10	HAL2	0.09			C14	c3	-0.00	CTL2	-0.18	LP2	0.000
H14b	h1	0.10	HAL2	0.09			H14a/b	hc	0.00	HAL2	0.09	LP2	0.000
O15	os	-0.40	OSL	-0.34	LOS	-0.70	C15	c3	-0.02	CTL2	-0.18	LP2	0.000
O16	os	-0.40	OSL	-0.34	LOS	-0.70	H15a/b	hc	0.01	HAL2	0.09	LP2	0.000
carbonyl	Σ	0.28	Σ	0.22	Σ	0.2	C16	c3	-0.01	CTL2	-0.18	LP2	0.000
C1a	c	0.71	CL	0.63	LC	0.80	H16a/b	hc	0.01	HAL2	0.09	LP2	0.000
O1a	o	-0.57	OBL	-0.52	LO	-0.60	C17	c3	0.02	CTL2	-0.18	LP2	0.000
C1b	c	0.71	CL	0.63	LC	0.70	H17a/b	hc	0.01	HAL2	0.09	LP2	0.000
O1b	o	-0.57	OBL	-0.52	LO	-0.70	C18	c3	-0.13	CTL3	-0.27	LP3	0.000
							Ha/b/c	hc	0.03	HAL3	0.09		



5.2.3 Simulation conditions

All simulations were performed using the GROMACS package [161, 212]. Periodic boundary conditions were applied in all directions. The system was separately coupled to a temperature bath at 310 K for the lipids and the water molecules with a coupling time constant of 0.1 ps^{-1} [142]. Bonds to H-atoms were constrained using the LINCS [215] and the SETTLE algorithms [216]. This allowed for an integration step size of 2 fs. The nonbonded pair list was updated every ten steps with a cutoff of 1.0 nm. For the short range van der Waals interactions, a cutoff distance of 1.0 nm was used. In treating the long-range electrostatics, the particle-mesh ewald method with a grid spacing of 0.12 nm and cubic interpolation was adopted.

Two systems were simulated at constant pressure (GAFF all-atom and Berger united-atom, systems A and E in Table 5.2), applying a semi-isotropic pressure coupling with a barostat relaxation time of 1 ps at a pressure of 1 bar [142]. In order to ensure an area per lipid in agreement with experiment, DOPC bilayers simulated applying all-atom force fields were additionally subjected to a surface tension γ ($\gamma = 22 \text{ dyn/cm}$ per surface; systems B, C, and D). In the following, constant temperature and pressure conditions will be termed *NPT* ensembles, simulation conditions including surface tension *NP γ T* ensembles. However, note that the Berendsen thermostat and barostat do not strictly provide a correct *NPT* ensemble. The volume compressibility was chosen to $4.5 \times 10^{-5} \text{ bar}^{-1}$. Data were collected every picosecond.

All simulation systems were energy minimized with the steepest descent method and subsequently simulated for 100 ns each. For the analyses, the first 20 ns were disregarded due to equilibration effects. Table 5.2 gives a summary of the simulation systems presented in this manuscript. With a combination of different force fields, pressure coupling methods, and water models, a total of five systems were studied and compared.

5.2.4 Analysis

Lipid order parameter

The lipid order parameter, S_{CD} , is a direct measurement of the acyl chain order or disorder from the quadrupolar splitting in the NMR experiment. For the simulations, the

Table 5.2: Overview of the simulation systems presented in this study.

system	# lipid	#water	lipid force field	water model	ensemble
A	72	2727	GAFF all-atom	SPC/E	<i>NPT</i>
B	72	2727	GAFF all-atom	SPC/E	<i>NPγT</i>
C	72	2727	GAFF all-atom	TIP3P	<i>NPγT</i>
D	72	2727	CHARMM all-atom	TIP3P	<i>NPγT</i>
E	128	4789	Berger united-atom	SPC	<i>NPT</i>

molecular order parameter is given by [19]:

$$S_{ij} = \frac{1}{2} \langle 3 \cos \theta_i \cos \theta_j - \delta_{ij} \rangle \quad (5.1)$$

where θ_i is the angle between the i th molecular axis ($i, j = x, y, z$) and the bilayer normal. When the C_nH bond vector is used as the molecular axis (say, z), then S_{zz} gives the experimentally measured S_{CD} value [314]. For the united-atom model which contains no explicit hydrogen atoms in the carbon tails, the segmental vector C_{n-1} to C_{n+1} is taken as the molecular axis of the C_n methylene group, about which the segment motion is assumed to be axially symmetric. Then, the deuterium order parameter S_{CD} is approximated by the following relations for saturated and unsaturated carbon tail atoms [315]:

$$-S_{CD}^{sat} = \frac{2}{3} S_{xx} + \frac{1}{3} S_{yy} \text{ and} \quad (5.2)$$

$$-S_{CD}^{unsat} = \frac{1}{4} S_{zz} + \frac{3}{4} S_{yy} \mp \frac{\sqrt{3}}{2} S_{yz} . \quad (5.3)$$

Lipid and water diffusion

The self-diffusion coefficient D of molecules can be calculated from the Einstein relation on Brownian motion:

$$2d_f D = \lim_{t \rightarrow \infty} \frac{1}{t} \langle (r(t) - r(0))^2 \rangle \quad (5.4)$$

where d_f is the number of translational degrees of freedom (for lateral diffusion $d_f = 2$), and $r(t)$ is the position of the molecule at time t . In practice, the lateral self-diffusion coefficient is estimated from the slope of the molecule's mean-square displacements (msds)

(e.g., taken on the center of mass (c.m.) coordinates) in a defined time window averaged over all molecules N [229]:

$$d^2(t) = \frac{1}{N} \frac{\Delta t}{T-t} \sum_{i=1}^N \sum_{t_0=0}^{T-t-1} |r(t_0) - r(t_0 + t)|^2 . \quad (5.5)$$

The first sum runs over the N molecules and the second sum runs over all time frames smaller than $T - t$, where T is the sampling time (Δt is the time between two subsequent conformations).

For the lipids, the lateral msds were corrected for the c.m. motion of the respective monolayer [229]. c.m. removal allows a correction for correlated unidirectional motions. For the investigated system sizes the c.m. removal likely yields a too small value for the lipid diffusion [316]. However, without c.m. removal the diffusion coefficient might be severely overestimated due to correlations even with the second lipid shell around a molecule: Transitions will propagate over distances larger than the box size [316] (for the 72 lipid system). The errors were estimated by splitting the trajectories into pieces of 20 ns length (block averaging).

To obtain a spatially resolved water diffusion coefficient, the simulation box was divided into 40 slabs (i.e., $\approx 2 \text{ \AA}$ per slab) and the lateral diffusion in each slab was calculated by considering only the water molecules located in the same slab at time t_0 and at time $t_0 + t$. Block averaging from 5 ns pieces of the production trajectory was used to obtain the mean and standard error of the coefficients. For comparison, additional simulations of pure water boxes (containing 2182 water molecules, 5 ns simulation length each) yielded bulk water diffusion coefficients for the investigated water models.

Electrostatic potential

The electrostatic potential across the phospholipid bilayer was calculated by double integration of the averaged charge density ρ across the bilayer,

$$\phi(z) - \phi(z_0) = -\frac{1}{\epsilon_0} \int_{z_0}^z dz' \int_{z_0}^{z'} \rho(z'') dz'' . \quad (5.6)$$

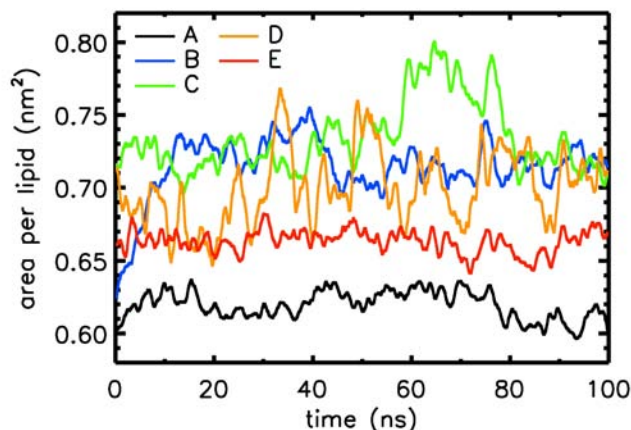


Figure 5.1: Area per lipid for the five investigated systems in 100 ns simulation time smoothed by a sliding window of 1 ns length. Larger fluctuations were observed for systems applying surface tension (B, C, and D) as compared to those using semi-isotropic pressure coupling (A and E). Note that the experimental area per lipid for DOPC was measured to be 0.721 nm^2 at 30° C [317].

5.3 Results

5.3.1 Area per lipid

The area per lipid is frequently used as a measure for the equilibration of the lipid bilayer system or to monitor phase transitions. In practice, the area per lipid is obtained as the lateral area of the simulation box (the xy-plane) divided by the number of lipids in one monolayer. In Fig. 5.1, the area per lipid for the 100 ns trajectory of each simulation system is presented. Equilibration in the area per lipid is reached after approximately 20 ns for each system, and the analyses were conducted on the final 80 ns of the trajectories.

For a DOPC simulation applying the CHARMM27 force field without surface tension (data not shown) the area per lipid decreased to 0.56 nm^2 within 16 ns. This transition to a gel-like state was previously observed for a dipalmitoylphosphatidylcholine (DPPC) bilayer applying the same force field in the *NPT* ensemble [318, 319]. Also, in a comparative simulation study of a DOPC bilayer at low hydration between the CHARMM and Berger force field in the *NPT* ensemble, a too small area per lipid was reported for the CHARMM27 force field [90]. The transition to a gel-like state can be prevented by application of a surface tension $\gamma = 22 \text{ dyn/cm}$ (system D). Also for GAFF in

Table 5.3: Averages and errors of the membrane structural parameters calculated by block averaging (block length 20 ns).

system	area per lipid (nm ²)	membrane thickness (nm)
<i>expt</i> †	0.721	3.71
A	0.62 ± 0.01	4.00 ± 0.05
B	0.72 ± 0.01	3.61 ± 0.04
C	0.74 ± 0.03	3.51 ± 0.13
D	0.71 ± 0.01	3.63 ± 0.13
E	0.66 ± 0.01	3.72 ± 0.11

The membrane thickness was measured as the distance between the two peaks in the system electron density profiles. Errors in the area per lipid for systems D and E were rounded to 0.01 nm². †The experimental values were measured by Liu and Nagle [317] using fully hydrated DOPC bilayers at 30° C.

the *NPT* ensemble the area per lipid was well below the crystallographic value (0.62 nm² versus 0.72 nm²). Test simulations showed the best agreement to experimental data in the *NP γ T* ensemble by applying the same surface tension γ as for the CHARMM27 system (tested values $\gamma = 22, 30, 35$ dyn/cm).

Table 5.3 shows that the area per lipid agrees favorably with the experimental value of 72 Å² for the GAFF and CHARMM27 systems (B, C, and D). However, lipids simulated in the Berger force field (*NPT*, system E) were too densely packed (area per lipid 8% below experiment).

5.3.2 Lipid headgroup orientation

Differences among the force fields in the lipid headgroup region are reflected, e.g., in the headgroup tilt with respect to the bilayer normal. The headgroup tilt was taken as the angle between the vector connecting the phosphorus and the nitrogen atoms and the bilayer normal. The most probable orientations as well as the width of the distribution of tilt angles are summarized in Table 5.4. The largest lipid headgroup tilt angles were observed for the Berger force field (86°, system E) and the smallest for GAFF (59° for system A, 67° for system B). The distribution of tilt angles is broad for all investigated force fields, with a width at half maximum from 62° (CHARMM27) to 88° (Berger). The difference in the lipid headgroup tilt is also reflected in the electron density profiles across the bilayer (see below). The straightened headgroup orientation in the CHARMM27 force field and in GAFF enabled an increased water content in the interfacial membrane-water region.

Table 5.4: Distribution of lipid headgroup orientations and the lipid dipole moments.

system	most probable orientation (°)	width at half maximum (°)	$M \pm \sigma$ (D)	M_z (D)
A	59	79 $\begin{pmatrix} +46 \\ -33 \end{pmatrix}$	23.2 ± 3.8	4.3
B	67	74 $\begin{pmatrix} +36 \\ -38 \end{pmatrix}$	23.2 ± 2.8	4.0
C	69	82 $\begin{pmatrix} +39 \\ -43 \end{pmatrix}$	23.3 ± 2.7	3.5
D	73	62 $\begin{pmatrix} +32 \\ -30 \end{pmatrix}$	23.7 ± 3.2	2.1
E	86	88 $\begin{pmatrix} +32 \\ -56 \end{pmatrix}$	27.1 ± 3.8	8.1

The headgroup orientation is computed as the angle between the vector connecting the phosphorus and the nitrogen atoms and the bilayer normal. Both the maximum of the distribution – the most probable orientation – and its width are given. The last two columns give the most probable total dipole moment (in Debye) of the individual lipids in the respective force fields (\pm the width of a fitted Gaussian distribution) as well as the average of the dipole moment along the bilayer normal (z-direction).

5.3.3 Lipid order parameter

The ensemble averaged deuterium lipid order parameters $|S_{CD}|$ of the two carbon tails are separately shown in Fig. 5.2. All systems displayed the general trend of decreasing order along the chain toward the core of the bilayer with a prominent dip close to or at the double-bond segment (carbon atoms 9 and 10). Similar characteristics were observed for the oleoyl chain of POPC by deuterium NMR [320] and in MD simulations (see e.g., the recent work by Pandit *et al.* [321]), and on DOPC by the DROSS NMR technique [322]. Both ^2H -NMR and ^2H - ^{13}C DROSS NMR found the dip located at the C10 atom.

In the MD simulations, however, the position of the central discontinuity differed among the investigated force fields: It occurred in both chains at C9 for CHARMM27 (D), and at C10 for Berger (E), while for GAFF (B) the dip is seen at C11 for the *sn*-1 chain and at C10/C11 for the *sn*-2 chain (see Table 5.1 for the naming). Atoms more far away from the glycerol backbone (C12–C18) showed the same order for both chains in all force fields, which is in agreement with NMR data. This finding was even observed for the saturated and unsaturated chains of POPC [320].

In contrast, deuterium NMR revealed differences close to the glycerol backbone even for identical chains: In studies on DPPC [323] and POPC [320] a distinctly smaller order was observed for the C2 atom of the *sn*-2 acyl chain as compared to the *sn*-1 chain. This inequivalence of the chains close to the glycerol backbone was found to be indepen-

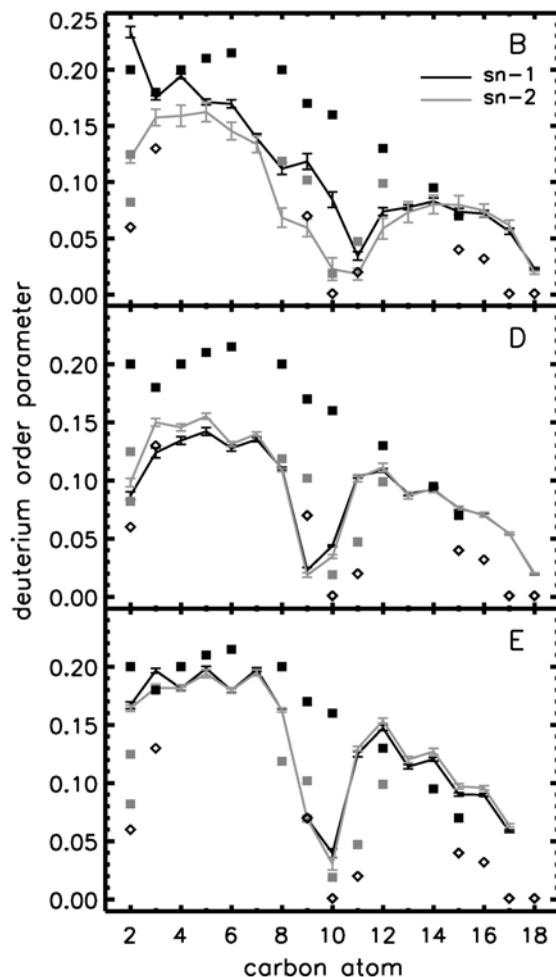


Figure 5.2: Deuterium order parameters, $|S_{CD}|$, for the two acyl chains of DOPC lipids analyzed for systems B, D, and E. Error bars indicate the errors of the means from block averaging (blocks of 20 ns length). Experimental values are given for the POPC *sn*-1 (black squares) and *sn*-2 chain (gray squares) at 27°C [320], and for DOPC *sn*-2 at 37°C [322] (\diamond symbols). Note that the double-bonded carbon atoms are at position 9 and 10.

dent of the polar headgroup and thus to be a general feature of phospholipids within membranes [320]. From NMR results it was concluded that the orientations in the beginning of the chains differ significantly with chain 1 being oriented perpendicular and chain 2 parallel to the bilayer surface [323]. The suggestion of different conformations of the beginnings of the two chains was supported by x-ray diffraction studies [324]. Only the new GAFF for DOPC reflected the general order characteristics with a significantly enhanced order for the C2 atom of the *sn*-1 chain. The Berger and CHARMM27 force

fields show similar profiles for both chains close to the glycerol backbone as was also observed in earlier studies based on multianosecond simulations [30, 292, 325]. For DPPC, the C2 order for the *sn*-1 chain was even reported to be smaller than that of the *sn*-2 chain applying the CHARMM27 force field [127]. A previous study on DOPC [326] applying a modified GROMOS96 force field [327] reported tiny differences for the C2 order parameters between the chains, together with the dip located at the C9 [326] atom similar to the CHARMM27 force field or at the C10 atom [327].

The conformation in the beginning of the acyl chain is described by the orientation of the vector connecting the C1 and the C2 atom: For both CHARMM27 and GAFF lipids, chain 1 is oriented perpendicular to the bilayer surface (maximum of the probability distribution of angles to bilayer normal $\approx 180^\circ$, data not shown). While the distribution is only slightly shifted to smaller angles for chain 2 in CHARMM27 (163° , width 44°), the second chain adopts a significantly different orientation with respect to chain 1 in GAFF (133° , width 27°). Like for CHARMM27, the orientations of the C1–C2 vector for the Berger force field are similar with 160° and 144° for the two chains.

In the deuterium NMR experiment [320], two signals were observed at C2 indicating a nonequivalence of the two hydrogen positions only in this segment, due to different average orientations [328]. For the all-atom GAFF and CHARMM systems, the order parameter of each individual C–H bond can be determined separately. In the simulations (data not shown) the order of the two hydrogens is very similar in all methylene segments including in the C2 segment. The difference of the mean between the two hydrogens in C2 is only 0.01 for GAFF and is 0.02 for CHARMM, while the experimental difference is about 0.05. Hence, the nonequivalent feature at C2 cannot be reproduced by any of the tested force fields.

5.3.4 Density profile and membrane thickness

Electron density profiles of the simulated membrane systems can directly be compared to x-ray experimental data. Fig. 5.3 shows the overall electron density and the electron densities of individual chemical groups of the bilayer.

The total electron density of the GAFF system without surface tension (A) shows

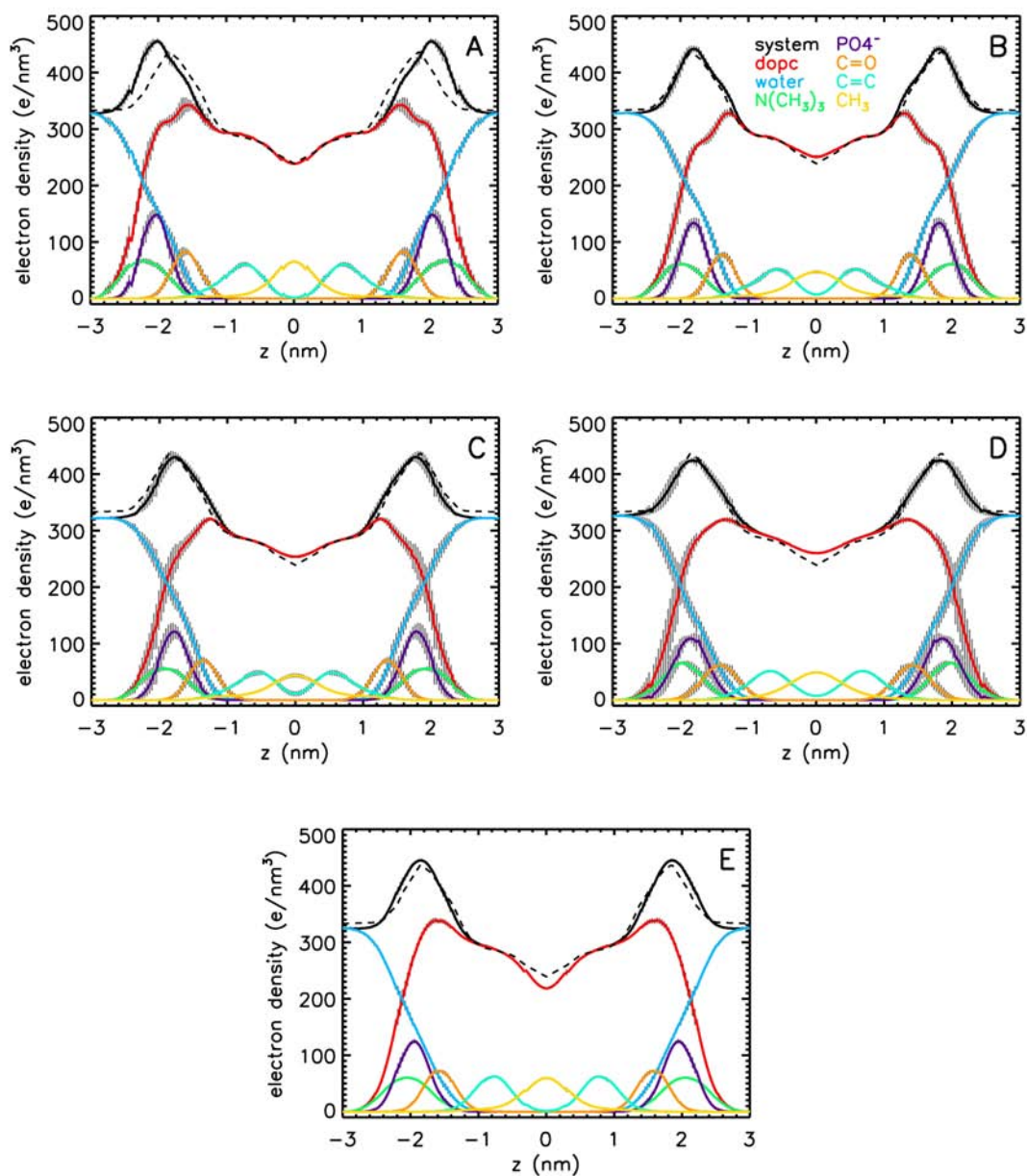


Figure 5.3: The (symmetrized) electron density profiles of the overall and individual chemical components of all simulation systems. The profiles are centered at the core of the bilayer, and the standard errors (as shown here in *gray* lines) are calculated by dividing the trajectories into blocks of 20 ns length. The profile was computed by placing the appropriate number of electrons at the center of atomic nuclei binning along the direction of the membrane normal (bin width of 0.3 Å). The experimental density profile [317] is shown as a *dashed* line.

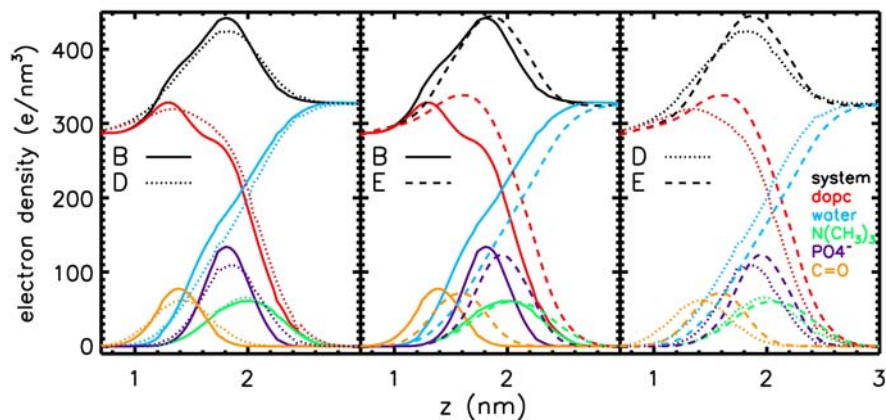


Figure 5.4: Comparison of the electron density profiles at the membrane-water interface (centered on the lipid bilayer) for force field combinations GAFF-SPC/E, CHARMM27-TIP3P, and Berger-SPC (systems B, D, and E).

good agreement with the x-ray data in the hydrophobic core region. However, the membrane thickness measured as the distance between the maxima of the electron density profiles is increased by $\approx 3 \text{ \AA}$ with respect to experiment (see Table 5.3). The GAFF-SPC/E system applying surface tension (B) revealed overall excellent agreement with the experimental profile. Using the TIP3P instead of the SPC/E water model together with GAFF (C) resulted in a decreased density at the membrane-water interface.

Also the electron density profile obtained for the CHARMM27 system (D) agrees well with the experimental profile, except for the region of the central methyl groups for which the density is significantly enhanced with respect to experiment. Interestingly, systems with the TIP3P water model showed enhanced bilayer fluctuations, resulting in increased error bars for the membrane thickness (Table 5.3).

Although the membrane thickness is best modeled by the Berger force field (E), the electron density profile is at variance with the x-ray data. The headgroup region is broadened, and the methyl group region is underestimated.

For comparison between the investigated force fields, Fig. 5.4 shows a close-up view of the membrane-water interface for the GAFF-SPC/E, CHARMM27-TIP3P, and Berger-SPC force field combinations. Although the membrane thickness is similar for all

three force fields, both GAFF and CHARMM27 show a drastically increased water content (*blue* lines) in the lipid headgroup region as compared to Berger (with root mean square deviations, rms, of 37 and 27 e/nm³, respectively), coupled to a decreased DOPC electron density (red lines, with rms of 31 and 20 e/nm³, respectively). While the membrane thickness between Berger and the all-atom systems differs only by 1 Å, the carbonyl groups are shifted for Berger-SPC by ≈ 2 Å towards the headgroup region. The hydration of the carbonyl oxygens is significantly lowered for Berger lipids with respect to CHARMM27 and GAFF: The cumulative radial distribution yielded an average of only 1.5 water molecules around both carbonyl oxygens for Berger (taken at the first minimum of the radial distribution function, 0.55 for the *sn*-1 chain), but 3.4 (1.7) and 2.9 (1.4) water molecules for CHARMM27 and GAFF lipids, respectively.

5.3.5 Lipid and water diffusion

Lipids in the liquid crystalline phase diffuse in the plane of the bilayer due to thermal agitation. This diffusive movement can roughly be classified into two regimes: Fast fluctuation of the lipid in the local solvation cage [329] and a relatively slow but long distance diffusion in the bilayer. Different experimental methods acting on different time scales therefore obtain lipid diffusion coefficients differing by two to three orders of magnitude.

As shown in Fig. 5.5 (upper panel) the lipid msd for all systems clearly showed the existence of both long-range and short-range diffusion behaviors of lipids, with a smooth transition between the two regions. In order to determine the linear segment in the msd curve (long-range diffusion), the diffusion coefficient D was calculated using different time windows for the linear fit.

The values for D (Fig. 5.5, lower panel) converged between 3 ns (for systems A, B, and E) and 5 ns (C and D). Therefore, the diffusion coefficients for long-range lipid diffusion were consistently computed from a linear fit to the msd between 5 and 10 ns. The data are summarized in Table 5.5. With the exception of the bilayer simulated applying the CHARMM27 force field (system D), all computed diffusion coefficients are smaller by a factor of 2–8 as compared to the experimental value of $D = 13.7 \times 10^{-8} \text{ cm}^2\text{s}^{-1}$ (NMR on oriented bilayers at 308 K [330]). Interestingly, the DOPC diffusion is also strongly dependent also on the force field used for the water molecules: While GAFF combined with SPC/E water yields a lipid diffusion coefficient of $D = 3.1 \pm 0.9 \times 10^{-8} \text{ cm}^2\text{s}^{-1}$,

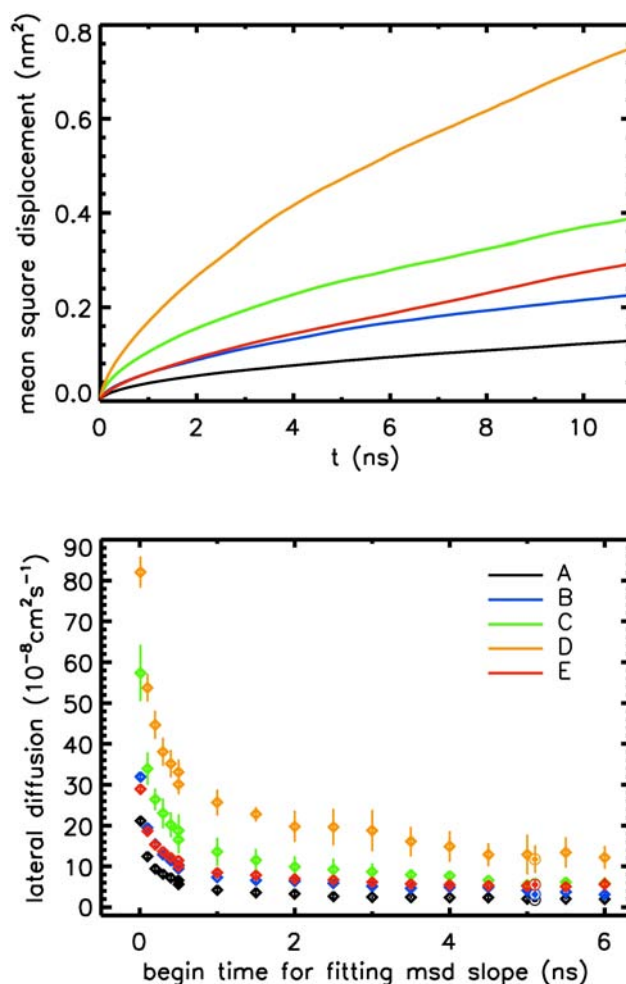


Figure 5.5: Lipid diffusion coefficients calculated for different time lengths of the simulations by block averaging: The trajectory was divided into 20 ns pieces and the msd (upper panel) was calculated separately for each block. Diffusion coefficients (lower panel) computed for different time ranges were obtained by fitting different time windows of the msd curve. For the short-range diffusion (colored \diamond symbols), shorter time windows of 100 ps (fit starts between 10 and 500 ps) and 500 ps (fit starts between 500 ps and 6 ns) were used. For the long-range diffusion (colored \odot symbols) fitting was done on the linear segment of the msd curve between 5 and 10 ns.

the diffusion is almost enhanced by a factor of 2 for GAFF combined with TIP3P water. Thus the increased bulk water diffusion of TIP3P with respect to SPC/E (see below) has also a pronounced influence also on the lipids in a bilayer. Although the area per lipid is similar for both systems, the long-range lipid diffusion is about two times larger for

Table 5.5: The calculated mean lateral diffusion coefficient for water molecules and for DOPC molecules.

system	water diffusion ($\times 10^{-5} \text{cm}^2 \text{s}^{-1}$)	lipid diffusion ($\times 10^{-8} \text{cm}^2 \text{s}^{-1}$)
<i>expt</i>		13.7 [†]
A	2.27 ± 0.03	1.79 ± 0.51
B	2.07 ± 0.03	3.13 ± 0.94
C	4.31 ± 0.08	5.71 ± 1.06
D	4.60 ± 0.08	11.76 ± 3.39
E	3.63 ± 0.02	5.52 ± 1.00

For water diffusion, the average was calculated from all water molecules in the system regardless of the distance to bilayer. For lipid diffusion, the long-range diffusion coefficients are shown here while the short-range diffusions are depicted in Fig. 5.5. [†]The experimental lipid diffusion coefficient is taken from pulsed field gradient NMR experiments on oriented bilayers at 308 K [330].

the CHARMM27-TIP3P system as compared to GAFF-TIP3P. The CHARMM27 diffusion coefficient is, however, subject to a large error.

The diffusion coefficients obtained on the subnanosecond time scale decayed exponentially with increasing time scale. Values for the diffusion coefficient range between 5×10^{-8} and $82 \times 10^{-8} \text{cm}^2 \text{s}^{-1}$, depending on the time scale and on the applied force field, and are in agreement with experimental diffusion coefficients obtained for DPPC of $(10-100) \times 10^{-8} \text{cm}^2 \text{s}^{-1}$ [329, 331, 332].

The (lateral) water diffusion close to the phospholipid bilayer and in the interfacial region strongly depends on the water model applied in the simulation (see Fig. 5.6). While SPC/E water in GAFF simulations was largely immobilized in the interfacial region (*blue* and *black lines*, see also Lopez *et al.* [333]), both Berger-SPC and CHARMM27-TIP3P resulted in a comparably large water diffusion of $(1-3) \times 10^{-5} \text{cm}^2/\text{s}$. This is at least partially caused by the enhanced bulk diffusion values for these water models [334] as compared to experiment ($2.92 \times 10^{-5} \text{cm}^2/\text{s}$ at 35°C, see [335]).

5.3.6 Electrostatic potential and dipole moment

The electrostatic potential, or the dipole potential, is known to be an important factor for the permeation of ionic species through membranes, and the insertion and proper function or regulation of membrane proteins. Lipid polar headgroups, glycerol esters, as well as water molecules were found to contribute to the total electrostatic potential,

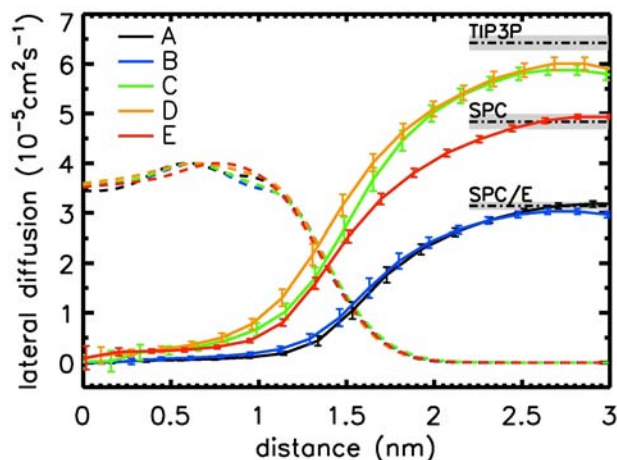


Figure 5.6: The lateral diffusion coefficients of water molecules (*solid* lines) at the membrane-water interface. The *dashed* lines mark the normalized DOPC electron density profiles (superimposed at the descending slope) to indicate the location of the bilayer. The respective values for bulk water diffusion are shown as *dashed-dotted* lines (errors in *gray* shading). All diffusion coefficients (and standard errors) were measured by fitting the slope between 2 and 200 ps of the msd curves, using block averaging of length 5 ns.

which arises from the nonrandom orientation of lipids and hydrated water in the bilayer. Experimentally, a fully saturated phospholipid was measured to have an electrostatic potential in the range of 220–280 mV [336, 337]. Introducing one unsaturated segment to the acyl chains would decrease the value of the potential by as much as 30 mV [338].

Fig. 5.7 shows the calculated electrostatics potential of all investigated force fields. Quantitatively, all profiles are larger by a factor of 3–4 as compared to experiment. Nevertheless, they are qualitatively in agreement with experiments [339], and in accord with previous simulation studies (see, e.g., [229, 340, 341]): the potential is positive inside the bilayer, the phospholipid headgroups contribute a negative potential (*solid* lines in Fig. 5.7, lower panel) which is overcompensated by the opposed water dipole orientation (*dashed* lines) in the interfacial region, resulting in a total positive electrostatic potential. The orientation of water dipoles was previously found to be reduced in the presence of salt ions [229].

Both all-atom force fields have a distinct potential maximum at the bilayer center, caused by the nonzero partial charges on the terminal methyl groups. While the total electrostatic potential for the CHARMM27 system rises first in the region of the carbonyl

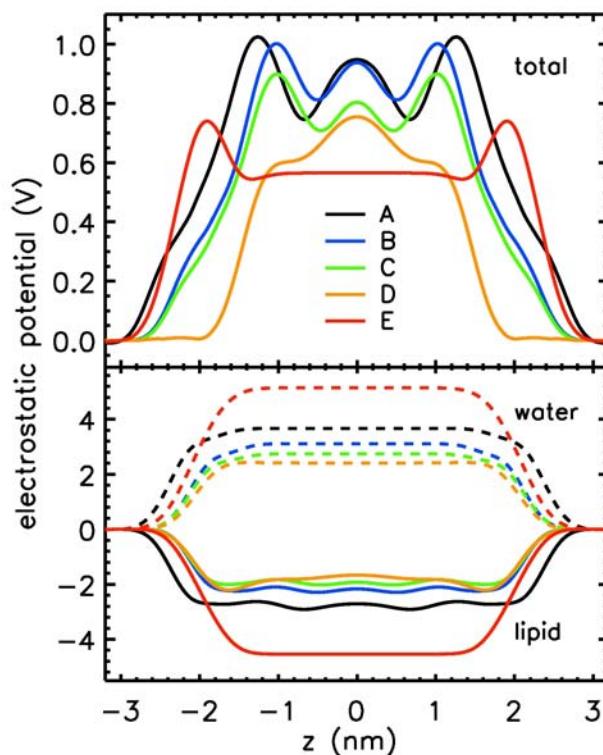


Figure 5.7: Total electrostatic potential (upper panel) and contributions (lower panel) due to the lipid dipoles (*solid lines*) and due to water dipole orientation (*dashed lines*) at the membrane/water interface across the DOPC bilayer (symmetrized). The potential was averaged over the final 80 ns of the simulation.

groups, the potential for the GAFF system steeply increases in the choline/phosphate region (similar for both investigated water models). For the latter, the potential decreases slightly towards the unsaturated carbons of the chains followed by the central maximum. The Berger force field showed a flat potential in the region of the hydrocarbon chains which is due to the uncharged hydrocarbon tail atoms.

Besides the PC headgroup, mainly the fatty acid carbonyl groups contribute to the molecular dipole moment (see also distribution of partial charges in Table 5.1). In crystal structures at very low hydration (two water molecules per lipid) an asymmetry between the carbonyl orientations of the *sn*-1 and *sn*-2 was observed [342, 343]. The *sn*-1 carbonyl oriented parallel to the bilayer plane and the *sn*-2 carbonyl was found in two different conformations, both pointing toward the water phase (partially negatively charged oxy-

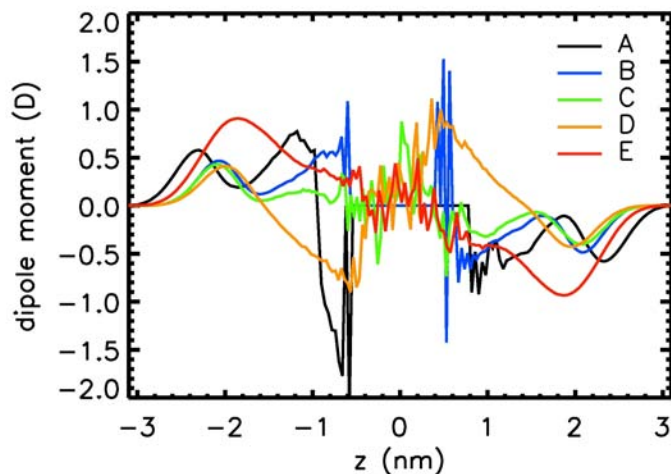


Figure 5.8: Average water dipole moment along the membrane normal. The large fluctuations inside the hydrophobic core of the lipid bilayer are due to individual water molecules spontaneously permeating the membrane.

gen pointing out of the hydrophobic core).

All force fields showed broad gaussian-like distributions of C=O orientations with respect to the bilayer normal (data not shown). Within the Berger force field, the most probable angle ϕ between the C=O vector and the membrane normal was shifted from 60° to 31° between the *sn*-1 and *sn*-2 carbonyls, the probabilities of finding angles below 90° (carbonyl pointing to the water phase, carbonyl dipole toward hydrophobic core) are 86% and 97%, respectively. For GAFF (with surface tension, SPC/E water), an increase in ϕ from 54° to 69° was observed, and the probability of finding a carbonyl pointing to the water phase is 93% for the *sn*-1 and 76% for the *sn*-2 carbonyl. The most probable carbonyl angles for the acyl chains in the CHARMM27 force field are 44° and 69° ; however, the probabilities for angles $\leq 90^\circ$ were similar for both chains with 70%.

The water order in the interfacial region is further investigated in Fig. 5.8 showing the mean dipole moment of water molecules depending on their position relative to the lipid bilayer. Both Berger and GAFF systems revealed two regions of positive water dipole moment (pointing into the membrane, opposite to the lipid dipoles), one in the region of the choline and phosphate groups and the second at the hydrophobic interface

close to the carbonyl groups. The water orientation is more pronounced for the Berger force field. This is due to the increased total dipole moment of Berger lipids ($\approx 15\%$ with respect to GAFF and CHARMM27) and the two times larger component of the dipole moment normal to the membrane (Table 5.4).

For the CHARMM27 system (D), the water dipole orientation at the interface headgroup-hydrophobic core is reversed with respect to the other force fields. Both the water model (TIP3P) and the significant amount of carbonyl dipoles pointing into the hydrophobic core ($\approx 30\%$) for CHARMM27 are presumably the cause for this reversed water dipole orientation.

5.4 Discussion

All three investigated lipid force fields were shown to correctly describe the coarse properties of phospholipid bilayers. However, the general feature of distinctly different C2 order parameters between the two acyl chains is observed only in the newly developed GAFF for DOPC. Neither of the investigated force fields could reproduce the experimentally observed C2 splitting in the *sn*-2 chain, and indeed the two methylene hydrogen positions were found equivalent along the acyl chains in both all-atom models. The C2 splitting was suggested to be due to two different conformations of the lipid molecule or due to the magnetic inequivalence of the C2 deuterons in the NMR experiment [320]. The simulations did not provide any evidence for different C2 order parameters coupled to different lipid conformations. Possibly, a polarizable lipid force field can induce an inequivalence of the two protons due to differential shielding at the hydrophobic/hydrophilic interface.

Also the different orientations in the beginning of the two chains with respect to the bilayer normal appear to be best described by GAFF. Interestingly, Jójárt and Martinek [131] did not observe significant differences between the C2 atom orders of the palmitoyl and the oleyl chains of POPC applying GAFF. This might be due to high sensitivity of RESP charges to the conformation of the molecule (charge calculation on 12 conformations [131] versus 72 conformations here). Order parameters reported for the recently developed GROMOS96 45A3 force field for phospholipids [344] also show an enhanced order for the C2 atom of the *sn*-1 chain (DPPC). However, the latter two studies were probably based on too short sampling times (4 ns and 300 ps, respectively). A

recent reparametrization of the partial charges in the CHARMM27 force field enabling simulations of the fluid phase in the *NPT* ensemble [319] did not yield improved C2 atom orders with respect to the original CHARMM27.

Both structural and dynamical properties of the aqueous solution at the water-phospholipid bilayer interface (for a thorough review on this topic see Berkowitz *et al.* [298]) were shown to depend on the phospholipid force field: The ordering of water molecules within the lipid-water interface crucially depends on the chosen lipid force field. For CHARMM27, the total electrostatic potential was shown to rise first in the region of the carbonyl groups. Together with the experimental finding that removal of the carbonyl groups only partly accounts for the positive electrostatic potential inside lipid bilayers [339] this may question the applicability of the CHARMM27 force field in cases where the potential is crucial to, e.g., the structure or function of membrane-associated proteins or in the electrostatically driven binding of molecules to membranes.

Also the water dynamics close to membrane interfaces is crucially dependent on the applied force field: CHARMM27 was developed applying the TIP3P water model, the Berger force field together with SPC water, and GAFF may be used with both TIP3P and with SPC/E. Only the SPC/E water correctly reflects the bulk water diffusion coefficient, TIP3P overestimates the bulk water diffusion by more than a factor of 2. For the CHARMM27 lipid bilayer simulation, the used 38 water molecules per lipid were not sufficient to reach full hydration, since the water diffusion between periodic bilayers did not reach the increased bulk water diffusion for the TIP3P water model. In contrast, for SPC and SPC/E water this hydration level was sufficient to reach the bulk water diffusion. The lateral diffusion coefficient for lipids is too small for GAFF and the Berger force field applying the SPC/E and SPC water models, respectively. In contrast, the CHARMM27 lipid force field shows a diffusion close to the experimental value. One possible reason may be due to the noteworthy charges on the acyl chain atoms in the CHARMM27 force field. Also, the diffusion is partly enhanced due to the large diffusion coefficient for water molecules applying the TIP3P model. Note that due to long-range correlations the lateral diffusion is dependent on the system size for small systems [316]. Here, due to the removal of unidirectional correlated motions the obtained results for the diffusion coefficient are likely too small.

5.5 Conclusion

In the present study we show simulation results for a DOPC membrane employing a newly developed all-atom force field based on GAFF. The performance of this force field against two existing parametrizations (the all-atom CHARMM27 and the united-atom model by Berger) is tested on a range of physical observables. The presented GAFF reproduces both the coarse properties such as the bilayer thickness and also the experimentally found differences in the structure and the order of the two acyl chains. In addition, GAFF offers a consistent force field for both lipids and membrane embedded proteins, thereby enabling detailed studies of the interaction between lipids and proteins. The extension of GAFF to other phospholipids is straightforward.

It has been argued that the *NPT* ensemble is appropriate for lipid bilayer simulations [128, 345, 346]. Both GAFF and the CHARMM27 lipid force field showed a transition to a gel-like state in this ensemble, making the use of a surface tension mandatory in simulations of the fluid (L_α) phase. The applied surface tension in our GAFF simulations was found to be approximately independent of the size of the bilayer patch (a four times larger bilayer did not show significant changes in the area per lipid, data not shown), and should be multiplied by the number of bilayers in the simulation system. Membrane-embedded proteins will modify the membrane pressure profile in a local environment around the protein. However, for melittin embedded in a DMPC bilayer (121 lipids), even similar lateral pressures were determined for the protein-lipid system (applying CHARMM27) as compared to the pure lipid bilayer [347]. Therefore, we expect the surface-tension to be only slightly affected for comparable dilute protein-lipid systems.

In case of CHARMM27, a reparametrization of the partial atomic charges has recently been shown to pave the way towards fluid phase simulations in the *NPT* ensemble for DPPC [319]. One possible reason for deviations from the fluid-like behavior of bilayers simulated in the *NPT* ensemble applying all-atom force fields may be the neglect of polarizability. Especially the large fields occurring at the interface between the highly polar water phase and the low-dielectric hydrocarbon interior underline the need for a careful investigation of polarization effects. To this end, development and tests of a polarizable model are currently under way.

Apart from the polarization issue, future studies will focus on the lipid-protein interaction in the different force fields. However, comparison to experimental data is currently limited due to the scarcity of detailed experimental studies on these interactions. Since GAFF easily allows extension to arbitrary organic molecules it can also be applied to systematic studies on the partitioning of solutes between the solvent and the bilayer, of great importance for a more thorough understanding of dose–response relationships in medicine. Knowledge about the binding characteristics may additionally prove useful for future drug development.

Acknowledgements

We thank Volkhart Helms for support with computing time and Beate Griepernau for help with the analysis. We thank Mark Abraham for providing the script for the conversion of the CHARMM27 force field to GROMACS, and for a lot of helpful discussions about its use. Financial support by the Deutsche Forschungsgemeinschaft (Graduate School *Structure Formation and Transport in Complex Systems*, No. 1276/1) is acknowledged. As members of the Center for Bioinformatics, Rainer A. Böckmann and Shirley Siu are supported by the Deutsche Forschungsgemeinschaft Grant BIZ 4/1. Robert Vacha and Pavel Jungwirth thank the Grant Agency of the Academy of Sciences (Grant No. A400400503) and the Czech Ministry of Education (Grant No. LC512). R.V. acknowledges support from the Granting Agency of the Czech Republic (grant 203/05/H001).

PDB files of equilibrated snapshots, and the GROMACS implementations of the used Berger and CHARMM27 force field as well as that of the developed GAFF for DOPC molecules are available free of charge on the websites:

<http://www.bioinf.uni-sb.de/RB>

<http://www.molecular.cz/~vacha/downloade.htm>.

Author Contributions:

Rainer A. Böckmann and Pavel Jungwirth designed research. The lipid force field was parameterized by Robert Vacha and Weng In Siu. Simulations were set up by Weng In Siu and Robert Vacha. The analysis was done by Weng In Siu and partly by Robert Vacha. The article was written by Weng In Siu and Rainer A. Böckmann.

Simulating Proton Transfer Using the Semi-Empirical Q-HOP Method

Summary

Although proton transfer (PT) is an important chemical reaction occurring in the cell, computational studies of the PT phenomena involving a large number of molecules in equilibrium are still a formidable task. Due to the quantum nature of the light-mass proton and the alternation of chemical bonds during proton transfer, an accurate description of PT requires computationally expensive quantum chemical techniques. A simplified semi-empirical model (Q-HOP) [140] allows the extension of PT studies to system sizes of the order of 10^4 atoms and nanosecond time scales. In the Q-HOP method, the proton hopping probability is calculated on-the-fly with analytically fitted functions depending only on the donor-acceptor distance and the change of the electrostatic energy of the system upon proton transfer from the donor to the acceptor.

In this study, we have implemented the Q-HOP method in the simulation package GROMACS. In addition to the original implementation, improvements were made to ensure energy conservation in the PT process. Also, different from the original implementation using a cutoff radius for electrostatics, long-range electrostatics was properly taken into account. This implementation allows for the simulation of PT processes in comparatively large systems on long time scales. In this way, PT processes can be efficiently used also in classical MD simulations.

Additionally, the Q-HOP method was applied to study the PT in bulk water and in presence of a glycerol 1-monooleate (GMO) membrane. The obtained proton diffusion coefficient in the bulk is very good agreement to the known experimental value. An almost linear dependency of the proton diffusion coefficient on the system temperature was obtained, in excellent agreement to experiments. In the presence of a membrane, although the proton mobility in the membrane interfacial region is reduced (by as much as 80%), long distance diffusions of protons in the vicinity of the membrane of up to 6–7 nm were observed in the simulations.

6.1 Introduction

Proton transport is one of the fastest and the most abundant chemical reactions occurring in the biological cell. It plays a fundamental role in energy conversion processes such as photosynthesis and cell respiration, and in many other catalytic reactions [348]. In nature, a proton (H^+) is unstable to exist by its own but in most of the time chemically bonded to protonatable species such as water to form an ion. Besides the normal mass diffusion, proton transport is achieved by successive shuffling of the proton from one molecule to another via hydrogen-bonded networks maintained among the molecules. In the course of proton migrations, topological changes are taking place by breaking and forming of covalent bonds of the proton with the donor and the acceptor atom, respectively. This so-called *Grotthuss structural diffusion* [349] is the major transport mechanism contributing to the unusually high mobility of protons in water observed experimentally. Its diffusion coefficient is five times larger than that of cations having similar size (e.g. Na^+) [350].

In liquid water, the excess proton H^+ is solvated by surrounding water molecules to form different complexes. In particular, the two limiting complexes are the Eigen cation (H_9O_4^+) [351] in which the hydronium is located in the center of three water molecules hydrogen-bonded to it; and the Zundel cation (H_5O_2^+) [352] in which the excess proton is equally shared between two water molecules. While contradicting opinions [353–355] exist about which one of the complexes is the dominating one at equilibrium in bulk, it is generally accepted that rapid transition from one complex to the other takes place to achieve the fast proton diffusion supported by both experimental [356, 357] and computational [358–360] studies.

Indeed, the advances in computational techniques have undisputably contributed to the understanding of the proton transport mechanism *per se*, and the behaviour of the excess proton in different biological environments. Computational techniques to study the solvated proton structures and dynamics in biomolecular systems are constantly evolving to improve the accuracy of the underlying model and the efficiency of the method. Major works include the development of the *ab initio* Molecular Dynamics based on the Car–Parrinello method [361] (see [362] for a review), hybrid QM/MM methods [363–365], Warshel’s Empirical Valence Bond method (EVB) [366] and its derivatives (e.g. [367, 368], multi-state EVB models from Voth and co-workers [369–371]), and the semi-empirical Q-HOP method [140, 154, 155, 165]. These methods are different in the sense that different levels of approximation are used.

For example, in *ab initio* MD, forces are derived directly from the electronic structures using a first-principles description based on density functional theory. It is, therefore, deemed to be the most predictive method [362]. However, the extreme computational cost limits the application of this method to rather small systems (a few hundred atoms) and for short simulation times (up to a few hundred picoseconds). For the multi-state EVB model (MS-EVB), the state of a chemical reaction is represented by a linear combination of a number of valence bond states, thus it is able to model a delocalized proton. To this purpose, a multi-dimensional Hamiltonian matrix containing energies of all considered states has to be built and diagonalized to solve the ground state eigenfunction, which in turn is used to calculate forces. Because the potential energy functions used to define the elements in the Hamiltonian, and also the force field parameters are empirically adjusted, their correctness is crucially depending on the reliability of these empirical methods. In addition, the large computational cost connected with the complex MS-EVB procedure currently allows only short simulations of a few nanoseconds. The Q-HOP method, on the other hand, focuses on an approximation for the one-dimensional energy surface for the proton transfer between the donor and the acceptor. The proton transfer probability between donor and acceptor is expressed as a function of the donor-acceptor distance and the environmental electrostatic effect only. The proton transfer probability functions are simple fitted formulas derived from the time-dependent Schrödinger equation and the transition state theory, where the final hopping reaction is determined by a stochastic process. The proton transfer reaction is then simulated as an instantaneous proton shuttle from the donor to the acceptor. In Q-HOP, by neglecting the quantum structural details of the delocalized proton, the computational procedure is greatly simplified. Therefore, this method, when well-integrated into the MD simulation procedure,

will allow the study of proton transfer processes in larger biomolecular systems for longer time scales. Successful applications of the Q-HOP method include the study of protonation equilibria of titratable amino acids and molecules in bulk water [158, 372], the study of proton transport in the green fluorescent protein [156], at the air-water interface [373], inside the Aquaporin water channel [157], and at the pore entrance of proton pumping proteins [374].

The first version of Q-HOP was implemented in ARGOS [159], and later in NWChem [375]. Parameter sets including all titratable amino acids were compiled in previous work [165]. The method allows simulating proton transfer not only in the bulk water but also among protein residues, making Q-HOP suitable for the study of complex biomolecular systems. To this end, we have re-implemented the Q-HOP method into the fast and popular simulation package GROMACS [161]. Taking the advantage of an efficient MD code and a fast parallel processing routine, the new code exhibits a marked increase in performance compared to the existing implementations. To test the validity of the implementation and the predictive power of the Q-HOP method, we have simulated and analyzed long time scale dynamics of the hoppable proton in bulk water and at the membrane interface.

The theoretical background of the Q-HOP method is covered in Section 2.3. Here, the details of our studied systems are given.

6.2 Methods

The Q-HOP implementation in GROMACS [376] was tested by simulating an excess proton (H_3O^+) in a (periodic) box of 1,004 water molecules and one chloride counter-ion. Simulations were performed in a wide range of temperatures, from 240 K to 340 K. The systems were coupled to a Berendsen thermostat [142] using a time constant of 0.1 ps. The pressure was (isotropically) coupled to a pressure bath at 1 bar with a time constant of 1.0 ps using the Berendsen barostat [142]. For the non-bonded interactions, a linear shift function was applied between 1.2 nm and 1.3 nm to allow forces to decay smoothly to zero. Long-range electrostatic interactions were treated with the Particle Mesh Ewald (PME) method [147]. An integration time step of 1 fs was employed for the simulations, and trajectory data were collected every picosecond. The SPC/E (extended simple point charge) water model was used as it was shown to reproduce the structural and dynamic properties of bulk water at ambient conditions [377]. The Lennard-Jones

Table 6.1: Partial atomic charges for the hydrogen and oxygen atoms of the hydronium ion.

Charge set	$q_o(e)$	$q_h(e)$	ref
Palazzo	-0.4167	0.4722	[379]
Voth	-0.5	0.5	[370]
Helms	-0.749	0.583	[140]
SPCE (water)	-0.8476	0.4238	[378]

parameters of the oxygen and hydrogen atoms in the hydronium ion were taken from the SPC/E model [378]. The bond length for O-H was set to 0.1 nm and the angle for HOH to 109.47°. To investigate the influence of the hydronium partial charges on proton diffusion, different previously published charge sets were tested. These include the potentials derived from ion-water pairs by Palazzo and co-workers [379], the potentials based on the Zundel complex and an ion in water clusters by Voth and co-workers [370], and the parameters used in previous Q-HOP simulations [140]. The different hydronium charge sets are summarized in Table 6.1.

The Q-HOP procedure was invoked every 10 fs, which is the minimum duration for a single proton-transfer event [155]. After a successful transfer, the Q-HOP method was disabled for some femtoseconds. This *waiting time* was set to 20 fs in previous Q-HOP studies [140], and corresponds to the approximate transfer time of the proton from the donor to the acceptor. The value depends on the magnitude of the donor-acceptor distance and the relative energy of the hydrogen donor-bound state and the acceptor-bound state. Lill *et al.* [155] estimated the transfer time to 10–40 fs in a strongly hydrogen bonded network. The effect of this transfer time on diffusion was tested for time intervals of 10 to 200 fs, see Fig. 6.1. For time intervals between 20 and 100 fs the mean diffusion coefficient of hydronium was determined to $10 \times 10^{-5} \text{ cm}^2 \text{ s}^{-1}$, close to the experimental value of $9.3 \times 10^{-5} \text{ cm}^2$ [380]. With increasing waiting times the probability for a backward hopping from the acceptor to the original donor molecule significantly decreased as compared to forward hopping (proton hops to a new acceptor). For a short waiting time of 10 fs, more than 80% of the hopping events can be assigned to backward hopping, the mobility of the proton was thus substantially retarded. In contrast, large waiting times (> 100 fs) caused excess reduction on forward hoppings, and led to a decrease in proton diffusion. In conclusion, proton diffusion is insensitive to changes in the waiting time between 20–100 fs. For our simulations, a waiting time of 20 fs was chosen.

Table 6.2: The GAFF atom types and the partial atomic charges for the GMO molecule.

group	atom*	chg [†]	atom	chg	group	atom	chg	atom	charge	
CH ₃	C1 (c3)	-0.07	H (hc)	0.01	CH ₂	C13 (c3)	-0.02	H (hc)	0.00	
CH ₂	C2 (c3)	0.03	H (hc)	0.00		C14 (c3)	-0.01	H (hc)	0.01	
	C3 (c3)	-0.01	H (hc)	0.00		C15 (c3)	0.00	H (hc)	0.01	
	C4 (c3)	-0.01	H (hc)	0.00		C16 (c3)	0.00	H (hc)	0.01	
	C5 (c3)	0.00	H (hc)	0.00		C17 (c3)	-0.12	H (hc)	0.04	
	C6 (c3)	-0.01	H (hc)	0.00		COO	C18 (c)	0.79	O1 (o)	-0.60
	C7 (c3)	0.00	H (hc)	0.01			O2 (os)	-0.44		
	C8 (c3)	0.06	H (hc)	0.03		CH ₂	C19 (c3)	0.01	H (h1)	0.11
CH	C9 (c2)	-0.25	H (ha)	0.13	CHOH	C20 (c3)	0.20	H (h1)	0.08	
	C10 (c2)	-0.25	H (ha)	0.13		O3 (oh)	-0.68	H (ho)	0.43	
CH ₂	C11 (c3)	0.06	H (hc)	0.03	CH ₂	C21 (c3)	0.12	H (h1)	0.05	
	C12 (c3)	0.01	H (hc)	0.01	OH	O4 (oh)	-0.66	H (ho)	0.43	

*See Fig. 6.2 for the atom numberings. GAFF atom types are given in parenthesis.

[†]Atomic charge is in unit e .

Three sets of membrane simulations were performed: a hydrated GMO bilayer with water only, with 200 mM NaCl electrolyte, and with 500 mM NaCl electrolyte.

With the new GAFF parameters, the GMO systems were subject to 200 steps of energy minimization and up to 80 ns of equilibration. Different snapshots from the equilibration trajectories were used as the starting structures for subsequent Q-HOP simulations. The simulation conditions were the same as for the water box, except that surface tension pressure coupling was applied with $\gamma = 22$ dyn/cm per surface, adapted from DOPC lipid bilayer simulations [132]. Coordinates and energies were collected at a frequency of 5 ps^{-1} .

For each electrolytic condition, four separate Q-HOP runs were performed starting from different snapshots of the respective equilibration trajectory or the same snapshot using different start up velocities. The total simulation length for each environment was 115 ns.

It should be pointed out that in membrane simulations with Q-HOP only hoppings between water molecules were taken into account, as experiments and *ab initio* simulations rendered the protonation of lipid headgroups unlikely (personal communication with Peter Pohl and Udo Schmitt).

The self-diffusion coefficient (D) of a molecule can be approximated by the slope of its mass-weighted mean square displacement (MSD) averaged over time using the Einstein relation:

$$D = \frac{1}{2d_f} \lim_{t \rightarrow \infty} \frac{d}{dt} \langle (r(t) - r(0))^2 \rangle \quad (6.1)$$

where d_f is the number of translational degrees of freedom and $r(t)$ is the position of the molecule at time t . Here, block averaging was applied to calculate the average diffusion coefficient and its error bar. For membrane simulations, the lateral diffusion of the hydronium ion as a function of distance to the membrane was analyzed: The simulation box was divided into 20 slabs along the membrane normal (about 5 Å per slab). The slab lateral diffusion $D_{xy}(s)$ considers the lateral displacements of the hydronium ion within the slab windows $[slab_{s-1}, slab_{s+1}]$. The slab MSD curves were fitted in the range of 0.2 to 25 ps.

The dynamics of the hydronium ion in bulk water or in the membrane hydrophilic region can be characterized by the autocorrelation function, $C(t)$, for hydrogen bonds [376]:

$$C(t) = \langle h_i(t_0) h_i(t_0 + t) \rangle \quad (6.2)$$

where $h_i(j) = 1$ if the hydrogen bond of a donor-and-acceptor pair i (e.g. an ion-water pair or an ion-GMO oxygen pair) exists at time j , and $h_i(j) = 0$ otherwise. Note that this function does not require a continuous existence of a hydrogen bond, but allows for the transient breakings and reformings of the bond due to local diffusive and librational motion (so-called *intermittent* hydrogen bonds [381, 382]). Thus, the long-time structural relaxation of hydrogen bonds can be captured in this correlation function. A rough estimate of the hydrogen bond lifetime τ_{HB} can be derived from the integral over $C(t)$.

6.3 Proton diffusion in bulk water

6.3.1 Diffusion

In classical simulations, the calculated diffusion coefficient of the hydronium molecule (D) at 300 K is approximately $1.0 \times 10^{-5} \text{ cm}^2 \text{ s}^{-1}$, almost independent of the applied charge set (triangles in Fig. 6.3). Thus in standard MD simulations the hydronium diffusion is smaller by a factor of 9 as compared to experiment. In contrast, applying the

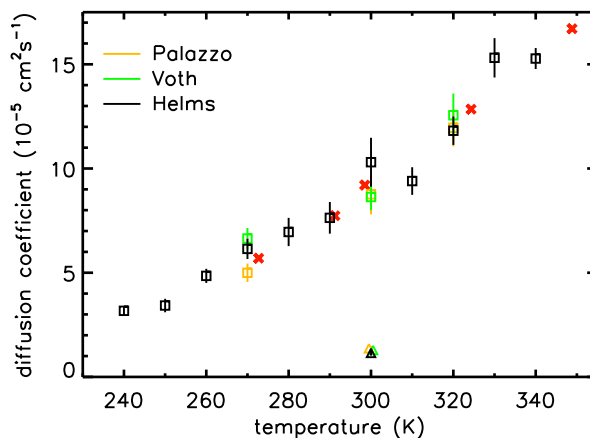


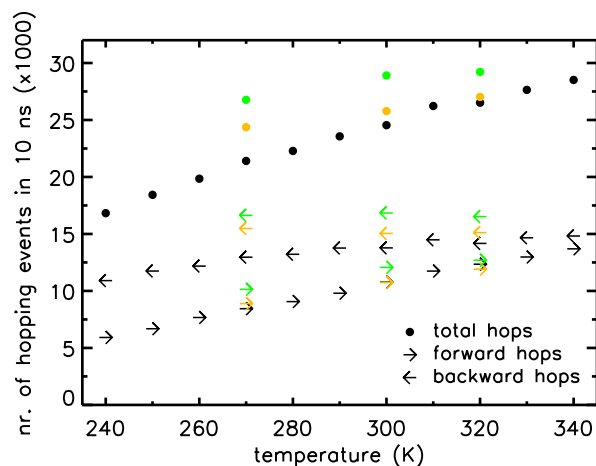
Figure 6.3: Diffusion coefficients (D) of the hydronium ion as a function of the temperature and of the applied hydronium charge set. Results from Q-HOP simulations are labeled with (\square), from classical simulations are labelled with (\triangle), and experimental values of proton diffusion in bulk [383] with red crosses. D was calculated by fitting to the slope of the mean square displacement (MSD) curve in the range of $\Delta t=10 - 100$ ps. The means of ten 1-ns blocks are plotted, standard errors of the means are shown by vertical bars.

Q-HOP procedure, the mean hydronium diffusion coefficient was in the range of $8-10 \times 10^{-5} \text{ cm}^2 \text{ s}^{-1}$, in very good agreement to the experimental value of $9.3 \times 10^{-5} \text{ cm}^2 \text{ s}^{-1}$ [380]. Similar to the classical case, the choice of the hydronium charge set had only a small effect on the diffusion coefficient.

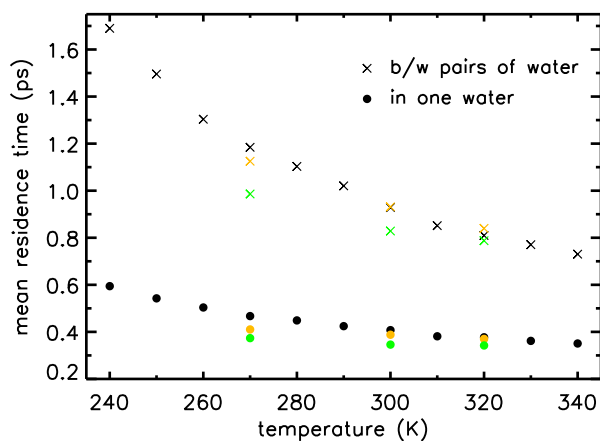
The temperature dependency of proton diffusion was well reproduced by Q-HOP (Fig. 6.3), showing an almost linear increase with temperature. This increase in proton diffusion is caused by an increase in the forward hopping rate (proton hopping to a different water molecule than a previously visited one) with increasing temperature while the number of back hoppings (proton hopping back to the previous donor) increased to a smaller degree (Fig. 6.4). Thereby, the mean residence time of a proton on a water molecule decreased from 0.6 ps at temperature $T = 240$ K to 0.37 ps at $T = 340$ K.

6.3.2 Regimes of the proton transfer reaction

The choice of the regimes which determine the hopping probability is a function of the distance between the oxygens of the donor hydronium molecule and the tentative ac-



(a)



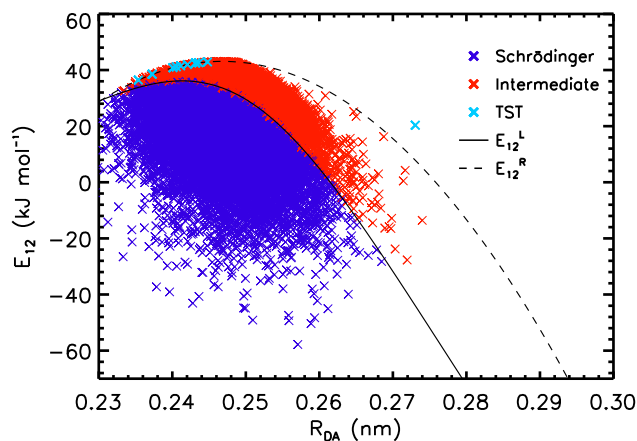
(b)

Figure 6.4: (a) Number of proton hopping events and (b) proton mean residence time in water-box simulations. The same color scheme as in Fig. 6.3 is used here.

ceptor water molecule, R_{DA} , and the relative energy of the proton donor-bound state and the acceptor-bound state, E_{12} . The regimes in proton transfer reactions are depicted in Fig. 6.5 (see also Fig. 2.3 in the Methodology chapter for comparison). The three defined regimes Schrödinger, transition state theory (TST), and intermediate are separated by the validity limits, namely E_{12}^L (solid line) and E_{12}^R (dashed line). In average, about two-third of the hops take place in the Schrödinger regime, one-third in the intermediate regime, and relatively few hops in the TST regime (See Table 6.3). With an increase in

Table 6.3: The distribution of proton transfer reactions taken place in the three defined regimes. Values are given in percentage.

Temperature (K)	Schrödinger (%)	Intermediate (%)	TST (%)
240	66.53	32.57	0.90
250	66.79	32.39	0.82
260	66.80	32.46	0.74
270	67.40	32.12	0.47
280	67.63	31.92	0.45
290	68.41	31.36	0.22
300	69.37	30.58	0.05
310	70.18	29.80	0.02
320	70.02	29.95	0.02
330	71.09	28.87	0.04
340	71.49	28.50	0.01

**Figure 6.5: Regimes of all hopping events from a Q-HOP simulation at 300 K using the Helms charge set.**

system temperature, even a larger percentage of the hopping events were found within the Schrödinger regime. This is a consequence of the decreased energetic difference E_{12} between the donor-bound state and the acceptor-bound state at elevated temperature shown in Fig. 6.6 (left panel). Also shown is the distribution of donor-acceptor distances R_{DA} which was almost invariant to changes in temperature (right panel).

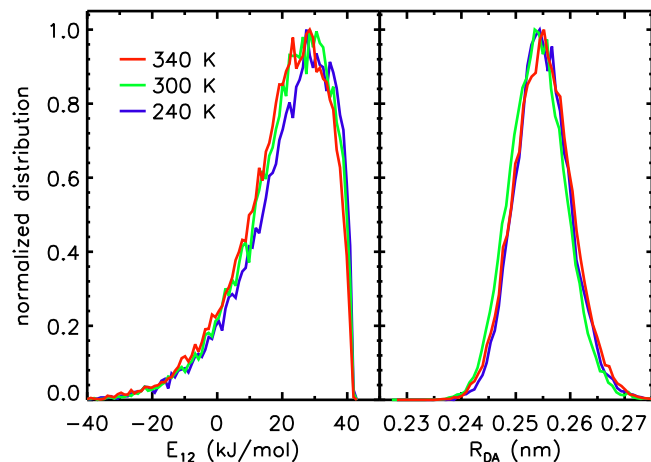


Figure 6.6: Distribution for E_{12} and R_{DA} from proton hopping reactions in Q-HOP simulations using the Helms charge set. For clarity, only three simulations at different temperatures are shown.

6.3.3 Structure of the hydronium solvation shell

Microscopically, the proton transfer reaction initiates a change in the system configuration followed by reorganization of the surrounding water molecules around the protonation site. The distribution of the water molecules in simulations with proton hopping is thus expected to be different from classical simulations. In Fig. 6.7, the radial distribution function $g_{OO}(r)$ (rdf) of water molecules around the hydronium (solid lines) shows that while the location of the first solvation peak remained the same (at ≈ 0.25 nm), the magnitude of the peak in the Q-HOP simulation was significantly reduced and the curve was broadened close to the first minimum. This indicates that the neighboring water molecules of the hydronium were less ordered and more diffusive probably due to the frequent changes in system configuration. Similar first solvation peaks in the range of 0.24–0.26 nm were reported in previous studies using various computational models (see e.g. [369, 384, 385]). The influence of a “hoppable” proton was seen to extend up to the second solvation shell. Integrating $g_{OO}(r)$ yields a coordination number of ≈ 3 . The rdfs for water hydrogen atoms around the hydronium oxygen $g_{OH}(r)$, dashed lines in Fig 6.7, show a broad peak at ≈ 0.32 nm, which can be attributed to a fourth water molecule attracted to the top of the tetrahedral hydronium, in agreement to the experimentally derived rdf from neutron diffraction [386].

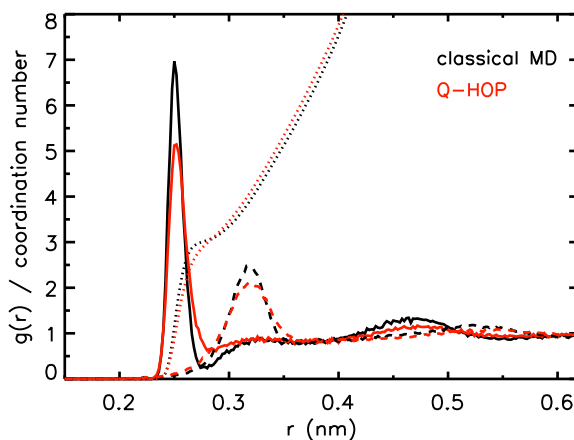


Figure 6.7: The radial distribution function of water oxygen g_{OO} (solid lines) and of water hydrogen g_{OH} (dashed lines) around the hydronium oxygen for the water box simulation in 300 K using the Helms charge set. Also shown are the coordination numbers of water oxygens (dotted lines).

The hydrogen bonded (HB) network centered around the hydronium ion can be quantified by counting the occurrence frequencies of different types of hydrogen bonds defined in [387]. In brief, type D_i indicates that the HB involves a proton donated from a molecule of the solvation shell i (shell 0 is the hydronium molecule itself). Similarly, type A_i is a HB that involves a proton accepted by a molecule in the solvation shell i , except those emanating from the protonated center. Solvation shells are straightly defined by the cutoff distances, while HBs are defined by both an O–O cutoff distance (of 3.25, 3.40, 3.45, 3.50 Å for D/A0 to D/A3, respectively according to [387]) and by the hydrogen-donor-acceptor angle of 30°. From Fig. 6.8, it is seen that the charged hydronium strongly oriented the first shell waters. All three protons of the hydronium were typically hydrogen-bonded to the first shell water molecules (D0), but rarely protons were accepted (A0). HBs from the first shell waters bonding outwards were more relaxed – only about 65% of the waters had two D1 bonds in the Q-HOP model as compared to over 80% in MS-EVB2. First shell waters which are not strongly bonded to the hydronium can fluctuate and network with the other neighboring water as acceptor, as shown by the line A1. Finally the behavior of the third shell waters were observed to already display bulk-like properties.

The comparison of the solvation structure of the hydronium obtained from Q-HOP

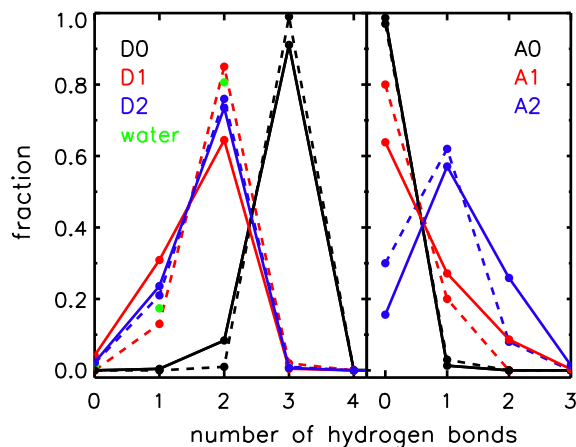


Figure 6.8: Distribution of the hydrogen bond types of hydronium and water molecules in the 0/1/2-solvation shell centered around the hydronium at 300 K. Results from Q-HOP simulation with Helms charge-set are in *solid* lines, whereas those from [387] are in *dashed* lines. The green bullets show the distribution for bulk water.

simulation to the one from MS-EVB2 model by Markovitch *et al.* (*dashed* lines in Fig. 6.8) shows that although structures from the two models are fairly similar, the interchange of the bonding pattern in D1 and A1 indicates a disturbed first solvation shell in Q-HOP. This is due to the essential rearrangement of the shell waters after spontaneous hopping in Q-HOP. A small difference may also arise due to the use of different water models (SPC/E vs. TIP3P in MS-EVB2). A difference in the water structure between the classical hydronium simulation and the MS-EVB2 results is seen mainly for A1 and A2 bonds (difference for A1 is 0.21, A2 is 0.39).

6.4 Proton diffusion at the membrane-water interface

Proton diffusion in the presence of a membrane-water interface was studied on fully hydrated GMO lipid bilayer systems. As shown in Table 6.4, three systems with differing in their salt concentrations were simulated: NaCl 0 mM, 200 mM, and 500 mM. For each system, four separate runs of different lengths were performed, summing up to a total of 115 ns Q-HOP simulation for each system. The average area per lipid for the three systems varied between 38 \AA^2 and 39 \AA^2 , which is in very good agreement to the known experimental value of 38.6 \AA^2 [388].

Table 6.4: Average area per lipid (in \AA^2) of GMO bilayers in Q-HOP membrane simulations at 310 K.

simulation	sim 1 10 ns	sim 2 25 ns	sim 3 40 ns	sim 4 40 ns	block average
NaCl 0 mM	39.7	38.6	39.1	38.3	38.8 ± 0.2
NaCl 200 mM	39.4	39.1	39.6	39.0	39.3 ± 0.2
NaCl 500 mM	39.0	38.9	38.6	38.5	38.7 ± 0.2

The last column gives the block average (10 ns blocks) and standard error calculated from all simulation runs. The initial snapshots for sim 1–4 were taken from the corresponding equilibration trajectories at 20, 60, and 80 ns respectively, where sim 2 and sim 3 ran with newly assigned velocities.

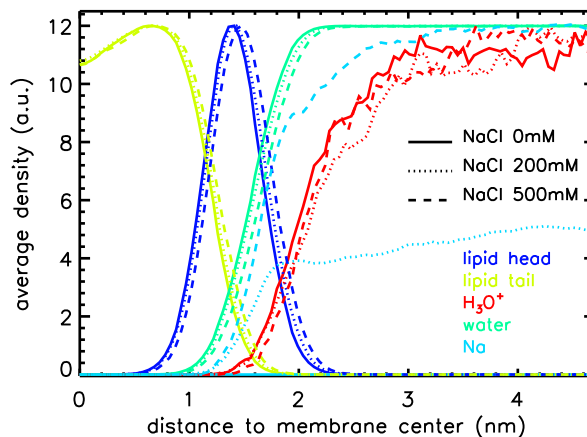


Figure 6.9: The average densities of different groups as a function of the distance to the membrane center. Simulations of different ionic concentrations are shown with different line types. Density curves are normalized for clarity, except for the sodium curves.

In the GMO membrane systems, the hydronium ion traveled rapidly from the membrane interface to the bulk, and then back to the membrane. No preferential deposition of the hydronium in the membrane was observed regardless of the ionic concentrations (see Fig. 6.10). In all cases, the outer hydrophilic region of the membrane which has an increased water accessibility, was more frequently visited by the hydronium.

Table 6.5: The diffusion coefficient of the hydronium ion in GMO systems and in the water box systems.

	D_{3d}^{GMO}	D_{xy}^{GMO}	D_z^{GMO}	D_{3d}^{waterbox}
NaCl 0 mM	10.32 ± 0.25	11.45 ± 0.25	8.07 ± 0.45	10.03 ± 0.34
NaCl 200 mM	9.11 ± 0.27	10.18 ± 0.36	7.20 ± 0.23	9.54 ± 0.41
NaCl 500 mM	8.17 ± 0.16	8.92 ± 0.24	6.69 ± 0.26	8.77 ± 0.36

The diffusion coefficient D is obtained by fitting the MSD curve in the range of 10–100 ps applying the block averaging procedure (10 ns per block). The value in the table has the unit of $10^{-5} \text{cm}^2 \text{s}^{-1}$. The subscript $3d$ indicates that the diffusion is three dimensional, xy is lateral diffusion in the direction of the membrane plane, and z is the one-dimensional diffusion along the membrane normal.

6.4.1 Proton mobility

In the presence of the GMO membrane, the hydronium ion was observed to diffuse non-isotropically, i.e. it moved faster in the direction of the membrane plane than in the direction of the membrane normal. As shown in Table 6.5, although the three-dimensional diffusion coefficients of the hydronium ion in GMO systems were similar to those in pure water, the diffusion of the hydronium in the direction of the membrane plane was slightly enhanced whereas the diffusion in the direction of the membrane normal was slightly suppressed, regardless of the salt concentrations.

The lateral diffusion of water molecules was shown to be slowed down in the DOPC membrane-water interfacial region [132]. A similar reduction in hydronium diffusion was also observed in GMO systems. By using sliding windows of about 15 Å in thickness along the membrane normal, the slab lateral diffusion of hydronium as a function of the distance to the membrane was analyzed. As shown in Fig 6.10, the hydronium mobility was drastically reduced when approaching the membrane. In the hydrophilic lipid headgroup region (indicated with pink color in the figure), the hydronium diffusion was decreased by at least 80% with respect to that in the bulk. The forward hopping rate of protons (1.21 hops/ps) was similar to the one in bulk (1.19 hops/ps); however, the backward hopping rate was increased by 13%.

Microscopically, the hydronium ions were seen to move rapidly in the water phase and make frequent visits to the membrane hydrophilic region. Four oxygen-containing groups in the GMO lipids are the potential hydronium attractors: the ester oxygens O1 and O2, and the hydroxyl oxygens O3 and O4. The hydroxyl groups are in the outermost

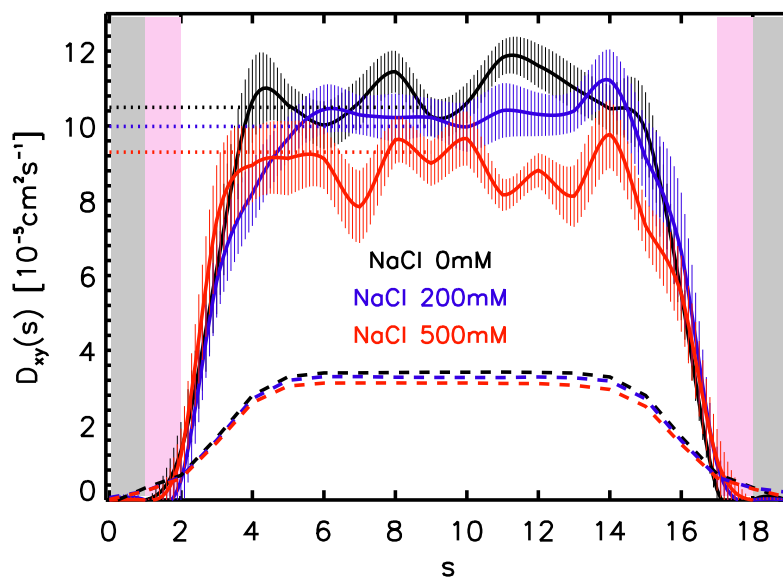


Figure 6.10: The slab lateral diffusion coefficients of the hydronium ion (solid lines, smoothed) and water (dashed lines) in the GMO simulations. The $D_{xy}(s)$ values were obtained by fitting the MSD curve in the range of 0.2–25 ps (hydronium) and 1–25 ps (water), where the MSD considers displacement of the molecule within the slab windows $[slab_{s-1}, slab_{s+1}]$. The pink area indicates the GMO headgroup region, and the grey area the carbon tail region. The hydronium lateral diffusion in the bulk are also shown as reference (dotted lines).

part of the hydrophilic region, thus they are fully hydrated in the bulk water; whereas the ester groups adjoining the hydrophobic core are less accessible to water. Both the water accessibility of the lipid atoms and the local electrostatic potential influence the spatial preference of the hydronium. It is seen from Fig. 6.11 that the ion stayed most of the time in the bulk, i.e. at least two hydration shells away from any lipid oxygens. At the same time, ion shuttlings between lipid atoms frequently occurred. A round-trip travel of the hydronium (that goes from the bulk to the membrane, and then back to the bulk) was as short as 0.4 ps. In the membrane simulations without salt, the mean time for a round-trip travel reaching to the surface hydroxyl groups was 2.5 (O3) and 1.1 (O4) ps, whereas it was 5.3 (O1) and 3.6 (O2) ps for the less hydrated ester oxygens. Also long term burial of the hydronium ion in the membrane of up to 50 ps was rarely observed.

During each round-trip travel of the hydronium into the membrane, the hydronium ion diffused for some distance before returning to the bulk. The lateral distance

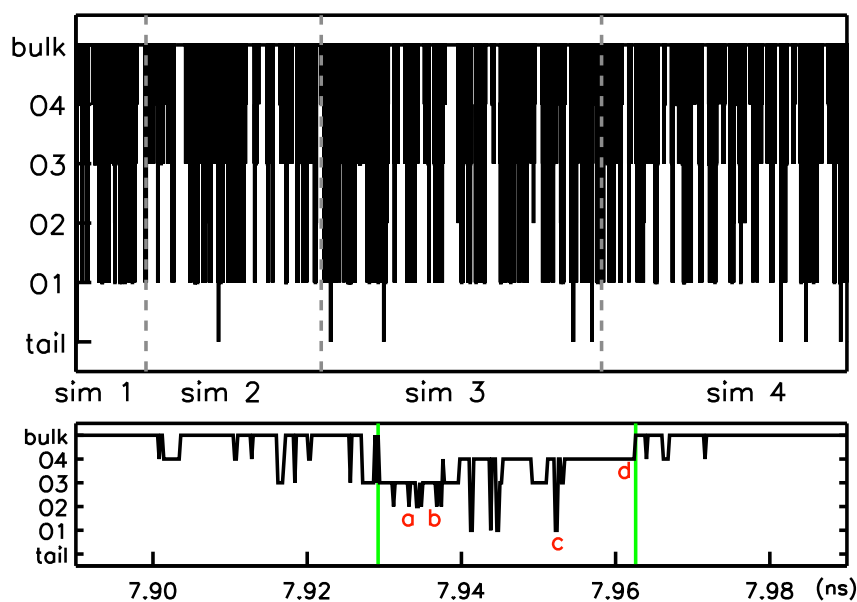


Figure 6.11: (top) Travelling of the hydronium ion from the bulk to the membrane and back in GMO simulations (NaCl 0mM). The ordinate indicates the presence of the ion either close to the headgroup atoms O1–O4 (distance < 0.6 nm), or in close contact with the membrane (< 0.4 nm to lipid tail atoms), or in the bulk. Note that four trajectories were concatenated in this plot, so the total time length is 115 ns. (bottom) Close-up of the ion travelling behaviour for 100 ps from sim 2. In total, 14 hydronium round-trips to the membrane were recorded. Within this period, the longest round-trip travel was 33.4 ps, from 7929.2 ps to 7962.6 ps (enclosed with green bars) for a lateral distance of 1.9 nm. Snapshots of the hydronium diffusion on the membrane surface are depicted in Fig. 6.12, and the trajectories taken for the images are indicated here with letters a–d.

between the point of entry into (or close to) the membrane and the point of exit followed an approximate Gaussian distribution. As shown in Fig. 6.13, the distance distributions for round-trips reaching the deeper esters O1 and O2 are broad, i.e. the hydronium travelled larger distances in the membrane than for round-trips reaching only the surface O3 and O4 groups. About 50 instances of long distance diffusions of 1–2 nm were observed within 115 ns of Q-HOP simulation.

It is known that in the presence of salts, the Grotthus mechanism is suppressed and the proton diffusion is decreased [389]. Indeed, our results show that the influence of salts on hydronium diffusion is significant. At moderate to high salt concentrations, hydronium diffusion was decreased by 5–13% in bulk water, whereas it was reduced

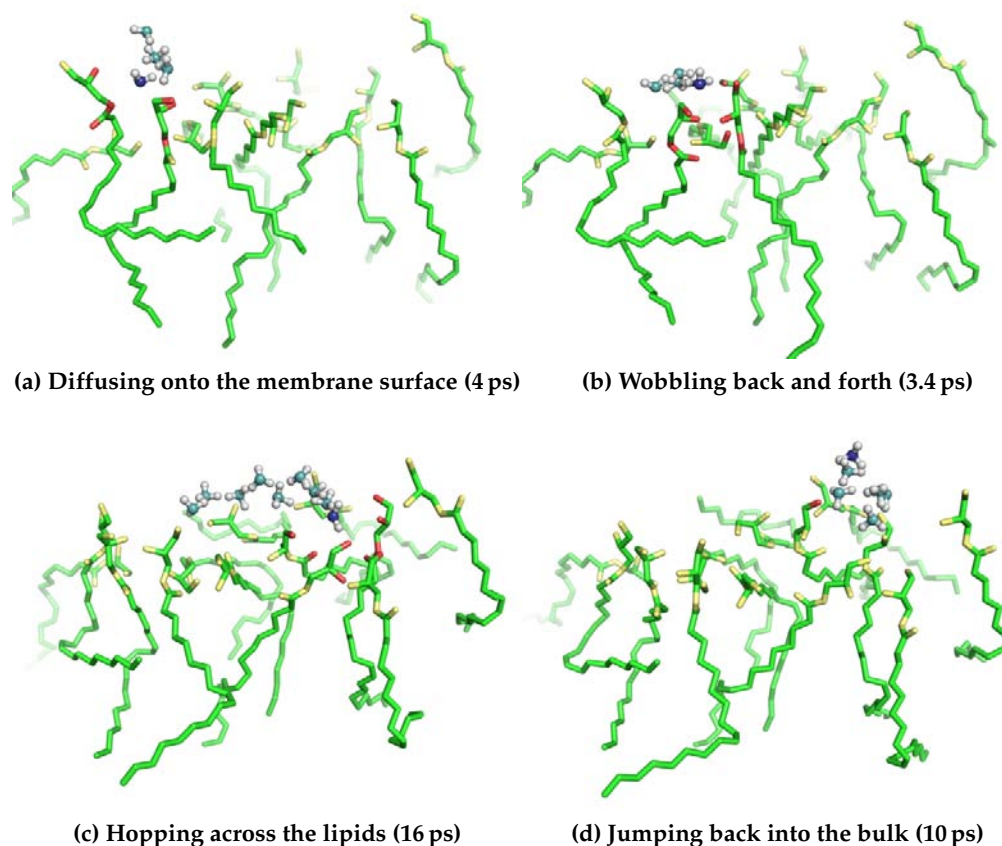


Figure 6.12: Snapshots of the 1.9-nm hydronium diffusion along the membrane surface observed in sim 2 within a time window of 33.4 ps. Hydronium ions are drawn in light blue, and the ones of the final frames in the shown trajectories are drawn in deep blue (see the letter a–d in Fig. 6.11). GMO oxygens within 0.6 nm of the deep blue hydronium are indicated in red. In total, the hydronium ion hopped 81 times and ran across the headgroups of 13 GMO lipids.

further by 5–7% in the presence of GMO membranes. As shown in Fig. 6.14, the mean residence time of the excess proton on a water molecule was only slightly affected in the presence of salts (colored ●), however, the localization of proton between water pairs was increased (colored ×). The computed forward hopping rates of the proton in the membrane interfacial region were reduced by 7% and 12% for systems at 200 mM and 500 mM NaCl, respectively, while in bulk water the reduction was 5% and 9%.

Interestingly, in the membrane region the presence of salts affected the proton diffusion differently in the inner hydrophilic region and the outer hydrophilic region. The round-trip travel time of hydronium reaching O1 was increased from 5.3 ps to 5.6 ps in

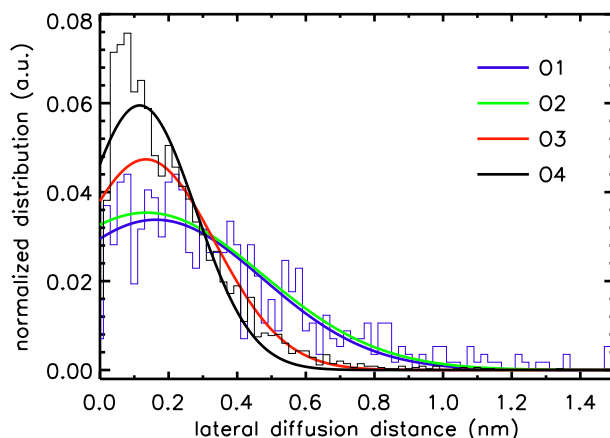


Figure 6.13: The normalized distributions of the lateral distance between the point of entry and the point of exit of the hydronium round-trip travels in the membrane (without salt). The mean μ and the standard deviation σ of the fitted gaussians are (O1) 0.16 ± 0.31 , (O2) 0.14 ± 0.34 , (O3) 0.13 ± 0.20 , (O4) 0.12 ± 0.16 . For reference, two original histograms (O1 and O4) are shown in thinner lines.

200 mM and to 5.8 ps in 500 mM NaCl. Also for reaching O2, the travel time was increased from 3.6 ps to 4.2 ps for both salt concentrations. No salt-dependency was observed for round-trips to strongly hydrated O3 and O4 atoms. Thus, the results show an increased residence time for hydronium close to the hydrophobic tail region of the GMO bilayer in the presence of NaCl.

So far, we described the diffusion behaviour of the excess proton within and in close vicinity (< 0.6 nm) of the membrane. With this small cutoff, the lateral distance that the hydronium can travel is short, typically within 2 nm. However, it is not clear to which cutoff distance the hydronium diffusion is affected by the existence of the membrane, and how it compares to bulk water. To answer these questions, we calculated the lateral diffusion distance distributions using cutoffs ranging from 0.3 nm to 2.3 nm (note that 2.5 nm is half the thickness of the water slab), and compared the distributions to the case of a pure water box. The results are shown in Fig. 6.15: For small cutoffs of < 0.8 nm, the distance distributions of the membrane system and water box were similar. For cutoffs > 0.9 nm, the lateral distances travelled by the hydronium in membrane system are significantly increased with respect to the distances in a pure water box, visualized as long tails in the distributions. While bulk-like behaviour was not yet observed for a cutoff of

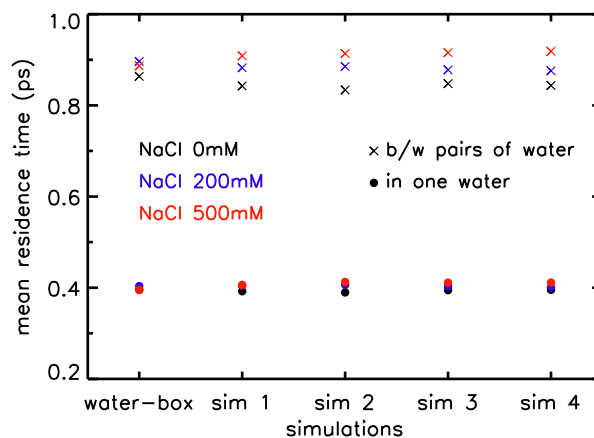


Figure 6.14: Comparison of the mean residence time of the excess proton with a water molecule or between a pair of water molecules. The former can be seen as the mean life time of the hydronium ion. Shown are results for the pure water box simulations as well as for the GMO simulations.

2.3 nm, a simulation system with an increased water layer thickness would be needed to evaluate the maximum distance from the membrane within which the membrane is still influential. Nevertheless, it is shown that the lateral proton diffusion close to surfaces is significantly enhanced.

6.4.2 Proton solvation in the membrane

In the hydrophilic region of the GMO bilayer, the hydration of the GMO oxygens as analyzed from the radial distribution functions (data not shown) followed the sequence $O4 > O3 > O1 > O2$ with 2, 1.7, 0.7, and 0.2 water molecules in the first solvation shell, respectively. Similarly, the hydronium ion which made also frequent visits to the GMO bilayer had contacts with the headgroup oxygens following the same sequence. As shown in Fig. 6.16, the hydronium radial distribution functions involving the GMO hydroxyl oxygens $O3$ and $O4$ exhibit pronounced peaks at 0.26 nm, but for the esters $O1$ and $O2$ only a small or no peak were found. For the former, the first peak is at the same distance as the first peak of the corresponding rdf of water. This demonstrates that the hydronium ion succeeds in penetrating into the first solvation shell of the GMO hydroxyl oxygens distributed in the outer hydrophilic region of the membrane.

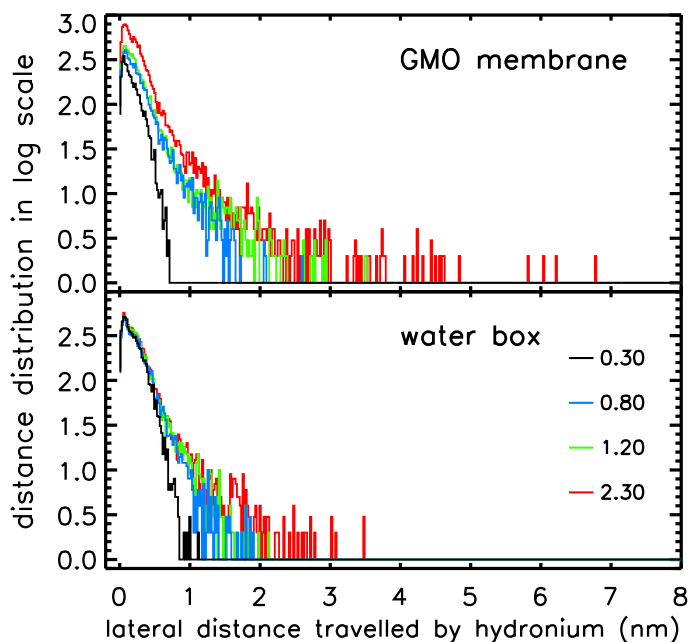


Figure 6.15: The distribution of the lateral distance travelled by the hydronium in the GMO system (parallel to the membrane surface) and in the pure water box. The distance is defined as the lateral distance from the point of entry into the membrane (within a cutoff from the membrane) to the point of exit of the hydronium. For the water box system, an imaginary plane at different z coordinates was defined for the cutoff calculation. Here, different cutoffs were used and indicated with different colors in the plots. Note that the water slab thickness of the membrane system is about 5 nm. Considering the periodic boundary conditions and the fluctuation of the system size, results for cutoffs beyond 2.3 nm were not considered.

The hydronium ion forms hydrogen bonds with the lipid headgroup atoms. The dynamics of the hydronium ion in the membrane may be characterized by the hydrogen bond time correlation function, $C(t)$. The existence of a hydrogen bond is defined using geometric criteria with a donor-acceptor cutoff distance of 0.35 nm and a hydrogen-donor-acceptor angle of $< 30^\circ$. Only for 0.35% of the total simulation time (115 ns) a hydrogen bond is found between the hydronium and a lipid. It is therefore statistically insufficient to calculate a smooth correlation curve and the hydrogen bond lifetime τ_{HB} . But still, $C(t)$ may be used to obtain the trend of the structural relaxation of the hydronium in the membrane region.

The hydronium formed hydrogen bonds mostly with the hydroxyl groups in the outer hydrophilic region of the bilayer (see also rdf, Fig. 6.16), with the hydronium ion acting as donor. 56% of all hydrogen bonds to GMO lipids were formed to the O4 hy-

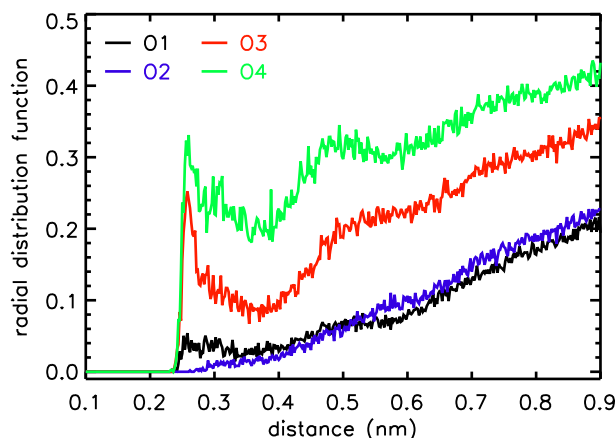


Figure 6.16: The radial distribution function of the GMO oxygens around the hydronium oxygen.

droxyl group, about 38% to the O3 hydroxyl group, and less than 6% to the carbonyl O1. As the O2 atom has exceedingly low water accessibility and possesses a smaller partial charge as compared to other GMO oxygens, the potential to interact with the hydronium is expected to be very small (0.7% of hydronium hydrogen bonds to O2). Therefore, the following correlation analysis is focused on the hydrogen bonds with O1, O3, and O4.

Fig. 6.17 shows the structural relaxations of the hydronium hydrogen bond with different lipid oxygen groups. In all cases the hydronium-lipid hydrogen bond relaxation times were smaller than those for hydrogen bonds to bulk water molecule. The lifetime τ_{HB} to water is 2.20 ps while it is 20% smaller for hydronium-lipid oxygen hydrogen bonds (τ_{HB} =1.69 ps, 1.95 ps and 1.70 ps for O1, O3 and O4, respectively).

Notably, the rates of water relaxations in the bilayer (see the inset) are found to be distinctly related to the locations of the oxygen groups in the bilayer – the deeper it is to the hydrophobic core, the slower the decay of the correlation function, and vice versa. A similar behavior was observed for the distance time correlation of charged Na^+ ions to GMO oxygens in 200 mM electrolyte (data not shown). This behavior is probably due to a faster exchange of water molecules on the surface of the GMO bilayer.

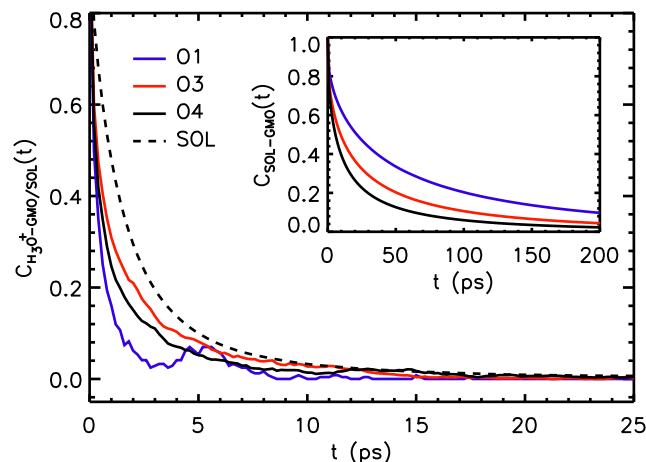


Figure 6.17: The autocorrelation function of hydrogen bonds between the hydronium ion and the lipid polar headgroups involving the oxygens O1, O3, and O4 in Q-HOP membrane simulations. The dashed line gives the reference hydrogen bond relaxation of the hydronium as calculated for the pure waterbox simulation. For comparison, the hydrogen bond time correlation between GMO atoms and water in the classical simulation is displayed in the inset.

6.5 Conclusion and future work

In this work, we have re-implemented the Q-HOP method into the simulation package GROMACS. Q-HOP is an efficient but approximate technique to simulate proton transfer reactions in biomolecular systems. It is approximate meaning that structural details of the proton particle at quantum level are neglected. Nevertheless, in Q-HOP, the Grotthuss mechanism is simulated by instantaneous hopping of a proton from the donor to the acceptor molecule depending on the donor-acceptor distance and Coulombic environmental effects. The current implementation as well as the method itself was evaluated rigorously by long simulations of hydronium ions in bulk water (in total 200 ns) and in the presence of bilayer membranes (in total 345 ns), a time scale which could not be addressed by previous implementations.

It was shown that with the Q-HOP method the proton diffusion coefficient at room temperature could be reproduced quantitatively to the known experimental value, confirming previous Q-HOP simulation studies [140]. In addition, an almost linear dependency of the proton diffusion coefficient on system temperatures from 240 K to 340 K was obtained, in excellent agreement with the experimental observations [383].

In Q-HOP simulations, the direction of proton hopping is not always linear and one-directional (as in most schematic drawings of the Grotthuss mechanism); instead, the proton hops quickly back and forth between water pairs before hopping to a new close-by water molecule. At room temperature, the mean residence time of a proton on one water molecule and between water pairs are 0.4 ps and 0.9 ps respectively. Additionally, the radial distribution function and the hydrogen-bonded structure of the hydronium in bulk water were investigated. Our results show that both the proton solvation structure and dynamics are in reasonable agreement to the observations from experiment and the more realistic albeit very slow MS-EVB model.

The proton mobility in the presence of a membrane interface was found to be markedly different from that in bulk water. Our results have shown that although the membrane slows down the diffusion of a proton in its vicinity as much as 80% to that in the bulk, a proton may laterally travel along the membrane surface for larger distances. Long distance proton travels in the vicinity of the membrane of up to 6–7 nm were observed. Unlike water molecules being tightly captured in the membrane hydrophilic region (exhibited by slow hydrogen bond relaxation rate), protons rapidly escape from the bound lipids, and hop to neighboring lipids via bridging waters or retract back to the bulk. This observation of long distance migration of protons along the membrane surface is in agreement with experiments [390, 391]: Protons released by the integral membrane protein Bacteriorhodopsin to the extracellular side of the purple membrane were detected by fluorescein dyes attached in the cytoplasmic side. As the detection of protons in the bulk is much delayed (0.8–1 ms longer), the existence of long range diffusion of protons along the membrane surface is well justified. In the presence of salt, the diffusion of protons was decreased. In particular, longer detainment of the hydronium was observed in the inner hydrophilic region, as compared to the salt-free condition.

In conclusion, the use of the Q-HOP method in studying proton transfer in biomolecular systems is fruitful, as demonstrated by the previous work [157, 158, 372–374] and presented here by our water and membrane results. As many interesting biochemical phenomena take place in the regime of long time scales, fast and efficient methods allowing the study of these systems are desirable. Future work will mainly focus on the inclusion of proton hopping to titratable amino acids and investigate the effects of different membrane compositions, also including membrane proteins, on proton diffusion.

Acknowledgements

This work is the result of a close collaboration between the Department of Theoretical and Computational Biophysics of the MPI for Biophysical Chemistry, Göttingen and the Theoretical and Computational Membrane Biology, Saarland University. In particular, thanks are giving to G. Groenhof, B. de Groot and H. Grubmüller for their efforts and supports in implementation and in many contributing discussions. We also knowledge the help from W. Gu and V. Helms for the Q-HOP code discussions, and our master student M. Moritz for her work in the initial code. We thank Robert Vacha from the Academy of Sciences of Czech Republic for helping the conversion of topology file needed in the lipid force field development.

Shirley W. I. Siu was supported by the Deutsche Forschungsgemeinschaft (Graduate School *Structure Formation and Transport in Complex Systems*, No. 1276/1). As a member of the Center for Bioinformatics, Rainer A. Böckmann was supported by the Deutsche Forschungsgemeinschaft Grant BIZ 4/1.

Author Contributions:

Rainer A. Böckmann and Bert de Groot designed research. The Q-HOP code in GROMACS was implemented by Gerrit Groenhof and Weng In Siu. Testing of the initial code was done by Mareike Moritz in her master thesis, and testing of the final code was done by Weng In Siu. The GAFF lipid force field was parameterized by Weng In Siu. Simulations were set up and analyzed by Weng In Siu.

Summary & Conclusions

Biological transport is the key to maintain the living of the cell. It is ubiquitous and involves ions and molecules of different sizes that are exchanged across the cell interior and exterior, and between the cell compartments [1]. To understand such transport processes, three fundamental questions need to be answered: What are the *mechanisms* of transport along and across the boundary? What are the *factors* affecting these processes? And how do the required substances arrive at the right place (*supply*) in the cell where the exchange takes place?

In this thesis, we tried to shed some light on selected topics along this line by means of molecular dynamics simulations. In particular, we investigated the influence of proteins on the stability of membranes in electric fields [260], important e.g. for the rate of spontaneous membrane pore formation [105]. Apart from its probable biological role e.g. in ion transport, electropore formation by externally applied fields is widely used for the delivery of drugs into cells [167], in electrofusion [180, 392], or for the site-specific delivery of drugs for the treatment of skin cancer [168, 169]. Another focus of our work [25] was on the influence of the environment – in particular of lipids – on the transport of ions through the simple ion channel gramicidin [192]. However, current force fields for MD simulations can only be used with great care in combined studies of both phospholipids and proteins or drugs as their development for different molecular species typically followed separate lines. Thereby, the validity of their combination in studies on mixed membrane-protein systems may be questioned [129]. As a first step to solve this discrepancy, we reported the development of a consistent force field for phospholipids based on the generalized AMBER force field [132]. While the classical MD method is

sufficient to simulate the interactions of proteins and lipids, the simulation of transport processes such as proton transfer that involves chemical bond breaking and formation is not possible. To this end, the quasi-classical Q-HOP method [140] was improved and re-implemented in a fast simulation package. In this way, the long time scale diffusion of protons in bulk water and in the presence of a membrane interface could be studied.

From our studies on gramicidin-DMPC systems (Chapters 3 and 4), two important factors affecting the ion conduction through gramicidin channels were observed: the conformation of the channel and the nearby lipid and water environment. Simulations of the two experimentally determined main conformations of gramicidin with and without applied external electric fields revealed that the so-called “non-channel” conformation of gramicidin (DH) [209, 236] has both higher rates for water and for ion permeation as compared to the “channel” conformation (HD) [237, 238]. For the former, the free energy barrier of ion permeation was significantly decreased by ≈ 25 kJ/mol with respect to the “channel” conformation. While the energetically favorable environment for ion permeation inside the channel is crucially dependent on the organization of the atoms lining the channel interior (in particular the carbonyl oxygens of the protein backbone), the stabilization of a potassium ion at the pore entrance is determined mainly by the surrounding lipids and their hydration shells. It was shown that lipid-ion interactions stabilize potassium at the channel entrance with a favorable enthalpic contribution of ≈ -180 kJ/mol in DH with respect to HD while this type of interaction is sterically largely hindered in HD. Our results suggest that a different lipid species may not only affect the preferred gramicidin conformation but also the strength of the lipid-cation interaction at the channel entrances.

Beside the transport through pore-like channels, non-protein regulated transport through momentarily formed electropores can occur [180]. The formation of electropores is strongly coupled to the transmembrane potential [392] and also to the composition of membranes. In the study of gramicidin-DMPC systems with applied external electric fields (Chapter 3), the gramicidin as a membrane protein was observed to have a significant effect on the pore formation rate. When embedded in the bilayer, gramicidin enhanced the membrane stability by increasing the lipid chain order and the membrane thickness. Even this small transmembrane protein effectively decreased the probability of forming a closed water file across the membrane as the initial step of electropore formation.

Unlike the transport across membranes which occurs in a localized region of the cell, transport processes to specific sites are even more challenging due to increased time- and length-scales. In this thesis, we have chosen to study the proton transport in bulk water and close to a membrane surface due to its biological importance (Chapter 6). By the use of the semi-empirical Q-HOP method [140] and our improved re-implementation in a fast simulation packages [161], long simulations on the submicrosecond time scale were feasible. Our results revealed that proton transport in the bulk water is a random walk, whereas in the presence of a membrane surface, the proton mobility is laterally increased with respect to that in the bulk. Although the proton diffusion in the vicinity of membranes is significantly reduced, protons may laterally diffuse along membrane surfaces for large distances. On biological membranes, this surface diffusion may even be further enhanced as shown in experiments [390, 391]. It may be speculated that this fast 2-dimensional diffusion of protons on the confined surface of cells or organelles greatly simplifies the supply of ion/proton-pumps with protons with respect to 3D diffusion of protons e.g. in the cytoplasm.

Both proteins and lipid membranes play a fundamental role in all biomolecular transport processes. Thus, the predictive power of computational studies involving proteins and membranes crucially depends on the underlying force fields and the combination of the lipid and protein force fields [129]. To this end, we developed a lipid force field for DOPC and for GMO molecules based on the general AMBER force field [130] that was parameterized consistently for proteins, DNA and other organic molecules (Chapter 5). Our new lipid force field showed improved structural properties of DOPC membranes as compared to existing popular lipid force fields. Although different lipid force fields displayed similar macroscopic properties, the molecular details like the hydration of lipid head groups differed significantly.

In the following we will briefly outline current and relevant future directions for the characterization of biological transport processes on the molecular level involving method development, application studies, and necessary further force field development.

Regarding computer simulations of biomolecular transport processes, on the one hand, the length scale and the time scale of the studied processes will be further ex-

tended to approach macroscopic level. To this end, coarse-grained models [98, 138] which were available only since a few years will likely be one method of choice. Similar to the atomic force field, coarse-grained models demand a vast amount of time and effort in development and in validation, the baseline for acceptance will be their abilities to produce results complying with experiments and atomistic models qualitatively and semi-quantitatively. On the other hand, the intricate details involved in molecular transport mechanisms win importance not least because of the quickly growing interest in the design of new proteins within the emerging field of synthetic biology. Methods which combine the accuracy of *ab initio* methods [362] and the efficiency of classical methods yield a level of detail which cannot be provided by either of them alone. In this respect, the various hybrid models (QM/MM models [365, 393]) serve as good starting points. The focus of these models will probably be in solving the boundary problems inherent in the mixing of systems of different scales described by different approximations. The success of the Q-HOP method in studying proton diffusion prompts us for continuing in extending the model to other titratable molecules within the framework of the GRO-MACS program package [161].

For simulation applications, as more experimental structures of membrane proteins are going to be uncovered, studies of the often sophisticated transport mechanisms of large and complex channels are compelling. Our current work along this line includes the study of the voltage-gated potassium channel (Kv) [394] and the calcium ATPase channels [395]. For the latter, crystal conformations at different stages of the transport process together with intermediate conformations sampled by MD simulations are expected to yield a complete picture of the transport mechanism.

As the predictive power of computational methods, in particular of MD simulations, relies largely on the computational models and the underlying force fields, the development of consistent force fields for lipids, proteins, and other organic molecules will continue to be an important and indispensable focus of current research. In addition, consideration of polarization effects [139], which were observed to be prominent at the hydrophobic-water interface, will gain considerable importance with further increasing computational power and increasing demands on the predictive power of MD methods. Current simulations of membranes mostly involve single homogenous lipid bilayers. However, the influence of the membrane composition with various biochemically relevant lipids and membrane-anchored molecules on transport processes is receiving

great attention. Model membranes mimicking more physiological biomembranes will be a basic requirement for realistic studies of transport processes. Besides the developed general AMBER force field for DOPC, we are currently working on the development of force fields for other phospholipids such as DMPC, POPC, and anionic lipids such as POPG and POPS, which are known to have a significant influence on the function of membrane proteins. Finally, currently modeled systems including several finite bilayers will for the first time allow unbiased studies on membrane fusion and fission [396].

Bibliography

1. Berg, J. M., J. L. Tymoczko, and L. Stryer, 2002. *Biochemistry* (5th ed.). Freeman.
2. Sumida, C., R. Graber, and E. Nunez, 1993. *Prostaglandins Leukotrienes and Essential Fatty Acids* 48:117–122.
3. Cho, W., and R. V. Stahelin, 2005. *Ann. Rev. Biophys. Biomol. Struct.* 34:119–151.
4. Petty, H. R., 1993. *Molecular Biology of Membranes*. Springer, New York.
5. Hofacker, I., and K. Schulten, 1998. *PROTEINS: Struct., Func. & Bioinf.* 30:100–107.
6. Kandt, C., K. Gerwert, and J. Schlitter, 2005. *PROTEINS: Struct., Func. & Bioinf.* 58:528–537.
7. Herce, H. D., and A. E. Garcia, 2007. *Proc. Natl. Acad. Sci. USA* 104:20805–20810.
8. Haberl, F., O. Othersen, U. Seidel, H. Lanig, and T. Clark, 2007. Investigating Protein-Protein and Protein-Ligand Interactions by Molecular Dynamics Simulations. *In High Performance Computing in Science and Engineering*, Springer, 153–164.
9. Ahmad, M., W. Gu, and V. Helms, 2008. *Angew. Chem. Int. Ed. Engl.* 47:7626–7630.
10. Villa, A., J. Wöhnert, and G. Stock, 2009. *Nucleic Acids Res.* 2009:1–13.
11. Nishihara, Y., S. Hayashi, and S. Kato, 2008. *Chem. Phys. Lett.* 464:220–225.
12. Gnanakaran, S., H. Nymeyer, J. Portman, K. Y. Sanbonmatsu, and A. E. Garcia, 2003. *Curr. Opin. Struct. Biol.* 13:168–74.
13. Swope, W. C., and J. W. Pitera, 2004. *J. Phys. Chem. B* 108:6571–6581.
14. Swope, W. C., and J. W. Pitera, 2004. *J. Phys. Chem. B* 108:6582–6594.
15. Scheraga, H. A., M. Khalili, and A. Liwo, 2007. *Ann. Rev. Phys. Chem.* 58:57–83.
16. Okazaki, K. I., N. Koga, S. Takada, J. N. Onuchic, and P. G. Wolynes, 2006. *Proc. Natl. Acad. Sci. USA* 103:11844–11849.
17. Affentranger, R., I. Tavernelli, and I. E. Di, 2006. *J. Chem. Theory and Comput.* 2:217–228.
18. Zhang, J., C. Li, K. Chen, W. Zhu, X. Shen, and H. Jiang, 2006. *Proc. Natl. Acad. Sci. USA* 103:13368–13373.
19. Tieleman, D. P., S. J. Marrink, and H. J. C. Berendsen, 1997. *Biochim. Biophys. Acta* 1331:235–270.
20. Klauda, J. B., R. M. Venable, A. D. M. Jr., and R. W. Pastor, 2008. Considerations for lipid force field development. *In Computational Modeling of Membrane Bilayers*, Elsevier, 2–42.
21. Sapay, N., and D. P. Tieleman, 2008. Molecular Dynamics Simulation of Lipid-Protein Interactions. *In Computational Modeling of Membrane Bilayers*, Elsevier, 112–130.
22. Aqvist, J., and V. Luzhkov, 2000. *Nature* 404:881–884.
23. Jakobsson, E., R. J. Mashl, and T.-T. Tseng, 2002. *Curr. Topics in Membr.* 52:255–273.
24. Roux, B., T. Allen, S. Berneche, and W. Im, 2004. *Q. Rev. Biophys.* 37:15–103.
25. Siu, S. W. I., and R. A. Böckmann, 2009. *J. Phys. Chem. B* 113:3195–3202.
26. Yefimov, S., E. van der Giessen, P. R. Onck, and S. J. Marrink, 2008. *Biophys. J.* 94:2994–3002.
27. Vaccaro, L., K. A. Scott, and M. S. Samsom, 2008. *Biophys. J.* 95:5681–1691.
28. Law, R. J., K. Munson, G. Sachs, and F. C. Lightstone, 2008. *Biophys. J.* 95:2739–49.
29. Bjelkmar, P., P. S. Niemelä, I. Vattulainen, and E. Lindahl, 2009. *PLoS Comput. Biol.* 5:e1000289.

30. Griepernau, B., S. Leis, M. F. Schneider, M. Sikor, D. Steppich, and R. A. Böckmann, 2007. *Biochim. Biophys. Acta* 1768:2899–2913.
31. MacCallum, J. L., and D. P. Tieleman, 2008. Interactions between small molecules and lipid bilayers. *In Computational Modeling of Membrane Bilayers*, Elsevier, 228–256.
32. Berkowitz, M., 2008. On the nature of lipid rafts: insights from molecularly detailed simulations of model biological membranes containing mixtures of cholesterol and phospholipids. *In Computational Modeling of Membrane Bilayers*, Elsevier, 257–280.
33. Risselada, H. J., and S. J. Marrink, 2008. *Proc. Natl. Acad. Sci. USA* 105:17367–17372.
34. Tieleman, D. P., 2004. *BMC Biochemistry* 5:10.
35. Tarek, M., 2005. *Biophys. J.* 88:4045–4053.
36. Böckmann, R. A., B. de Groot, S. Kakorin, E. Neumann, and H. Grubmüller, 2008. *Biophys. J.* 95:1837–1850.
37. Babakhani, A., A. A. Gorfe, J. E. Kim, and J. A. McCammon, 2008. *J. Phys. Chem. B* 112:10528–34.
38. White, S. H., and G. von Heijne, 2008. *Ann. Rev. Biophys.* 37:23–42.
39. Wenk, M. R., 2005. *Nat. Rev. Drug Discov.* 4:594–610.
40. Sud, M., 2007. *Nucleic Acids Res.* 35:D527–D532.
41. Gurr, M. I., J. L. Harwood, and K. N. Frayn, 2002. *Lipid biochemistry* (5th ed.). Blackwell Science.
42. Dowhan, W., and M. Bogdanov, 2002. Functional roles of lipids in membranes. *In Biochemistry of lipids, lipoproteins and membranes* (4th ed.), Elsevier Science, 1–35.
43. Janiak, M. J., D. M. Small, and G. G. Shipley, 1979. *J. Biomol. Chem.* 254:6068–6078.
44. Trauble, H., and H. Eibl, 1974. *Proc. Natl. Acad. Sci. USA* 71:214–219.
45. Silvius, J. R., and P. M. Brown, 1986. *Biochemistry* 25:4249–4258.
46. Cevc, G., 1991. *Biochemistry* 30:7186–7193.
47. Lewis, R. N. A. H., and R. N. McElhaney, 1993. *Biophys. J.* 64:1081–1096.
48. Mateo, C. R., P. Tauc, and J. C. Brochon, 1993. *Biophys. J.* 65:2248–2260.
49. Huang, C.-H., and S. Li, 1999. *Biochim. Biophys. Acta* 1422:273–307.
50. Kranenburg, M., and B. Smit, 2005. *J. Phys. Chem. B* 109:6553–6563.
51. Singer, S. J., and G. L. Nicolson, 1972. *Science* 175:720–731.
52. Walz, D., J. Teissie, and G. Milazzo, 2004. *Bioelectrochemistry of Membrane*. Birkhauser, Basel-Boston-Berlin.
53. Engelman, D. M., 2005. *Nature* 438:578–580.
54. Simons, K., and D. Toomre, 2000. *Nat. Rev. Mol. Cell Biol.* 1:31–39.
55. Alonso, M. A., and J. Millan, 2001. *J. Cell Sci.* 114:3957–3965.
56. Moller, J. V., P. Nissen, T. L.-M. Sorensen, and M. le Maire, 2005. *Curr. Opin. Struct. Biol.* 15:387–393.
57. Marinissen, M. J., and J. S. Gutkind, 2001. *TRENDS in Pharm. Sci.* 22:368–376.
58. Henderson, R., and P. N. T. Unwin, 1975. *Nature* 257:28–32.
59. Deisenhofer, J., O. Epp, K. Miki, R. Huber, and H. Michel, 1985. *Nature* 318:618–624.
60. Membrane proteins of known 3D structure. http://blanco.biomol.uci.edu/Membrane_Proteins_xtal.html.
61. RCSB PDB Protein data bank. <http://www.pdb.org>.
62. Lee, A. G., 2005. *Mol. BioSyst.* 1:203–212.
63. Tsetlin, V., and F. Hucho, 2009. *Curr. Opin. Pharm.* 9:306–310.
64. Bezanilla, F., 2008. *Nat. Rev. Mol. Cell Biol.* 9:323–332.

65. Perozo, E., and D. C. Rees, 2003. *Curr. Opin. Struct. Biol.* 13:432–442.
66. Kelkar, D. A., and A. Chattopadhyay, 2007. *Biochim. Biophys. Acta* 1768:2011–2025.
67. Korn, S. J., and J. G. Trapani, 2007. Voltage-gated potassium channels. In *Biological membrane ion channels*, Springer, 119–170.
68. Morth, J. P., B. P. Pedersen, M. S. Toustrup-Jensen, T. L.-M. Sorensen, J. Petersen, J. P. Andersen, B. Vilsen, and P. Nissen, 2007. *Nature* 450:1043–1049.
69. Marsh, D., A. Watts, R. D. Pates, R. Uhl, P. F. Knowles, and M. Esmann, 1982. *Biophys. J.* 37:265–274.
70. Harroun, T. A., W. T. Heller, T. M. Weiss, L. Yang, and H. W. Huang, 1999. *Biophys. J.* 76:937–945.
71. Weiss, T. M., P. C. A. van der Wel, J. A. Killian, R. E. KoeppeII, and H. W. Huang, 2003. *Biophys. J.* 84:379–385.
72. Hong, H., and L. K. Tamm, 2004. *Proc. Natl. Acad. Sci. USA* 101:4065–4070.
73. O’Keeffe, A. H., J. M. East, and A. G. Lee, 2000. *Biophys. J.* 79:2066–2074.
74. Williamson, I. M., S. J. Alvis, J. M. East, and A. G. Lee, 1002. *Biophys. J.* 83:2026–2038.
75. Powl, A. M., J. M. East, and A. G. Lee, 2003. *Biochemistry* 42:14306–14317.
76. Mall, S. R., R. P. Broadbridge, A. G. Sharma, A. G. Lee, and J. M. East, 2000. *Biochemistry* 39:2071–2078.
77. Newton, A. C., 1993. *Ann. Rev. Biophys. Biomol. Struct.* 22:1–25.
78. Soubias, O., W. E. Teague, and K. Gawrisch, 2006. *J. Biomol. Chem.* 281:33233–33241.
79. Hakizimana, P., M. Masureel, B. Gbaguidi, J.-M. Ruysschaert, and C. Govaerts, 2008. *J. Biomol. Chem.* 238:9369–9376.
80. Bogdanov, M., J. Xie, P. Heacock, and W. Dowhan, 2008. *J. Cell Biol.* 182:925–935.
81. Wikström, M., A. A. Kelly, A. Georgiev, H. M. Eriksson, M. Rosen, Klement, M. Bogdanov, W. Dowhan, and A. Wieslander, 2009. *J. Biomol. Chem.* 284:954–965.
82. Robinson, N. C., J. Zborowski, and L. H. Talbert, 1990. *Biochemistry* 29:8962–8969.
83. Phillips, R., T. Ursell, P. Wiggins, and P. Sens, 2009. *Nature* 459:379–385.
84. Montal, M., and P. Mueller, 1972. *Proc. Natl. Acad. Sci. USA* 69:3561–3566.
85. Fuhrhop, J.-H., and C. Endisch, 2000. *Molecular and supramolecular chemistry of natural products and their model compounds*. CRC Press.
86. Castellana, E. T., and P. S. Cremer, 2006. *Surface Sci. Reports* 61:429–444.
87. Liu, A. L., A. Ottova-Leitmannova, and H. T. Tien, 2008. *ADVANCES IN PLANAR LIPID BILAYERS AND LIPOSOMES*. Academic Press.
88. Luckey, M., 2008. *Membrane structural biology: with biochemical and biophysical foundations*. Cambridge University Press, Cambridge.
89. Lasic, D. D., 1995. *Applications of Liposomes*. In *Handbook of Biological Physics*, vol. I, Elsevier Science, 491–519.
90. Benz, R. W., F. Castro-Roman, D. J. Tobias, and S. H. White, 2005. *Biophys. J.* 88:805–817.
91. Nagle, J. F., and S. Tristram-Nagle, 2000. *Biochim. Biophys. Acta* 1469:159–195.
92. McIntosh, T. J., 1986. *Biochemistry* 25:4948–4952.
93. Wiener, M. C., and S. H. White, 1992. *Biophys. J.* 61:434–447.
94. Seelig, J., 1977. *Q. Rev. Biophys.* 10:353–418.
95. Gawrisch, K., 2005. The dynamics of membrane lipids. In *The Structure of Biological Membranes* (2nd ed.), CRC Press, 147–172.
96. Friesner, R. A., and B. D. Dunietz, 2001. *Acc. Chem. Res.* 34:351–358.
97. van Gunsteren, W. F., D. Bakowies, R. Baron, I. Chandrasekhar, M. Christen, X. Daura, P. Gee, D. P. Geerke, A. Glättli, P. H.

- Hünenberger, M. A. Kastenholz, C. Oostenbrink, M. Schenk, D. Trzesniak, N. F. A. van der Vegt, and H. B. Yu, 2006. *Angew. Chem. Int. Ed. Engl.* 45:4064–4092.
98. Voth, G. A., 2008. Coarse-Graining of Condensed Phase and Biomolecular Systems. CRC Press.
99. Earl, D. J., and M. W. Deem, 2008. Monte Carlo Simulations. In *Molecular Modeling of Proteins (Methods in Molecular Biology)*, Humana Press, 25–36.
100. Dickinson, E., 1985. *Chem. Soc. Rev.* 14:421–455.
101. Chen, J., C. L. B. III, and J. Khandogin, 2008. *Curr. Opin. Struct. Biol.* 18:140–148.
102. Sanbonmatsu, K. Y., and C. S. Tung, 2007. *J. Struct. Biol.* 157:470–480.
103. Hess, B., C. Kutzner, D. van der Spoel, and E. Lindahl, 2008. *J. Chem. Theory and Comput.* 4:435–447.
104. Feller, S. E., D. Huster, and K. Garwrisch, 1999. *J. Am. Chem. Soc.* 121:8963–8964.
105. Böckmann, R. A., B. L. de Groot, S. Kakorin, E. Neumann, and H. Grubmüller, 2008. *Biophys. J.* 95:1837–1850.
106. Chung, S. H., O. S. Andersen, and V. K. (Eds.), 2007. *Biological Membrane Ion Channels: Dynamics, structure, and applications*. Springer.
107. Khalili-Araghi, F., J. Gumbart, P.-C. Wen, M. Sotomayor, E. Tajkhorshid, and K. Schulten, 2009. *Curr. Opin. Struct. Biol.* 19:128–137.
108. Kristiansen, K., 2004. *Pharmacology & Therapeutics* 103:21–80.
109. Crozier, P. S., M. J. Stevens, and T. B. Woolf, 2007. *PROTEINS: Struct., Func. & Bioinf.* 66:559–574.
110. Mobarec, J. C., and M. Filizola, 2008. *Expert Opin. Drug Discov.* 3:343–355.
111. Böckmann, B. A., and H. Grubmüller, 2002. *Nat. Struct. Biol.* 9:198–202.
112. Pu, J., and M. Karplus, 2008. *Proc. Natl. Acad. Sci. USA* 105:1192–1197.
113. Blood, P. D., R. D. Swenson, and G. A. Voth, 2008. *Biophys. J.* 95:1866–1876.
114. Hsin, J., J. Gumbart, L. G. Trabuco, E. Villa, P. Qian, C. N. Hunter, and K. Schulten, 2009. *Biophys. J.* 97:321–329.
115. Johansson, A. C. V., and E. Lindahl, 2006. *Biophys. J.* 91:4450–4463.
116. MacCallum, J. L., W. F. D. Bennet, and D. P. Tieleman, 2007. *J. Gen. Physiology* 129:371–377.
117. Becker, M. D., D. V. Greathouse, R. E. Koeppe II, and O. S. Andersen, 1991. *Biochemistry* 30:8830–8839.
118. Andersen, O. S., D. V. Greathouse, L. L. Providence, M. D. Becker, and R. E. Koeppe, 1998. *Biophys. J.* 120:5142–5146.
119. de Planque, M. R. R., B. B. Bonev, J. A. A. Demmers, D. V. Greathouse, R. E. K. II, F. Separovic, A. Watts, and J. A. Killian, 2003. *Biochemistry* 42:5341–5348.
120. Freites, J. A., D. J. Tobias, and S. H. White, 2006. *Biophys. J.* 91:90–92.
121. Horn, R., 2005. *Proc. Natl. Acad. Sci. USA* 102:4929–4930.
122. Ponder, J. W., and D. A. Case, 2003. *Adv. Prot. Chem.* 66:27–85.
123. MacKerell, A. D., D. Bashford, M. Bellott, R. L. Dunbrack, J. D. Evanseck, M. J. Field, S. Fischer, J. Gao, H. Guo, S. Ha, D. Joseph-McCarthy, L. Kuchnir, K. Kuczera, F. T. K. Lau, C. Mattos, S. Michnick, T. Ngo, D. T. Nguyen, B. Prodhom, W. E. Reiher, B. Roux, M. Schlenkrich, J. C. Smith, R. Stote, J. Straub, M. Watanabe, J. Wiorkiewicz-Kuczera, D. Yin, and M. Karplus, 1998. *J. Phys. Chem. B* 102:3586–3616.
124. Oostenbrink, C., A. Villa, A. E. Mark, and W. F. van Gunsteren, 2004. *J. Comput. Chem.* 25:1656–1676.
125. Kaminski, G., R. A. Friesner, J. Tirado-Rives, and W. L. Jorgensen, 2001. *J. Phys. Chem. B* 105:6474–6487.
126. Jorgensen, W. L., D. S. Maxwell, and J. Tirado-Rives, 1996. *J. Am. Chem. Soc.* 96:11225–11236.

127. Feller, S. E., and J. A. D. MacKerell, 2000. *J. Phys. Chem. B* 104:7510–7515.
128. Berger, O., O. Edholm, and F. Jähnig, 1997. *Biophys. J.* 72:2002–2013.
129. Tieleman, D. P., J. L. MacCallum, W. L. Ash, C. Kandt, Z. Xu, and L. Monticelli, 2006. *J. Phys.: Condens. Matter* 18:S1221–S1234.
130. Wang, J., R. M. Wolf, J. W. Caldwell, P. A. Kollman, and D. A. Case, 2004. *J. Comput. Chem.* 25:1157–1174.
131. Jójárt, B., and T. A. Martinek, 2007. *J. Comput. Chem.* 28:2051–2058.
132. Siu, S. W. I., R. Vacha, P. Jungwirth, and R. A. Böckmann, 2008. *J. Chem. Phys.* 128:125103.
133. Roux, B., 1995. *Comput. Phys. Comm.* 91:275–282.
134. Isralewitz, B., M. Gao, and K. Schulten, 2001. *Curr. Opin. Struct. Biol.* 11:224–230.
135. Venturoli, M., M. M. Sperotto, and M. Kraneburg, 2006. *Phys. Rep.* 437:1–54.
136. Lindahl, E., and M. S. Samsom, 2008. *Curr. Opin. Struct. Biol.* 18:425–431.
137. Ayton, G. S., and G. A. Voth, 2009. *Curr. Opin. Struct. Biol.* 19:138–144.
138. Marrink, S., H. Risselada, S. Yefimov, D. Tieleman, and A. de Vries, 2007. *J. Phys. Chem. B* 111:7812–7824.
139. Jungwirth, P., and D. J. Tobias, 2006. *Chem. Rev.* 106:1259–1281.
140. Lill, M. A., and V. Helms, 2001. *J. Chem. Phys.* 115:7993–8005.
141. Frenkel, D., and B. Smit, 2002. *Understanding Molecular Simulation: From Algorithms to Applications*. Academic Press, San Diego.
142. Berendsen, H. J. C., J. P. M. Postma, W. F. van Gunsteren, A. D. Nola, and J. R. Haak, 1984. *J. Chem. Phys.* 81:3684–3690.
143. Brooks, C. L., B. M. Pettitt, and M. Karplus, 1985. *J. Chem. Phys.* 83:5897.
144. Loncharich, R. J., and B. R. Brooks, 1989. *PROTEINS: Struct., Func. & Bioinf.* 6:32–45.
145. Norberg, J., and L. Nilsson, 2000. *Biophys. J.* 79:1537–1553.
146. Ewald, P. P., 1921. *Ann. Phys.* 64:253–287.
147. Darden, T., D. York, and L. Pedersen, 1993. *J. Chem. Phys.* 98:10089–10092.
148. Zwanzig, R. W., 1954. *J. Chem. Phys.* 22:1420–1426.
149. Beveridge, D. L., and F. M. DiCapua, 1989. *Ann. Rev. Biophys. Biophys. Chem.* 18:431–92.
150. Kirkwood, J. G., 1935. *J. Chem. Phys.* 3:300.
151. Edwards, S., B. Corry, S. Kuyucak, and S.-H. Chung, 2002. *Biophys. J.* 83:1348–1360.
152. Torrie, G. M., and J. P. Valleau, 1977. *J. Comput. Phys.* 23:187–199.
153. Kumar, S., D. Bouzida, R. H. Swendsen, P. A. Kollman, and J. M. Rosenberg, 1992. *J. Comput. Chem.* 13:1011–1021.
154. Lill, M. A., and V. Helms, 2001. *J. Chem. Phys.* 114:1125–1132.
155. Lill, M. A., and V. Helms, 2001. *J. Chem. Phys.* 115:7985–7992.
156. Lill, M. A., and V. Helms, 2002. *Proc. Natl. Acad. Sci. USA* 99:2778–2781.
157. de Groot, B. L., T. Frigato, V. Helms, and H. Grubmüller, 2003. *J. Molec. Biol.* 333:279–293.
158. Gu, W., T. Frigato, T. P. Straatsma, and V. Helms, 2007. *Angew. Chem. Int. Ed. Engl.* 46:2939–2943.
159. Straatsma, T. P., and J. A. McCammon, 1990. *J. Comput. Chem.* 11:943–951.
160. Kendall, R. A., E. Apra, D. E. Bernholdt, E. J. Bylaska, M. Dupuis, G. I. Fann, R. J. Harrison, J. Ju, J. A. Nichols, J. Nieplocha, T. P. Straatsma, T. L. Windus, and A. A. T. Wong, 2000. *Comput. Phys. Comm.* 128:260–283.
161. Berendsen, H. J. C., D. van der Spoel, and R. van Drunen, 1995. *Comput. Phys. Comm.* 91:43–56.
162. Huggins, M. L., 1936. *J. Phys. Chem.* 40:723.
163. Lu, D., and G. A. Voth, 1998. *J. Am. Chem. Soc.* 120:4006–4014.

164. Lill, M. A., M. C. Hutter, and V. Helms, 2000. *J. Phys. Chem. A* 104:8283–8289.
165. Herzog, E., T. Frigato, V. Helms, and C. R. D. Lancaster, 2006. *J. Comput. Chem.* 27:1534–1547.
166. Hänggi, P., P. Talkner, and M. Borkovec, 1990. *Rev. Modern Phys.* 62:251–341.
167. Neumann, E., M. Schaefer-Ridder, Y. Wang, and P. H. Hofschneider, 1982. *EMBO J.* 1:841–845.
168. Belehradek, M., C. Domenge, B. Luboinski, S. Orłowski, J. Belehradek, and L. M. Mir, 1993. *Cancer* 72:3694–3700.
169. Mir, L. M., S. Orłowski, J. Belehradek, J. Teissie, M. P. Rols, G. Sersa, D. Miklavcic, R. Gilbert, and R. Heller, 1995. *Bioelectrochemistry Bioenergetics* 38:203–207.
170. Mir, L. M., M. F. Bureau, J. Gehl, R. Rangara, D. Rouy, J.-M. Caillaud, P. Delaere, D. Branellec, B. Schwartz, and D. Scherman, 1999. *Proc. Natl. Acad. Sci. USA* 96:4262–4267.
171. Glasspool-Malone, J., S. Somiari, J. J. Drabick, and R. W. Malone, 2000. *Mol. Ther.* 2:140–146.
172. Drabick, J. J., J. Glasspool-Malone, S. Somiari, A. King, and R. W. Malone, 2001. *Mol. Ther.* 3:249–255.
173. Saeboe-Larssen, S., E. Fossberg, and G. Gaudernack, 2002. *J. Immunol. Meth.* 259:191–203.
174. Van Meirvenne, S., L. Straetman, C. Heirman, M. Dullaers, C. De Greef, V. Van Tendeloo, and K. Thielemans, 2002. *Cancer Gene Ther.* 9:787–797.
175. Pfanner, N., and W. Neupert, 1985. *EMBO J.* 4:2819–2825.
176. Neupert, W., 1997. *Ann. Rev. Biochem.* 66:863–917.
177. Weber, J., and A. E. Senior, 2003. *FEBS Lett.* 545:61–70.
178. Dimroth, P., C. von Ballmoos, and T. Meier, 2006. *EMBO Reports* 7:276–282.
179. Tsong, T. Y., 2004. Electroconformational Coupling. In *Bioelectrochemistry of Membranes*. Birkhäuser Verlag, Basel–Boston–Berlin.
180. Ramos, C., and J. Teissie, 2000. *Biochimie* 82:511–518.
181. Hofmann, F., H. Ohnimus, C. Scheller, W. Strupp, U. Zimmermann, and C. Jassoy, 1999. *J. Membr. Biol.* 169:103–109.
182. Stämpfli, R., 1958. *An. Acad. Brasil. Ciens.* 30:57–63.
183. Sale, A. J. H., and W. A. Hamilton, 1967. *Biochim. Biophys. Acta* 148:781–788.
184. Neumann, E., and K. Rosenheck, 1972. *J. Molec. Biol.* 10:279–290.
185. Weaver, J. C., and Y. A. Chizmadzhev, 1996. *Bioelectrochemistry Bioenergetics* 41:135–160.
186. Chizmadzhev, Y. A., J. Teissie, and D. Walz, 2004. Lipid bilayer electropermeabilization. In *Bioelectrochemistry of Membranes*, Birkhäuser Verlag, Basel–Boston–Berlin, 173–203.
187. Teissie, J., 2004. Cell membrane electropermeabilization. In *Bioelectrochemistry of Membranes*, Birkhäuser Verlag, Basel–Boston–Berlin, 205–235.
188. Hu, Q., S. Viswanadham, R. P. Joshi, K. H. Schoenbach, S. J. Beebe, and P. F. Blackmore, 2005. *Phys. Rev. E* 71:031914.
189. Hu, Q., R. P. Joshi, and K. H. Schoenbach, 2005. *Phys. Rev. E* 72:031902.
190. Gurtovenko, A. A., and I. Vattulainen, 2005. *J. Am. Chem. Soc.* 127:17570–17571.
191. Troiano, G. C., K. J. Stebe, R. M. Raphael, and L. Tung, 1999. *Biophys. J.* 76:3150–3157.
192. Wallace, B. A., 1981. *J. Membr. Biol.* 59:155–171.
193. Mackay, D. H., P. H. Berens, K. R. Wilson, and A. T. Hagler, 1994. *Biophys. J.* 46:229–248.
194. Chiu, S. W., E. Jakobsson, S. Subramaniam, and J. A. McCammon, 1991. *Biophys. J.* 60:273–285.
195. Roux, B., and M. Karplus, 1993. *J. Am. Chem. Soc.* 115:3250–3262.
196. de Groot, B. L., D. P. Tieleman, P. Pohl, and H. Grubmüller, 2002. *Biophys. J.* 82:2934–2942.
197. Andersen, O. S., R. E. Koeppe, and B. Roux, 2005. *IEEE Trans. Nanobiosci.* 4:10–20.

198. Bastug, T., and S. Kuyucak, 2006. *Biophys. J.* 90:3941–3950.
199. Allen, T. W., T. Bastug, S. Kuyucak, and S.-H. Chung, 2003. *Biophys. J.* 84:2159–2168.
200. Allen, T. W., O. S. Andersen, and B. Roux, 2004. *Proc. Natl. Acad. Sci. USA* 101:117–122.
201. Woolf, T. B., and B. Roux, 1994. *Proc. Natl. Acad. Sci. USA* 91:11631–11635.
202. Bastug, T., A. Gray-Weale, S. M. Patra, and S. Kuyucak, 2006. *Biophys. J.* 90:2285–2296.
203. Tang, P., and Y. Xu, 2002. *Proc. Natl. Acad. Sci. USA* 99:16035–16040.
204. Mobashery, N., C. Nielsen, and O. S. Andersen, 1997. *FEBS Lett.* 412:15–20.
205. Chen, Y., and B. A. Wallace, 1997. *Europ. Biophys. J.* 26:299–306.
206. Andersen, O. S., H.-J. Apell, E. Bamberg, D. D. Busath, R. E. Koeppe, F. J. Sigworth, G. Szabo, D. W. Urry, and A. Woolley, 1999. *Nat. Struct. Biol.* 6:609.
207. Cross, T. A., A. Arseniev, B. A. Cornell, J. H. Davis, J. A. Killian, R. E. Koeppe, L. K. Nicholson, F. Separovic, and B. A. Wallace, 1999. *Nat. Struct. Biol.* 6:610–611.
208. Burkhart, B. M., and W. L. Duax, 1999. *Nat. Struct. Biol.* 6:611–612.
209. Burkhart, B. M., N. Li, D. A. Langa, W. A. Pangborn, and W. L. Duax, 1998. *Proc. Natl. Acad. Sci. USA* 95:12950–12955.
210. Ketchum, R. R., K. C. Lee, S. Huo, and T. A. Cross, 1996. *J. Biomol. NMR* 8:1–14.
211. Faraldo-Gomez, J. D., G. R. Smith, and M. S. P. Sansom, 2002. *Europ. Biophys. J.* 31:217–227.
212. Lindahl, E., B. Hess, and D. van der Spoel, 2001. *J. Mol. Model.* 7:306–317.
213. Jorgensen, W. L., J. Chandrasekhar, and J. D. Madura, 1983. *J. Chem. Phys.* 79:926–935.
214. Böckmann, R. A., and A. Cafilisch, 2005. *Biophys. J.* 88:3191–3204.
215. Hess, B., H. Bekker, H. J. C. Berendsen, and J. G. E. M. Fraaije, 1997. *J. Comput. Chem.* 18:1463–1472.
216. Miyamoto, S., and P. A. Kollman, 1992. *J. Comput. Chem.* 13:952–962.
217. Allen, M. P., and D. J. Tildesley, 1987. *Computer Simulations of Liquids*. Clarendon, Oxford.
218. Bernal, J. D., 1959. *Nature* 183:141–147.
219. Patra, M., E. Salonen, E. Terama, I. Vattulainen, R. Faller, B. W. Lee, J. Holopainen, and M. Karttunen, 2006. *Biophys. J.* 90:1121–1135.
220. Lewis, B. A., and D. M. Engelman, 1983. *J. Molec. Biol.* 166:211–217.
221. Balgav, P., M. Dubnickov, N. Kucerka, M. A. Kiselev, S. P. Yaradaikin, and D. Uhrkov, 2001. *Biochim. Biophys. Acta* 1512:40–52.
222. Kucerka, N., Y. Liu, N. Chu, H. I. Petrache, S. Tristram-Nagle, and J. F. Nagle, 2005. *Biophys. J.* 88:2626–2637.
223. Tang, Y. Z., W. Z. Chen, and C. X. Wang, 2000. *Europ. Biophys. J.* 29:523–534.
224. Allen, T. W., O. S. Andersen, and B. Roux, 2003. *J. Am. Chem. Soc.* 125:9868–9877.
225. Rice, D., and E. Oldfield, 1979. *Biochemistry* 18:3272–3279.
226. Douliez, J.-P., A. Leonard, and E. J. Dufourc, 1995. *Biophys. J.* 68:1727–1739.
227. Chiu, S.-W., S. Subramaniam, and E. Jakobsson, 1999. *Biophys. J.* 76:1929–1938.
228. Al-Momani, L., P. Reiß, and U. Koert, 2005. *Biochem. Biophys. Res. Comm.* 328:342–347.
229. Böckmann, R. A., A. Hac, T. Heimburg, and H. Grubmüller, 2003. *Biophys. J.* 85:1647–1655.
230. Chiu, S.-W., S. Subramaniam, and E. Jakobsson, 1999. *Biophys. J.* 76:1939–1950.
231. Killian, J. A., K. U. Prasad, D. Hains, and D. W. Urry, 1988. *Biochemistry* 27:4848–4855.
232. LoGrasso, P. V., F. Moll, and T. A. Cross, 1988. *Biophys. J.* 54:259–267.

233. Bano, M. C., L. Braco, and C. Abad, 1991. *Biochemistry* 30:886–894.
234. Bamberg, E., and P. Läuger, 1974. *Biochim. Biophys. Acta* 367:127–133.
235. Arndt, H.-D., D. Bockelmann, A. Knoll, S. Lamberth, C. Griesinger, and U. Koert, 2002. *Angew. Chem. Int. Ed. Engl.* 41:4062–4065.
236. Arseniev, A. S., I. L. Barsukov, and V. F. Bystrov, 1985. *FEBS Lett.* 180:33–39.
237. Ketchum, R. R., B. Roux, and T. A. Cross, 1997. *Structure* 5:1655–1669.
238. Lomize, A. L., V. Y. Orekhov, and A. S. Arseniev, 1992. *Bioorgan. Chemistry* 18:182–200.
239. Cornell, B., 1987. *J. Bioener. Biomem.* 19:655–676.
240. The PyMOL Molecular Graphics System. <http://www.pymol.org>.
241. Urry, D. W., M. C. Goodall, J. D. Glickson, and D. F. Mayers, 1971. *Proc. Natl. Acad. Sci. USA* 68:1907–1911.
242. Bamberg, E., H. J. Apell, and H. Alpes, 1977. *Proc. Natl. Acad. Sci. USA* 74:2402–2406.
243. Apell, H. J., E. Bamberg, H. Alpes, and P. Läuger, 1977. *J. Membr. Biol.* 31:171–188.
244. Weinstein, S., B. A. Wallace, E. R. Blout, J. S. Morrow, and W. Veatch, 1979. *Proc. Natl. Acad. Sci. USA* 76:4230–4234.
245. Wallace, B. A., W. R. Veatch, and E. R. Blout, 1981. *Biochemistry* 20:5754–5760.
246. Levitt, D. G., 1978. *Biophys. J.* 22:209–219.
247. Monoi, H., 1991. *Biophys. J.* 59:786–794.
248. Nadler, B., U. Hollerbach, and R. S. Eisenberg, 2003. *Phys. Rev. E* 68:021905.
249. Åqvist, J., and A. Warshel, 1989. *Biophys. J.* 56:171–182.
250. Mamonov, A. B., R. D. Coalson, A. Nitzan, and M. G. Kurnikova, 2003. *Biophys. J.* 84:3646–3661.
251. Dorman, V. L., and P. C. Jordan, 2004. *Biophys. J.* 86:3259–3541.
252. Kato, M., and A. Warshel, 2005. *J. Phys. Chem. B* 109:19516–19522.
253. Braun-Sand, S., A. Burykin, Z. T. Chu, and A. Warshel, 2005. *J. Phys. Chem. B* 109:583–592.
254. Allen, T. W., O. S. Andersen, and B. Roux, 2006. *Biophys. J.* 90:3447–3468.
255. Liu, Z., Y. Xu, and P. Tang, 2006. *J. Phys. Chem. B* 110:12789–12795.
256. Bastug, T., and S. Kuyucak, 2006. *Biophys. J.* 90:3941–3950.
257. Bastug, T., and S. Kuyucak, 2007. *J. Chem. Phys.* 126:105103.
258. Qin, Z., H. L. Tepper, and G. A. Voth, 2007. *J. Phys. Chem. B* 111:9931–9939.
259. Fabritiis, G. D., P. V. Coveney, and J. Villá-Freixa, 2008. *Proteins* 73:185–194.
260. Siu, S. W. I., and R. A. Böckmann, 2007. *J. Struct. Biol.* 157:545–556.
261. Kucerka, N., Y. Liu, N. Chu, H. I. Petrache, S. Tristram-Nagle, and J. F. Nagle, 2004. *Biophys. J.* 88:2626–2637.
262. Straatsma, T. P., H. J. C. Berendsen, and J. P. M. Postma, 1986. *J. Chem. Phys.* 85(11):6720–6727.
263. Warshel, A., P. K. Sharma, M. Kato, and W. W. Parson, 2006. *Biochim. Biophys. Acta* 1764:1647–1676.
264. Figueirido, F., R. M. Levy, R. Zhou, and J. Berne, 1997. *J. Chem. Phys.* 106:9835–9849.
265. Bastug, T., S. M. Patra, and S. Kuyucak, 2006. *Chem. Phys. Lipids* 141:197–204.
266. Olah, G. A., H. W. Huang, W. Liu, and Y. Wu, 1991. *J. Molec. Biol.* 218:847–858.
267. Koeppe, R. E., J. M. Berg, K. O. Hodgson, and L. Stryer, 1979. *Nature* 279:723–725.
268. Urry, D. W., K. U. Prasad, and T. L. Trapane, 1982. *Proc. Natl. Acad. Sci. USA* 79:390–394.
269. Bastug, T., and S. Kuyucak, 2008. *J. Chem. Phys.* 128:227102.
270. Okamura, E., J. Umemura, and T. Takenaka, 1986. *Biochim. Biophys. Acta* 856:68–75.

271. Prosser, R. S., and J. H. Davis, 1994. *Biophys. J.* 66:1429–1440.
272. Ulrich, W.-P., and H. Vogel, 1999. *Biophys. J.* 76:1639–1647.
273. Kóta, Z., T. Páli, and D. Marsh, 2004. *Biophys. J.* 86:1521–1531.
274. van der Wel, P. C. A., E. Strandberg, J. A. Killian, and R. E. Koeppe, 2002. *Biophys. J.* 83:1479–1488.
275. Strandberg, E., S. Özdirekcan, D. T. S. Rijkers, P. C. A. van der Wel, R. E. Koeppe, R. M. J. Liskamp, and J. A. Killian, 2004. *Biophys. J.* 86:3709–3721.
276. Killian, J. A., 1998. *Biochim. Biophys. Acta* 1376:401–416.
277. Sengupta, D., L. Meinhold, D. Langosch, G. M. Ullmann, and J. C. Smith, 2005. *Proteins* 58:913–922.
278. Ulmschneider, M. B., M. S. P. Sansom, and A. D. Nola, 2006. *Biophys. J.* 90:1650–1660.
279. Smart, O. S., J. G. Neduelil, X. Wang, B. A. Wallace, and M. S. P. Sansom, 1996. *J. Mol. Graphics* 14:354–360.
280. Roux, B., and S. Bernéche, 2002. *Biophys. J.* 82:1681–1684.
281. Saparov, S. M., Y. N. Antonenko, R. E. Koeppe, and P. Pohl, 2000. *Biophys. J.* 79:2526–2534.
282. Hladky, S. B., and D. A. Haydon, 1972. *Biochim. Biophys. Acta* 274:294–312.
283. Urry, D. W., S. Alonso-Romanowski, C. M. Venkatachalam, R. D. Harris, and K. U. Prasad, 1984. *Biochem. Biophys. Res. Comm.* 118:885–893.
284. Busath, D. D., C. D. Thulin, R. W. Hendershot, L. R. Phillips, P. Maughan, C. D. Cole, N. C. Bingham, S. Morrison, L. C. Baird, R. J. Hendershot, M. Cotten, and T. A. Cross, 1998. *Biophys. J.* 75:2830–2844.
285. Rottenberg, H., and R. E. Koeppe-II, 1989. *Biochemistry* 28:4361–4367.
286. Trudell, J. R., 1977. *Anesthesiology* 46:5–10.
287. Cantor, R. S., 1997. *Biochemistry* 36:2339–2344.
288. Silvius, J. R., 2003. *Biochim. Biophys. Acta* 1610:174–183.
289. Hofsäß, C., E. Lindahl, and O. Edholm, 2003. *Biophys. J.* 84:2192–2206.
290. Urban, B. W., 2006. *Pharmacology & Therapeutics* 111:729–770.
291. Högberg, C.-J., and A. P. Lyubartsev, 2008. *Biophys. J.* 94:525–531.
292. Pandit, S. A., D. Bostick, and M. L. Berkowitz, 2003. *Biophys. J.* 84:3743–3750.
293. Herbette, L., C. A. Napolitano, and R. V. McDaniel, 1984. *Biophys. J.* 46:677–685.
294. Böckmann, R. A., and H. Grubmüller, 2004. *Angew. Chem. Int. Ed. Engl.* 43:1021–1024.
295. Heimburg, T., and A. D. Jackson, 2005. *Proc. Natl. Acad. Sci. USA* 102:9790–9795.
296. Heimburg, T., and A. D. Jackson, 2007. *Biophys. J.* 92:3159–3165.
297. Ash, W. L., M. R. Zlomislic, E. O. Oloo, and D. P. Tieleman, 2004. *Biochim. Biophys. Acta* 1666:158–189.
298. Berkowitz, M. L., D. L. Bostick, and S. Pandit, 2006. *Chem. Rev.* 106:1527–1539.
299. Castro-Roman, F., R. W. Benz, S. H. White, and D. J. Tobias, 2006. *J. Phys. Chem. B* 110:24157–24164.
300. Schlenkrich, M., J. Brickmann, A. D. MacKerell, and M. Karplus, 1996. Empirical potential energy function for phospholipids: Criteria for parameter optimization and applications., Birkhäuser, 31–81.
301. Chiu, S.-W., M. Clark, V. Balaji, S. Subramaniam, H. L. Scott, and E. Jakobsson, 1995. *Biophys. J.* 69:1230–1245.
302. Jorgensen, W. L., and J. Tirado-Rives, 1988. *J. Am. Chem. Soc.* 110:1657–1666.
303. Chanda, J., and S. Bandyopadhyay, 2006. *Langmuir* 22:3775–3781.
304. Bayly, C. I., P. Cieplak, W. D. Cornell, and P. A. Kollman, 1993. *J. Phys. Chem.* 97:10269–10280.

305. Cornell, W. D., P. Cieplak, C. I. Bayly, and P. A. Kollman, 1993. *J. Am. Chem. Soc.* 115:9620–9631.
306. Feller, S. E., D. Yin, R. W. Pastor, and A. D. MacKerell, 1997. *Biophys. J.* 73:2269–2279.
307. Lipid coordinate sets. <http://persweb.wabash.edu/facstaff/fellers>.
308. Tristram-Nagle, S., H. I. Petrache, and J. F. Nagle, 1998. *Biophys. J.* 75:917–925.
309. Gunsteren, W. F. V., and H. J. C. Berendsen, 1987. Gromos User Manual. BIOMOS biomolecular software, Laboratory of Physical Chemistry, University of Groningen, The Netherlands.
310. Frisch, M. J., G. W. Trucks, H. B. Schlegel, G. E. Scuseria, M. A. Robb, J. R. Cheeseman, J. A. Montgomery, Jr., T. Vreven, K. N. Kudin, J. C. Burant, J. M. Millam, S. S. Iyengar, J. Tomasi, V. Barone, B. Mennucci, M. Cossi, G. Scalmani, N. Rega, G. A. Petersson, H. Nakatsuji, M. Hada, M. Ehara, K. Toyota, R. Fukuda, J. Hasegawa, M. Ishida, T. Nakajima, Y. Honda, O. Kitao, H. Nakai, M. Klene, X. Li, J. E. Knox, H. P. Hratchian, J. B. Cross, V. Bakken, C. Adamo, J. Jaramillo, R. Gomperts, R. E. Stratmann, O. Yazyev, A. J. Austin, R. Cammi, C. Pomelli, J. W. Ochterski, P. Y. Ayala, K. Morokuma, G. A. Voth, P. Salvador, J. J. Dannenberg, V. G. Zakrzewski, S. Dapprich, A. D. Daniels, M. C. Strain, O. Farkas, D. K. Malick, A. D. Rabuck, K. Raghavachari, J. B. Foresman, J. V. Ortiz, Q. Cui, A. G. Baboul, S. Clifford, J. Cioslowski, B. B. Stefanov, G. Liu, A. Liashenko, P. Piskorz, I. Komaromi, R. L. Martin, D. J. Fox, T. Keith, M. A. Al-Laham, C. Y. Peng, A. Nanayakkara, M. Challacombe, P. M. W. Gill, B. Johnson, W. Chen, M. W. Wong, C. Gonzalez, and J. A. Pople. Gaussian 03, Revision C.02. Gaussian, Inc., Wallingford, CT, 2004.
311. Berendsen, H. J. C., J. P. M. Postma, W. F. Van Gunsteren, and J. Hermans, 1981. Interaction model for water in relation to protein hydration., D. Reidel Publishing Company, Dordrecht, The Netherlands, 331–342.
312. Jorgensen, W. L., J. Chandrasekhar, and J. D. Madura, 1983. *J. Chem. Phys.* 79:926–935.
313. Berendsen, H. J. C., J. R. Grigera, and T. P. Straatsma, 1987. *J. Phys. Chem.* 91:6269–6271.
314. Seelig, J., 1977. *Quarterly Reviews of Biophysics* 10:353–418.
315. Douliez, J. P., A. Ferrarini, and E. J. Dufourc, 1998. *J. Chem. Phys.* 109:2513–2518.
316. Klauda, J. B., B. R. Brooks, and R. W. Pastor, 2006. *J. Chem. Phys.* 125:144710.
317. Liu, Y., and J. F. Nagle, 2004. *Phys. Rev. E* 69:40901.
318. Jensen, M. O., O. G. Mouritsen, and G. H. Peters, 2004. *Biophys. J.* 86:3556–3575.
319. Sonne, J., M. O. Jensen, F. Y. Hansen, L. Hemmingsen, and G. H. Peters, 2007. *Biophys. J.* 92:4157–4167.
320. Seelig, J., and N. Waespe-Sarcevic, 1978. *Biochemistry* 17:3310–3315.
321. Pandit, S. A., S.-W. Chiu, E. Jakobsson, A. Grama, and H. L. Scott, 2007. *Biophys. J.* 92:920–927.
322. Warschawski, D. E., and P. F. Devaux, 2005. *Eur. Biophys. J.* 34:987–996.
323. Seelig, A., and J. Seelig, 1975. *Biochim. Biophys. Acta* 406:1–5.
324. Hitchcock, P. B., R. Mason, K. M. Thomas, and G. G. Shipley, 1974. *Proc. Natl. Acad. Sci. USA* 71:3036–3040.
325. Klauda, J. B., B. R. Brooks, A. D. MacKerell, R. M. Venable, and R. W. Pastor, 2005. *J. Phys. Chem. B* 109:5300–5311.
326. Bhide, S. Y., and M. L. Berkowitz, 2005. *J. Chem. Phys.* 123:224702.
327. Chiu, S. W., E. Jakobsson, S. Subramaniam, and H. L. Scott, 1999. *Biophys. J.* 77:2462–2469.
328. Engel, A. K., and D. Cowburn, 1981. *FEBS Lett.* 126:169.
329. König, S., T. M. Bayerl, G. Coddens, D. Richter, and E. Sackmann, 1995. *Biophys. J.* 68:1871–1880.
330. Filippov, A., G. Orädd, and G. Lindblom, 2003. *Langmuir* 19:6397–6400.
331. Pfeiffer, W., T. Henkel, E. Sackmann, and W. Knoll, 1989. *Europhys. Lett.* 8:201–206.

332. Tabony, J., and B. Perly, 1990. *Biochim. Biophys. Acta* 1063:67–72.
333. Lopez, C. F., S. O. Nielsen, and M. L. Klein, 2004. *J. Phys. Chem. B* 108:6603–6610.
334. Mahoney, M. W., and W. L. Jorgensen, 2001. *J. Chem. Phys.* 114:363–366.
335. Mills, R., 1973. *J. Phys. Chem.* 77:685–688.
336. Brockman, H., 1994. *Chem. Phys. Lipids* 73:57–79.
337. Clarke, R. J., 2001. *Adv. Colloid Interface Sci.* 89:263–281.
338. Clarke, R. J., 1997. *Biochim. Biophys. Acta* 1327:269–278.
339. Gawrisch, K., D. Ruston, J. Zimmerberg, V. A. Parsegian, R. P. Rand, and N. Fuller, 1992. *Biophys. J.* 61:1213–1223.
340. Mashl, R. J., H. L. Scott, S. Subramaniam, and E. Jacosson, 2001. *Biophys. J.* 81:3005–3015.
341. Pandit, A. A., D. Bostick, and M. L. Berkowitz, 2003. *J. Chem. Phys.* 119:2199–2205.
342. Pearson, R. H., and I. Pascher, 1979. *Nature* 281:499–501.
343. Hauser, H., I. Pascher, R. H. Pearson, and S. Sundell, 1981. *Biochim. Biophys. Acta* 650:21–51.
344. Chandrasekhar, I., M. Kastenholz, R. D. Lins, C. Oostenbrink, L. D. Schuler, D. P. Tieleman, and W. F. van Gunsteren, 2003. *Europ. Biophys. J.* 32:67–77.
345. Jähnig, F., 1996. *Biophys. J.* 71:1348–1349.
346. Marrink, S. J., and A. E. Mark, 2001. *J. Phys. Chem.* 105:6122–6127.
347. Gullingsrud, J., A. Babakhani, and J. A. McCammon, 2006. *Molec. Sim.* 32:831–838.
348. Ball, P., 2008. *Chem. Rev.* 108:74–108.
349. von Grothuss, C. J. D., 1806. *Annales de Chimie* 58:54–74.
350. Erdely-Gruz, T., 1974. *Transport Phenomena in Electrolyte Solutions*. Adam Higler, London.
351. Eigen, M., 1963. *Angew. Chem. Int. Ed. Engl.* 3:1.
352. Zundel, G., 2000. *Adv. Chem. Phys.* 111:1.
353. Tuckerman, M., K. Laasonen, M. Sprik, and M. Parrinello, 1995. *J. Chem. Phys.* 103:150–161.
354. Agmon, N., 1999. *Isr. J. Chem.* 39:493–502.
355. Asthagiri, D., L. R. Pratt, and J. D. Kress, 2005. *Proc. Natl. Acad. Sci. USA* 102:6704–6708.
356. Agmon, N., 1995. *Chem. Phys. Lett.* 244:456–462.
357. Woutersen, S., and H. J. Bakker, 2006. *Phys. Rev. Lett.* 96:138305.
358. Marx, D., M. E. Tuckerman, J. Hutter, and M. Parrinello, 1999. *Nature* 397:601–604.
359. Chandra, A., M. E. Tuckerman, and D. Marx, 2007. *Phys. Rev. Lett.* 99:145901.
360. Markovitch, O., H. Chen, S. Izvekov, F. Paesani, G. A. Voth, and N. Agmon, 2008. *J. Phys. Chem. B* 112:9456–9466.
361. Car, R., and M. Parrinello, 1985. *Phys. Rev. Lett.* 55:2471–2474.
362. Marx, D., 2006. *Chem. Phys. Chem.* 7:1848–1870.
363. Zahn, D., and J. Brickmann, 1999. *Isr. J. Chem.* 39:469–482.
364. Laio, A., J. VandeVondele, and U. Rothlisberger, 2002. *J. Chem. Phys.* 116:6941.
365. König, P. H., N. Ghosh, M. Hoffmann, M. Elstner, E. Tajkhorshid, T. Frauenheim, and Q. Cui, 2006. *J. Phys. Chem. A* 110:548–563.
366. Warshel, A., and R. M. Weiss, 1980. *J. Am. Chem. Soc.* 102:6218–6226.
367. Vuilleumier, R., and D. Borgis, 1997. *J. Mol. Struct.* 436:555–565.
368. Sagnella, D. E., and M. E. Tuckerman, 1998. *J. Chem. Phys.* 108:2073.
369. Schmitt, U. W., and G. A. Voth, 1999. *J. Chem. Phys.* 111:9361–9381.
370. Day, T. J. F., A. V. Soudackov, M. Cuma, U. W. Schmitt, and G. A. Voth, 2002. *J. Chem. Phys.* 117:5839–5849.

371. Wu, Y., H. Chen, F. Wang, F. Paesani, and G. A. Voth, 2008. *J. Phys. Chem. B* 112:467–482.
372. Gu, W., and V. Helms, 2007. *Comput. Phys. Comm.* 8:2445–2451.
373. Mucha, M., T. Frigato, L. M. Levering, H. C. Allen, D. J. Tobias, L. X. Dang, and P. Jungwirth, 2005. *J. Phys. Chem. B* 107:7617–7623.
374. Gu, W., and V. Helms, 2009. *J. Am. Chem. Soc.* 131:2080–2081.
375. Bylaska, E. J., W. A. de Jong, N. Govind, K. Kowalski, T. P. Straatsma, M. Valiev, D. Wang, E. Apra, T. L. Windus, J. Hammond, P. Nichols, S. Hirata, M. T. Hackler, Y. Zhao, P.-D. Fan, R. J. Harrison, M. Dupuis, D. M. A. Smith, J. Nieplocha, V. Tipparaju, M. Krishnan, Q. Wu, T. V. Voorhis, A. A. Auer, M. Nooijen, E. Brown, G. Cisneros, G. I. Fann, H. Fruchtl, J. Garza, K. Hirao, R. Kendall, J. A. Nichols, K. Tsemekhman, K. Wolinski, J. Anchell, D. Bernholdt, P. Borowski, T. Clark, D. Clerc, H. Dachsel, M. Deegan, K. Dyall, D. Elwood, E. Glendening, M. Gutowski, A. Hess, J. Jaffe, B. Johnson, J. Ju, R. Kobayashi, R. Kutteh, Z. Lin, R. Littlefield, X. Long, B. Meng, T. Nakajima, S. Niu, L. Pollack, M. Rosing, G. Sandrone, M. Stave, H. Taylor, G. Thomas, J. van Lenthe, A. Wong, and Z. Zhang, 2007. NWChem, A Computational Chemistry Package for Parallel Computers, Version 5.1. Pacific Northwest National Laboratory, Richland, Washington 99352-0999.
376. van der Spoel, D., E. Lindahl, B. Hess, G. Groenhof, A. E. Mark, and H. J. C. Berendsen, 2005. *J. Comput. Chem.* 26:1701–1718.
377. Mark, P., and L. Nilsson, 2001. *J. Phys. Chem. A* 105:9954–9960.
378. Berendsen, H. J. C., J. R. Grigera, and T. P. Straatsma, 1987. *J. Phys. Chem.* 91:6269–6271.
379. Fornili, S. L., M. Migliore, and M. A. Palazzo, 1986. *Chem. Phys. Lett.* 125:419–424.
380. Robinson, R. A., and R. H. Strokes, 1959. *Electrolyte Solutions*. Butterworths, London.
381. Rapaport, D. C., 1983. *Mol. Phys.* 50:1151.
382. Luzar, A., 2000. *J. Chem. Phys.* 113:10663–10675.
383. Kornyshev, A. A., A. M. Kuznetsov, E. Spohr, and J. Ulstrup, 2003. *J. Phys. Chem. B* 107:3351–3366.
384. Hermida-Ramón, J. M., and G. Karlström, 2004. *J. Mol. Struct.* 712:167–173.
385. Intharathep, P., A. Tongraar, and K. Sagarik, 2006. *J. Comput. Chem.* 27:1723–1732.
386. Botti, A., F. Bruni, S. Imberti, M. A. Ricci, and A. K. Soper, 2005. *J. Mol. Liquids* 117:77–79.
387. Markovitch, O., and N. Agmon, 2007. *J. Phys. Chem. A* 111:2253–2256.
388. White, S. H., 1978. *Biophys. J.* 23:337–347.
389. Roberts, N. K., 1976. *J. Phys. Chem.* 80:1117–1120.
390. Heberle, J., J. Riesle, G. Thiedemann, D. Oesterheit, and N. A. Dencher, 1994. *Nature* 370:379–382.
391. Alexiev, U., R. Mollaaghababa, P. Scherrer, H. G. Khorana, and M. P. Heyn, 1995. *Proc. Natl. Acad. Sci. USA* 92:372–376.
392. Senda, M., J. Takeda, S. Abe, and T. Nakamura, 1979. *Plant Cell Physiol.* 20:1441–1445.
393. Warshel, A., 2003. *Ann. Rev. Biophys. Biomol. Struct.* 32:425–443.
394. Long, S. B., X. Tao, E. B. Campbell, and R. MacKinnon, 2007. *Nature* 450:376–382.
395. Sorensen, T. L.-M., C. Olesen, A.-M. L. Jensen, J. V. Moller, and P. Nissen, 2006. *J. Biotech* 124:704–716.
396. Jahn, R., T. Lang, and T. C. Südhof, 2003. *Cell* 112:519–533.

List of publications

Andreas Springer, [Shirley W.I. Siu](#), Volker Hagen, Dimitry Cherepanov, Yuri N. Antonenko, Bert L. de Groot, Rainer A. Böckmann, Peter Pohl. **Retention of protons at the membrane water interface in the absence of specific binding sites or electrostatic attraction.** (manuscript in preparation).

Ling Wang, [Shirley W.I. Siu](#), Wei Gu, and Volkhard Helms. **Downhill binding energy surface of the barnase-barstar complex.** *Biopolymers* (2010), accepted for publication.

Siti Azma Jusoh, Christoph Welsch, [Shirley W.I. Siu](#), Rainer A. Böckmann, Volkhard Helms. **Contribution of charged and polar residues for the formation of the E1-E2 heterodimer from Hepatitis C Virus.** *J. Mol. Model.* (2010), accepted for publication.

[Shirley W.I. Siu](#) and Rainer A. Böckmann. **Low free energy barrier for ion permeation through double-helical Gramicidin.** *J. Phys. Chem. B* 113 (2009), 3195–3202.

Robert Vácha, [Shirley W.I. Siu](#), Michal Petrov, Rainer A. Böckmann, Justyna Barucha-Kraszewska, Piotr Jurkiewicz, Martin Hof, Max L. Berkowitz, Pavel Jungwirth. **Effects of alkali cations and halide anions on the DOPC lipid membrane.** *J. Phys. Chem. A* 113 (2009), 7235–7243.

Rui Wang, [Shirley W.I. Siu](#), Rainer A. Böckmann. **Fine-grained protein mutation extraction from biological literature.** *Proceedings of ICECT 2009*, 401–405, Macau, China, IEEE Computer Society, 2009.2.

Daniele Narzi, [Shirley W.I. Siu](#), Christian U. Stirnimann, John P.A. Grimshaw, Rudi Glockshuber, Guido Capitani, Rainer A. Böckmann. **Evidence for proton shuffling in a thioredoxin-like protein during catalysis.** *J. Mol. Biol.* 382 (2008), 978–986.

Shirley W. I. Siu, Robert Vácha, Pavel Jungwirth, Rainer A. Böckmann. **Biomolecular simulations of membranes: Physical properties from different force fields.** *J. Chem. Phys.* 128 (2008), 125103. *Selected for April issue of Virtual Journal of Biological Physics Research.*

Shirley W.I. Siu and Rainer A. Böckmann. **Electric Field Effects on Membranes: Gramicidin A as a Test Ground.** *J. Struc. Biol.* 157 (2007), 545–556.